A highly integrated Surface Plasmon Resonance Sensor based on a Focusing Diffractive Optic Element

Muhammad Zeeshan Khalid



Department of Electrical and Computer Engineering McGill University Montreal, Canada

June, 2007

Abstract

Surface plasmon resonance (SPR) sensing is now widely used in biosensing applications. There is significant scope to reduce the cost and complexity of existing commercial devices by increasing the level of optical integration. This thesis presents an SPR sensor that utilizes a diffractive optical element (DOE) which is integrated directly into the sensor-head and which significantly reduces the optical complexity. This design is intended for eventual mass replication via a suitable molding technique. This system is designed to be used within an angular sensing scheme and the DOE delivers the required 15° angular beam divergence. The beam-steering optics are modeled using ray-tracing, while the diffraction efficiency analysis of the DOE is performed using both scalar and rigorous techniques. The complete design, fabrication and experimental results are presented.

Sommaire

La détection par résonance plasmonique de surface est fréquemment employée dans les biocapteurs. Il serait donc avantageux de réduire le coût et la complexité des appareils commerciaux en augmentant leur niveau d'intégration optique. Cette thèse présente un capteur par résonance plasmonique de surface qui utilise un élément d'optique diffractive intégré directement dans la tête du capteur pour simplifier le système optique. Le capteur est conçu pour être éventuellement fabriqué à grande échelle par moulage. Le système est basé sur la détection angulaire et l'élément diffractif permet d'obtenir les 15 degrés de divergence nécessaire. L'optique utilisée pour contrôler le faisceau lumineux est modelée par lancer de rayon alors que l'analyse de l'élément diffractif est accomplie à l'aide de méthodes scalaires et vectorielles. La conception et la fabrication du système sont présentées, ainsi que des résultats de tests expérimentaux.

Acknowledgements

Firstly, I would like to thank my supervisor Dr. Andrew Kirk for his guidance and infinite patience with me. This thesis would not have been possible without his support, ideas and feedback. I would also like to thank the Fonds Québécois de la Recherche sur la Nature et les Technologies (FQRNT) and the Gar Lam Yip Memorial Foundation for funding this research.

I would like to extend my gratitude to my colleagues and friends in the Photonic Systems Group who have made this experience more memorable. In particular, I would like to thank Colin Alleyne, Xuyen Hoa, Cristina Marinescu and Michael Menard for their counsel and help with the fabrication and testing aspects of my work. I would also like to thank Daniel Paetz who helped perform the FDTD diffraction efficiency analysis.

Finally, I would like to thank my family. The undying support of my parents, my brother and my fiancé has carried me forward and kept me sane throughout graduate school.

Table of Contents

Abstract		1
Sommaii	re	1
Acknow	ledgements	2
Chapter	1: Introduction	5
Chapter	2: Surface Plasmon Resonance Modeling	7
2.1	Biosensing with Surface Plasmon Resonance	7
2.2	SPR Model	12
2.3	References	14
Chapter	3: Integrated SPR Sensors – Literature Review	16
3.1	References	19
Chapter -	4: SPR Sensor Layout	
4.1	Diffractive Optical Elements	
4.2	Structural Model	
4.3	Discussion	28
4.4	References	
Chapter	5: DOE Surface-relief Profile Modeling	30
5.1	Cylindrical Diffractive Mirror Model	
5.1.		
5.1.	2 Finite-thickness Design	
5.2	Analytical Modeling Results	
5.3	References	
Chapter	6: Phase and Ray-trace Modeling	
6.1	Background theory	38
6.2	Ray-trace simulation	40
6.2.	1 Phase Modeling	41
6.2.	2 System Performance Metrics	43
6.3	References	46
Chapter	7: Diffraction Efficiency Modeling	48
7.1	Background Theory - Diffraction Efficiency	48
7.2	Scalar Method	
7.2.	1 Scalar diffraction theory	
7.2.	2 Local linear grating model	53
7.3	Rigorous Method	54
7.4	Results and discussion	55
7.5	References	56
Chapter	8: Fabrication	58
8.1	Diffractive mirror fabrication	58
8.1.	1 Mask Design	59
8.1.		
8.2	Coupling slab fabrication	69
8.2.		
8.2.	2 Process-flow	70
83	Fabrication results	73

8.4	References	77
Chapter	9: Testing and Results	
9.1	Test Setup	
9.1	.1 Laser characterization	80
9.1	.2 Beam Profile	81
9.1	.3 Design of output focusing optics	83
9.1	.4 Flow cell	84
9.2	Results and Discussion	85
9.2	Diffraction Efficiency Calculations	88
9.2	2.2 SPR Measurements	89
9.2	Noise measurements and detection limit	101
9.3	Summary of sensor performance	102
9.4	Future considerations	103
9.5	References	104
Conclusion		

Chapter 1: Introduction

The surface plasmon resonance (SPR) technique is primarily used to detect molecular binding events at a metal surface by measuring changes in the local refractive index. SPR biosensing has gained enormous interest and popularity over the past couple decades for its versatility, sensitivity and low cost potential. Commercial SPR sensors are used in numerous disciplines such as health care, pharmaceutical research, environmental protection and forensic science, owing to the ability to provide label-free and real-time detection of biological and chemical interactions. Moreover, SPR sensors can be customized to detect any analyte in an aqueous solution, as long as a corresponding biorecognition element is available, which makes them extremely adaptable.

The primary motivation for this research is a vision to develop highly accurate SPR biosensors which are cheap, disposable and mass producible. The work presented in this thesis is the first step towards achieving this vision. The aim is to develop a working prototype of a highly integrated SPR sensor which is easy and cheap to fabricate, compact, precise and accurate. For many applications in various fields such as medicine and pharmaceutical research, simultaneous detection of multiple biomarkers is essential, and as such, the proposed SPR sensor must possess this ability. The sensor must be highly sensitive, have low system noise and should have the ability to detect small changes in analyte concentrations. The device design presented in Chapter 4 is based on all the above listed factors.

The thesis is broken down in the following manner: Chapter 2 provides an introduction to the SPR sensing concept, whereas a review of the available literature on various existing SPR sensors is presented in Chapter 3. Chapter 4 deals with the design of our SPR sensor which is based primarily on the use of a diffractive optical element (DOE). Analytical and ray-trace modeling results of the DOE are discussed in Chapter 5 and 6, respectively, whereas Chapter 7 deals with scalar and rigorous diffraction efficiency analysis of the

DOE. The fabrication process-flow and results are presented in Chapter 8. Lastly, Chapter 9 deals with the final testing and performance results of the SPR sensor.

Chapter 2: Surface Plasmon Resonance Modeling

This chapter provides an introduction to the phenomenon of surface plasmon resonance and an analytical SPR model is presented. Simulation results for the SPR configuration that is employed, are also provided.

2.1 Biosensing with Surface Plasmon Resonance

A surface plasmon wave or a surface plasmon-polariton (SPP) is a charge density wave occurring at the interface between a metal and a dielectric when photons of TM polarized light incident on the metal are resonant with the collective oscillations of unbound electrons in the metal [2.1]. It is a phenomenon by which light energy is transferred resonantly to a surface plasmon mode coupled to collective oscillations of electrons in a metal [2.2]. The SPP is a transverse-magnetic (TM) wave that propagates along the metal-dielectric boundary and, like any electromagnetic wave, is characterized by a complex propagation constant given by:

$$k_{SP} = \frac{2\pi}{\lambda} \sqrt{\frac{\varepsilon_M \varepsilon_D}{\varepsilon_M + \varepsilon_D}}$$
 Eq. 2.1

where λ is the wavelength of light, and ϵ_M and ϵ_D are the complex dielectric functions of the metal and dielectric, respectively. This equation describes an SPP if the real part of ϵ_M is negative and its absolute value is smaller than ϵ_D [2.3]. This condition is readily satisfied by several metals at optical wavelengths.

Surface plasmon resonance is a phenomenon that occurs when the energy and momentum of an incoming photon on a metal-dielectric boundary is completely transferred to an SPP. The momentum of a photon in air which is incident on a metal-dielectric boundary is given by:

$$k_{PH} = \frac{2\pi}{\lambda} n_0 \sin \theta_i$$
 Eq. 2.2

where $n_0 = 1$. For any angle θ_i , the momentum cannot match that of the SPP given by Eq. 2.1, hence, a photon in air can never excite an SPP. Various coupling schemes have been proposed to increase the momentum of the exciting photon. The attenuated total internal reflection (ATR) prism configuration, also known as the Kretchmann-Raether setup (Fig. 2.1) is the most widespread [2.4]. In this scheme, the photon is incident on the metal-dielectric boundary via a high refractive index prism, thus having its momentum increased by a factor of n_P – the refractive index of the prism.

Due to an increase in the photon momentum, resonant coupling then becomes possible at a well defined angle θ_{res} :

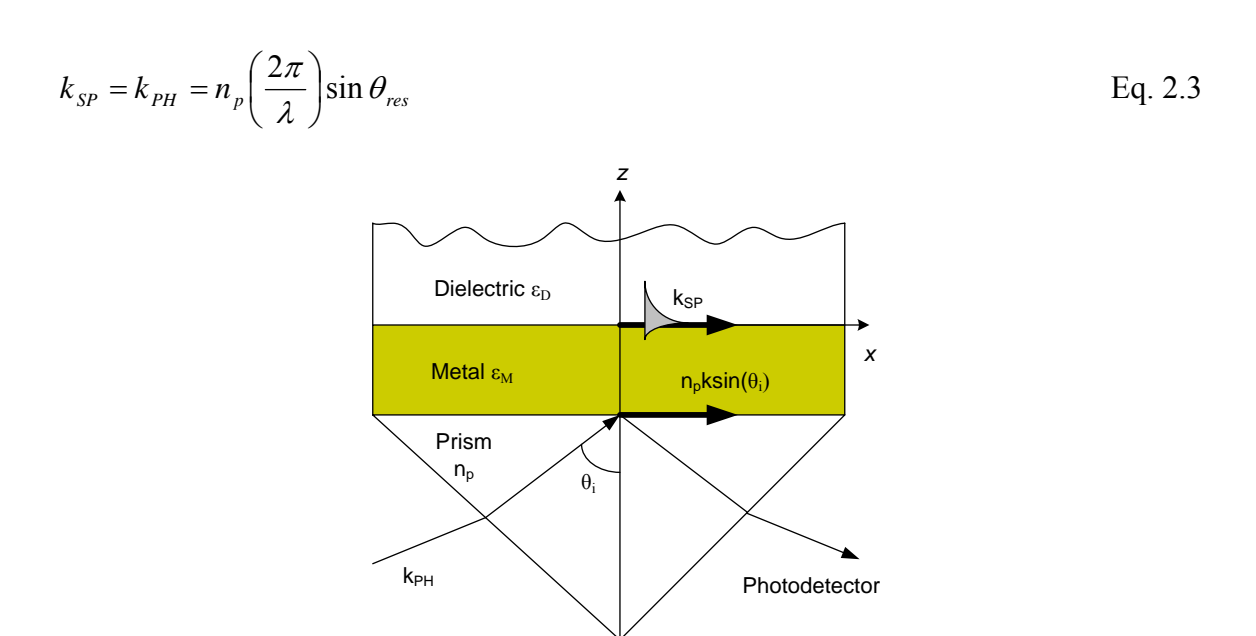


Fig. 2.1: Schematic of a 3-layer ATR system

The electromagnetic field of an SPP is confined at the metal-dielectric boundary and decreases exponentially into both media. Penetration depth is a parameter which measures the distance from the interface at which the amplitude of the SPP evanescent field falls by 1/e of its value at the metal interface. The penetration depth can be several

hundred nanometers, particularly into the dielectric, at visible and near infrared wavelengths [2.5]. It is the interaction of the evanescent field with the dielectric and the resulting sensitivity of the SPP wave-vector to the refractive index of the dielectric that forms the basis for SPR sensing.

For biosensing purposes, the metal film is generally a thin (~50nm) gold film. Silver displays stronger surface plasmon coupling, however gold is preferred due to its chemical stability. The dielectric is usually a liquid sample containing a certain analyte. Biorecognition elements are immobilized on the surface of the metal which recognize and capture analyte present in the solution producing a change in the refractive index at the metal surface. This gives rise to a change in the propagation constant of the SPP propagating along the metal surface which can be accurately measured by optical means. This process is summarized in Fig 2.2.

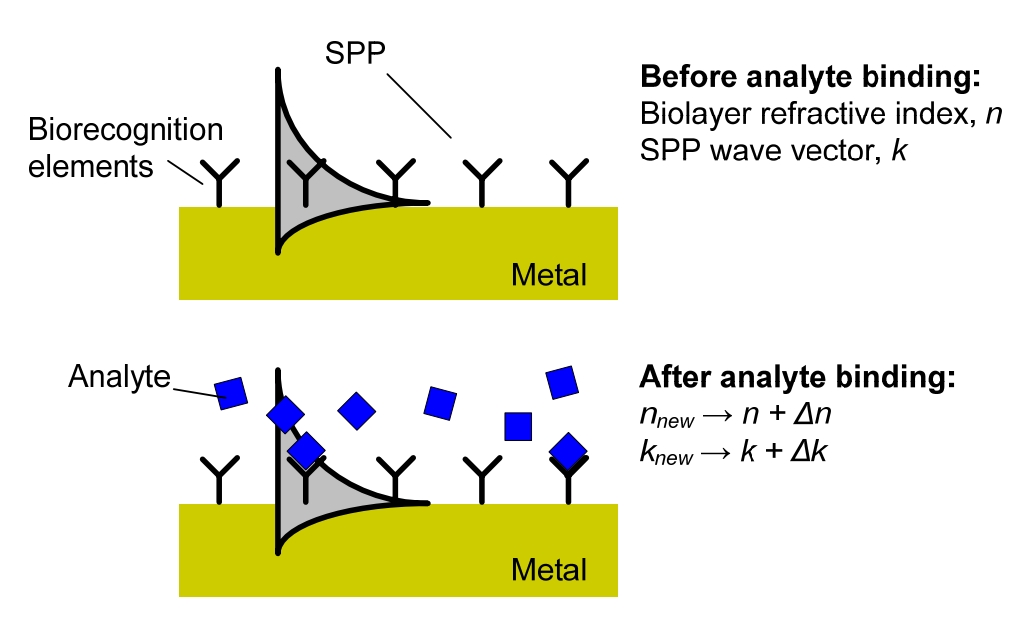


Fig. 2.2: Principle of SPR biosensing

The interaction of a light wave with an SPP can change some of the wave characteristics such as amplitude, phase and polarization [2.3]. Biosensors can then be classified according to the type of change that is measured. For instance, in an angular interrogation ATR experiment [2.6-8], the incidence angle is scanned and the intensity of the reflected

beam is measured by a photo-detector array. At the resonant coupling angle, the light is completely transferred to surface plasmons, hence, a sharp dip in the reflected intensity would be noted at the output. A local change in the refractive index near the metal surface due to analyte binding would result in a shift of the position of the reflectivity dip. This change can then be correlated with a corresponding change in the propagation constant of the SPP and the concentration of the analyte. Similarly, wavelength interrogation [2.9-11] schemes are also widespread, where polychromatic light is used to excite SPPs at a fixed angle of incidence. Resonant coupling occurs at a specific wavelength, resulting in a sharp decrease in the measured reflectivity. Again, binding events close to the metal surface cause a local change in the refractive index resulting in a shift in the resonant coupling wavelength. The shift can be easily measured using a spectrometer and can be used to determine the analyte concentration. Some other established measurement approaches include phase and polarization detection [2.12-14].

Reflectivity for TM polarized light as a function of angle of incidence for a 3-layer setup can be determined by the following [2.15]:

$$R(\theta) = \left| \frac{r_{SM} + r_{MD} \exp(-2\gamma_M d_M)}{1 + r_{SM} r_{MD} \exp(-2\gamma_M d_M)} \right|^2$$

$$r_{PM} = \frac{\varepsilon_M \gamma_S - n_S^2 \gamma_M}{\varepsilon_M \gamma_S + n_S^2 \gamma_M}$$

$$r_{MD} = \frac{\varepsilon_D \gamma_M - \varepsilon_M \gamma_D}{\varepsilon_D \gamma_M + \varepsilon_M \gamma_D}$$

$$\epsilon_D \gamma_M + \varepsilon_M \gamma_D$$

$$\gamma_M = \sqrt{-\varepsilon_M \left(\frac{2\pi}{\lambda}\right)^2 + k^2}, \gamma_S = \sqrt{n_S^2 \left(\frac{2\pi}{\lambda}\right)^2 - k^2}, \gamma_D = \sqrt{k^2 - \varepsilon_D \left(\frac{2\pi}{\lambda}\right)^2}$$

$$k = \frac{2\pi}{\lambda} n_P \sin \theta$$

where r_{PM} and r_{MD} are the fresnel reflection coefficients for the prism-metal interface and metal-dielectric interface, respectively, and d_M is the thickness of the metal layer. Fig. 2.3 shows a typical Reflectivity vs. Angle of Incidence curve for an angular interrogation based biosensor.

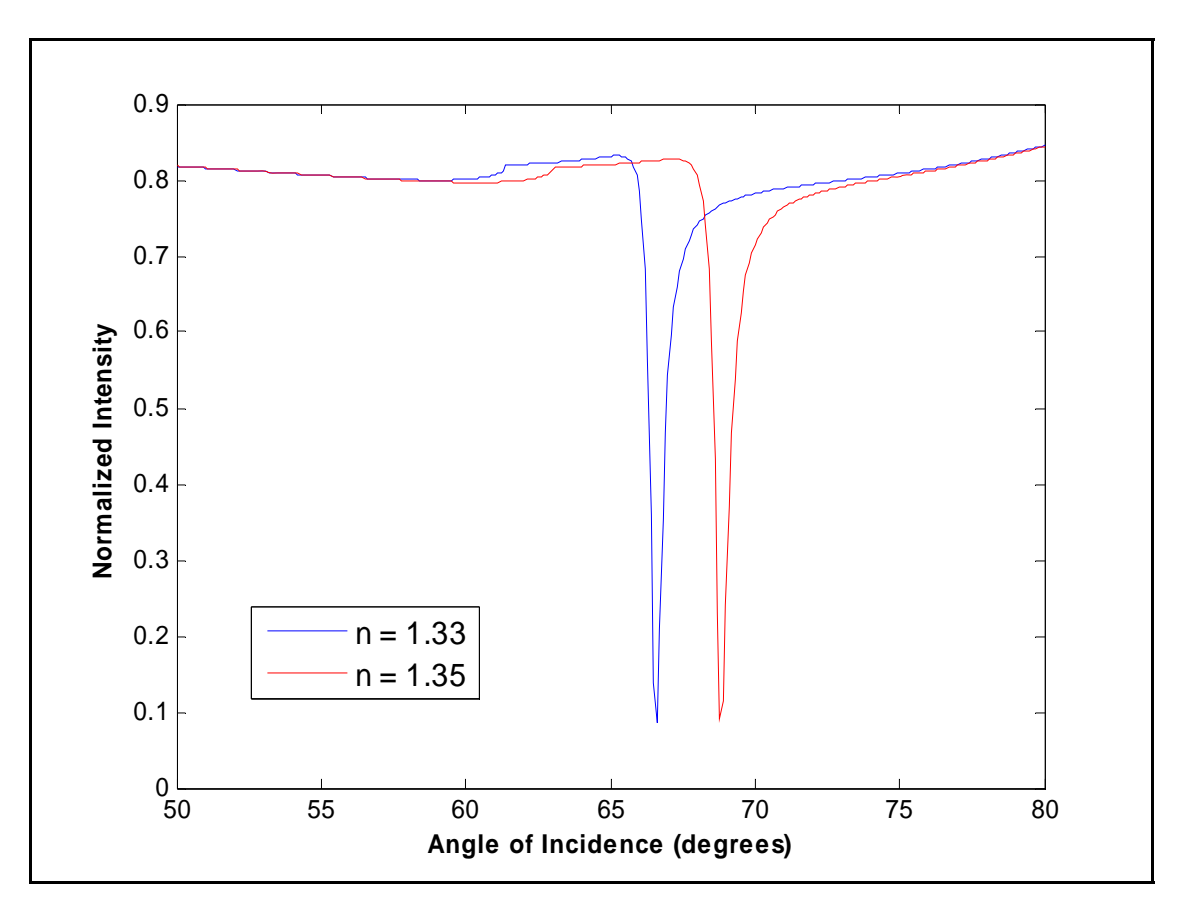


Fig. 2.3: Reflectivity for light wave exciting an SPP in the ATR configuration (NBK7 glass prism – 50nm thick gold film – dielectric) versus the angle of incidence for two different refractive indices of the dielectric (wavelength 632.8nm)

The characteristics that determine the performance of an SPR system include sensitivity, accuracy, specificity and lowest detection limit. Depending on whichever interrogation method is used (e.g. angular, wavelength, phase), it is desirable to obtain a large change in the SPR output as the refractive index near the metal surface changes. Thus, sensitivity is a key benchmark which depends on a number of factors such as the interrogation method employed, chemical properties of the biorecognition elements and analytes, the sensitivity of the SPP propagation constant to the change in refractive index and the efficiency with which analyte with a specific concentration contributes to change in refractive index. Specificity is an equally important characteristic that is marked by the ability of the biorecognition elements to capture the targeted analyte. The presence or

detection of non-targeted molecules in high concentration can lead to distorted results. Lastly, the detection limit is a parameter that determines the lowest possible change in the refractive index and hence, the analyte concentration, that can be detected by the biosensor. The detection limit can be lowered by increasing sensitivity and decreasing system noise contributed by the optics and electronics comprising the biosensor.

2.2 SPR Model

The Kretchmann-Raether setup shown in Fig. 2.1 is employed for our design as well; however, the prism is replaced by a flat substrate. Atop the substrate is a gold layer 50nm thick. The gold layer is then covered with a layer of biorecognition elements (2–3nm thick) which has a negligible effect on the 3-layer SPR model developed in the previous section. The sensor is then placed in a certain analyte solution as shown in Fig. 2.4.

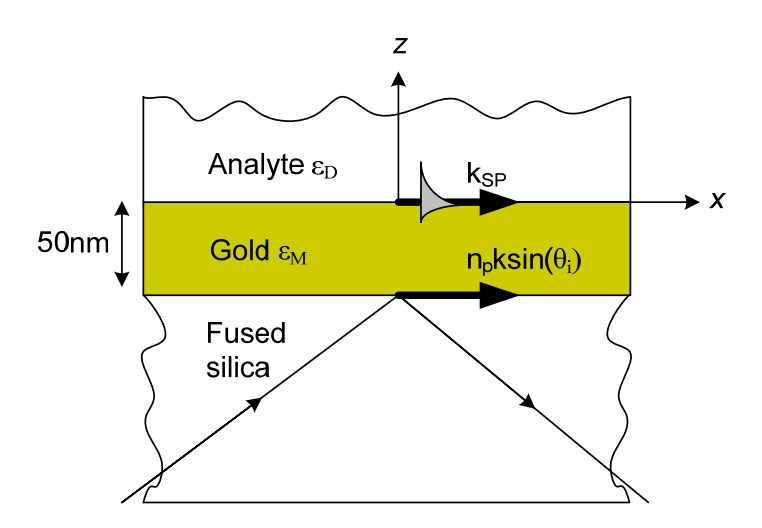


Fig. 2.4: 3-Layer ATR configuration employed for SPR modeling

Equations 2.1–3 can then be used to calculate the resonance angle. Visible and near infrared wavelengths are commonly used for SPR sensors and we decided to choose 850nm light purely because of its availability in our labs. Fused silica was chosen as the substrate material because it is cheap, readily available, has excellent optical properties and has been thoroughly researched and documented for micro-optics applications at

McGill. For 850nm wavelength light the refractive index of fused silica and gold are n_{fs} = n_p = 1.4525 and n_{gold} = n_M = 0.195 + j5.55 [2.16], respectively. The required dielectric constants for Eq. 2.1 are simply related to the refractive indices by $\varepsilon_x = n_x^2$. Assuming the refractive index of the analyte solution is n_D =1.33, the resonant angle θ_{res} is found to be 70.5°. This was verified using an SPR simulator – Winspall [2.17]. Fig. 2.5 shows the reflectivity as a function of angle of incidence and a sharp dip can be seen centered at 70.5°.

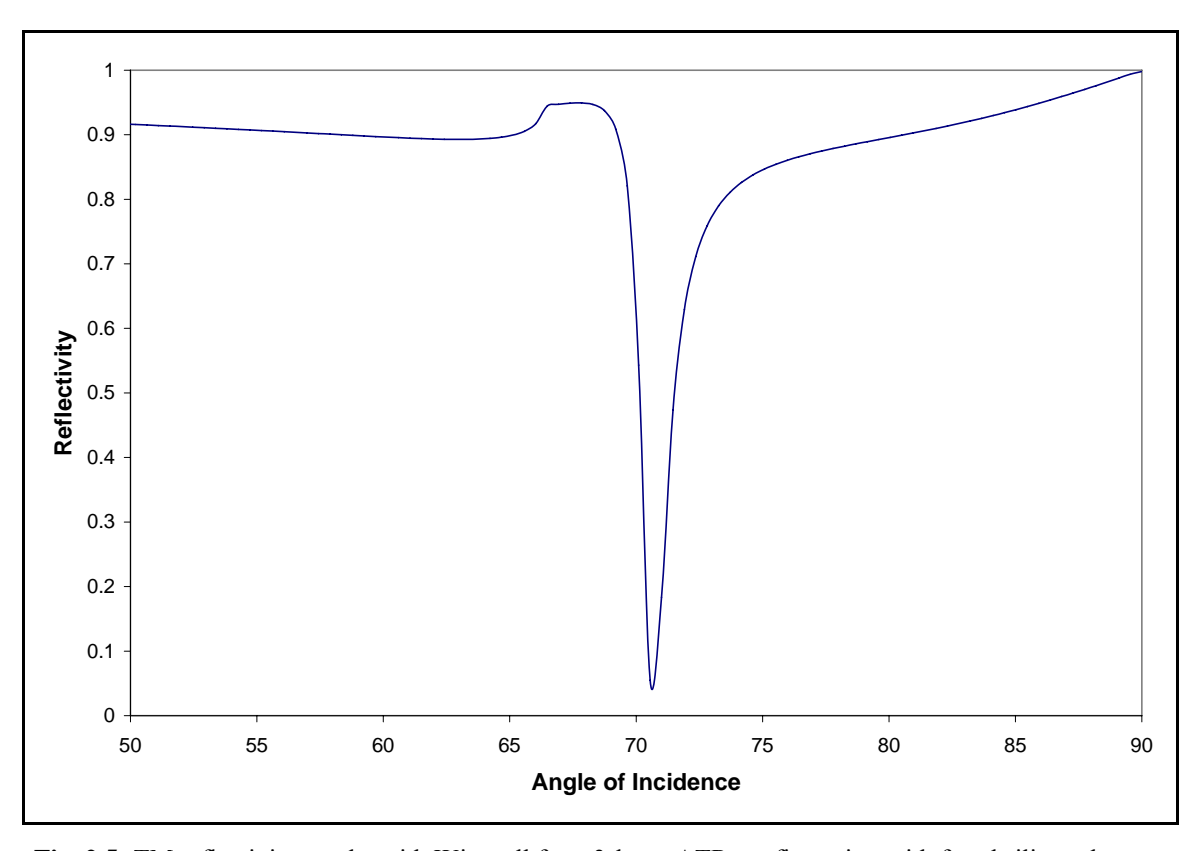


Fig. 2.5: TM reflectivity results with Winspall for a 3-layer ATR configuration with fused silica substrate $(n_{fs}=14525)$, 50nm gold layer $(n_{gold}=0.195+5.55i)$, and analyte $(n_D=1.33)$ at 850nm wavelength.

Throughout the literature, there are large variations in the refractive index of gold as reported by various researchers using various measurement techniques. Therefore, the value used is only an approximation and is a source of error for both the analytical and Winspall results. Hence, in practice, the position of the dip could be shifted to a slightly

lower or higher angle, and the dip could be shallower and wider than that depicted in Fig. 2.5.

Lastly, for a refractive index change of Δn , the angular sensitivity can be expressed using Eqs. 2.1–3 as [2.18]:

$$S = \frac{\partial \theta_{res}}{\partial n_{new}} = S = \frac{\varepsilon_M^2}{|\varepsilon_M + n_{new}^2| \sqrt{\varepsilon_M n_{fs}^2 (\varepsilon_M + n_{new}^2) - \varepsilon_M^2 n_{new}^2}}$$
 (rad/RIU), Eq. 2.5

where $n_{new} = n_D + \Delta n$ can be calculated using the new shifted θ_{res} and RIU stands for refractive index units which can be chosen arbitrarily.

2.3 References

- [2.1] B. Liedberg, C. Nylander, and I. Lundstrom, "Biosensing with Surface-Plasmon Resonance How It All Started," *Biosensors & Bioelectronics*, vol. 10, no. 8, p. R1-R9, 1995.
- [2.2] H. Raether, Surface Plasmons on smooth and Rough Surfaces and on Gratings. Berlin: Springer-Verlag, 1988.
- [2.3] J. Homola, "Present and future of surface plasmon resonance biosensors," *Analytical and Bioanalytical Chemistry*, vol. 377, no. 3, pp. 528-539, Oct.2003.
- [2.4] W. Knoll, "Integrated-Optics for the Characterization of Photoreactive Organic Thin-Films," *Pure and Applied Chemistry*, vol. 67, no. 1, pp. 87-94, Jan.1995.
- [2.5] J. Homola, S. S. Yee, and G. Gauglitz, "Surface plasmon resonance sensors: review," *Sensors and Actuators B: Chemical*, vol. 54, no. 1-2, pp. 3-15, Jan.1999.
- [2.6] B. P. Nelson, A. G. Frutos, J. M. Brockman, and R. M. Corn, "Near-Infrared Surface Plasmon Resonance Measurements of Ultrathin Films. 1. Angle Shift and SPR Imaging Experiments," *Anal. Chem.*, vol. 71, no. 18, pp. 3928-3934, Sept.1999.
- [2.7] K. H. Chen, J. H. Chen, and J. Y. Lin, "Comparison of Kretschmann-Raether configuration angular and thickness regimes with phase-difference shift for measuring changes in refractive index," *Optical Engineering*, vol. 45, no. 2 Feb.2006.

- [2.8] S. Patskovsky, A. V. Kabashin, and M. Meunier, "Near-infrared surface plasmon resonance sensing on a Si platform with nanoparticle-based signal enhancement," *Optical Materials*, vol. 27, no. 5, pp. 1093-1096, 2005.
- [2.9] K. Johansen, H. Arwin, I. Lundstrom, and B. Liedberg, "Imaging surface plasmon resonance sensor based on multiple wavelengths: Sensitivity considerations," *Review of Scientific Instruments*, vol. 71, no. 9, pp. 3530-3538, Sept.2000.
- [2.10] X. Liu, D. Q. Song, Q. L. Zhang, Y. Tian, L. Ding, and H. Q. Zhang, "Wavelength-modulation surface plasmon resonance sensor," *Trac-Trends in Analytical Chemistry*, vol. 24, no. 10, pp. 887-893, Nov.2005.
- [2.11] A. Hanning, J. Roeraade, J. J. Delrow, and R. C. Jorgenson, "Enhanced sensitivity of wavelength modulated surface plasmon resonance devices using dispersion from a dye solution," *Sensors and Actuators B: Chemical*, vol. 54, no. 1-2, pp. 25-36, Jan.1999.
- [2.12] Z. L. Sun, Y. H. He, and J. H. Guo, "Surface plasmon resonance sensor based on polarization interferometry and angle modulation," *Applied Optics*, vol. 45, no. 13, pp. 3071-3076, May2006.
- [2.13] J. F. Liu, D. Xiang, X. L. Yu, and D. S. Wang, "Data analysis of surface plasmon resonance biosensor based on phase detection," *Sensors and Actuators B-Chemical*, vol. 108, no. 1-2, pp. 778-783, July2005.
- [2.14] H. P. Ho, W. C. Law, S. Y. Wu, X. H. Liu, S. P. Wong, C. Lin, and S. K. Kong, "Phase-sensitive surface plasmon resonance biosensor using the photoelastic modulation technique," *Sensors & Actuators: B. Chemical*, vol. 114, no. 1, pp. 80-84, 2006.
- [2.15] K. Kurihara and K. Suzuki, "Theoretical Understanding of an Absorption-Based Surface Plasmon Resonance Sensor Based on Kretchmann's Theory," *Anal. Chem.*, vol. 74, no. 3, pp. 696-701, Feb.2002.
- [2.16] E. D. Palik, "Handbook of Optical-Constants," *Journal of the Optical Society of America A-Optics Image Science and Vision*, vol. 1, no. 12, p. 1297, 1984.
- [2.17] W. Knoll, Winspall 3.01, www.mpipmainz.mpg.de/knoll/soft/index.html
- [2.18] C. Thirstrup, W. Zong, M. Borre, H. Neff, H. C. Pedersen, and G. Holzhueter, "Diffractive optical coupling element for surface plasmon resonance sensors," *Sensors and Actuators B: Chemical*, vol. 100, no. 3, pp. 299-309, May2004.

Chapter 3: Integrated SPR Sensors – Literature Review

The "Smaller is Better" philosophy has always been fiercely pursued in the optics and electronics industry. Increasing the amount of monolithic integration can improve the overall performance of a system by making it more durable, compact, efficient, precise and more often than not, accurate. The simple prism-coupling ATR configuration presented in Chapter 2 has many mechanical interfaces, such as coupling optics, detector arrays, removable prism and a microfluidic chamber to deliver analyte to the sensing element. Such an instrument requires tremendous maintenance, and suffers from poor repeatability and precious, thereby, limiting its use to primarily a research tool. Thus, integrating the various components comprising the SPR sensor together can broaden the applications of the instrument.

Commercial SPR sensors with fully integrated opto-electronics and microfluidics have been around for some time. Most of these instruments rely on prism-coupling schemes of various designs. The first commercial SPR biosensor was released by Biacore International which was based on the Kretschmann configuration in 1990 [3.1]. Since then tremendous amount of work has been geared towards developing more compact, accurate and sensitive biosensors. Spreeta by Sensata [3.2] is another, popular, fully integrated commercial sensor which is based on angular interrogation using the ATR configuration. It employs a sensing medium placed on an angled prism facet. A diverging beam of light from a narrow-band LED is used to generate SPPs and thus, a whole angular spectrum is obtained at the output. Other commercially available SPR biosensors have been developed by Analytical μ -Systems (Bio-suplar 2) and British Windsor Scientific (IBIS) [3.3].

Thirstrup et al. [3.4] have presented a novel design of a highly integrated planar sensor, based on the Spreeta concept of angular reflectivity spectrum output, that employs diffractive optical elements to couple light in and out of a planar substrate and achieve the required angular spectrum. The sensor is fabricated in polymer using injection

molding and imprinting techniques, which is very attractive, but the detection limit suffers owing to low diffraction efficiency of the diffractive coupling elements.

A similar 'lightpipe' configuration has been employed by Nenninger et al. [3.5] but with dual channels and wavelength modulation. One channel is used to monitor binding events whereas the other channel has no biorecognition elements immobilized on the surface and serves as a reference channel. The difference of the two signals can help compensate for background refractive index and temperature variations. Another novel on-chip referencing scheme has been developed by depositing a high refractive index over layer of tantalum pentoxide over half the sensing surface [3.6]. SPR occurs at different wavelengths for regions with and without the overlayer when illuminated with polychromatic light. The reflectivity spectrum exhibits two dips where one can be used for sensing where as the other as a reference signal. Various other referencing schemes have been studied and it has been reported that residual error after compensation is typically 1–3% of the total RI change, due to background RI variations, whereas temperature compensation is less accurate with the error being 5-10% of the total response due to temperature variation [3.3].

In an effort for further miniaturization, SPR sensors have also been developed on optical fiber platforms. The first fiber-optic SPR sensor, proposed by Jorgenson et al. [3.7], was based on wavelength modulation in a multimode optical fiber. The sensing surface was created by partly stripping the polymer cladding and uniformly depositing gold around the core. The fiber can only support short wavelengths due to numerical aperture constraints, leading to a smaller SP probe depth. Multimode fibers intrinsically exhibit low resolution because they suffer from modal noise. Designs with single mode fibers requiring tapering or side-polishing have also been suggested [3.8–10]; however, they suffer from polarization instability and low sensitivity.

More recently, the focus has been shifted towards multi-analyte sensing or SPR Imaging. In the medicine and pharmaceutical arena, there is a great need for simultaneous detection of multiple biomarkers, thus giving rise to multi-channel SPR sensing systems.

Presently, most commercial SPR sensors offer a small number of independent sensing channels (<20) [3.11]. In the field of proteomics, however, hundreds of channels are required to study protein-peptide interactions, DNA interactions and hybridization, and cellular ligation. The current proteomic methods such as fluorescence or enzyme-linked immunosorbent assay (ELISA) require labels and can not provide real-time results. Thus SPR techniques can have a huge impact by providing label free detection along with kinetic and end-point data. The simplest approach to multi-channel sensing is to divide the metal surface into multiple sensing spots. A multi-channel flow cell is required to immobilize multiple biorecognition elements on the various sensing spots. Prism or grating coupling can then be used together with an interrogation method of choice to perform simultaneous real-time analysis on all channels. Berger et al. [3.12] demonstrated an SPR imaging system with 16 channels in a 4x4 array of sensing spots in a Kretchmann configuration. Such systems require uniform illumination of large sensing areas which can be quite challenging, as such, suffer from lower resolution (~10⁻⁵ RIU) [3.13]. However, Piliarik et al. [3.14] have rectified this issue with a combination of SPR imaging with polarization contrast and a spatially patterned multilayer SPR structure. The sensor has 108 channels and an improved resolution of 3x10⁻⁶ RIU. Another approach is, the Lumera ProteomicProcessor [3.11] that uses a scalable light source engine to project uniform laser power to a protein array with more than 10,000 spots in a 1.4cm² area microarray, making it an extremely high-throughput SPR imaging system.

In contrast to SPR imaging systems, multi-channel systems have also been devised using parallel channels based on spectroscopy of surface plasmons. For instance, the Biacore AB sensor utilizes four parallel converging beams to illuminate parallel sensing surfaces in an ATR configuration with angular modulation. Similarly, the design presented by Thirstrup et al. [3.4] is capable of a throughput of 48 channels. These designs can utilize information contained in the whole angular spectrum and as such have higher resolutions $\sim 3 \times 10^{-7}$ RIU.

Apart from miniaturizing SPR instruments and adding multi-channel capabilities, a lot of research has been focused solely on enhancing SPR sensitivity. The ability of the surface

plasmons to detect biomolecular interactions depends on the strong electromagnetic field enhancement when resonant coupling conditions are met. A similar enhancement is experienced near the surface of gold/silver nanoparticles when the frequency of incoming photons is resonant with the collective oscillations of free electrons within the nanoparticles, giving rise to localized surface plasmons (LSP). LSPs are also observed in gold/silver nanowire gratings [3.15]. The presence of nanoparticles or nanogratings increases the roughness of the sensing surface leading to increased light scattering and energy adsorption. As a result, large changes can be seen in the reflectivity spectra for small refractive index variations near the sensing surface. Hu et al. have presented a novel device with gold nanoparticles embedded in silica, integrated with a standard Kretchmann gold-on-prism geometry [3.16]. A detection performance of ~0.1pg/mm² surface coverage of biomolecules was obtained which is a 10-fold improvement in resolution over conventional SPR sensors with flat sensing interfaces.

As outlined in the previous chapter, the sensitivity of a system as a whole depends on a number of factors but in the context of this chapter, sensitivity improvements resulting only from design and structural configurations are discussed.

3.1 References

- [3.1] S. Lofas, M. Malmqvist, I. Ronnberg, E. Stenberg, B. Liedberg, and I. Lundstrom, "Bioanalysis with Surface-Plasmon Resonance," *Sensors and Actuators B-Chemical*, vol. 5, no. 1-4, pp. 79-84, Aug.1991.
- [3.2] J. Melendez, R. Carr, D. U. Bartholomew, K. Kukanskis, J. Elkind, S. Yee, C. Furlong, and R. Woodbury, "A commercial solution for surface plasmon sensing," *Sensors and Actuators B-Chemical*, vol. 35, no. 1-3, pp. 212-216, Sept.1996.
- [3.3] J. Homola, "Present and future of surface plasmon resonance biosensors," *Analytical and Bioanalytical Chemistry*, vol. 377, no. 3, pp. 528-539, Oct.2003.
- [3.4] C. Thirstrup, W. Zong, M. Borre, H. Neff, H. C. Pedersen, and G. Holzhueter, "Diffractive optical coupling element for surface plasmon resonance sensors," *Sensors and Actuators B: Chemical*, vol. 100, no. 3, pp. 299-309, May2004.
- [3.5] G. G. Nenninger, J. B. Clendenning, C. E. Furlong, and S. S. Yee, "Reference-compensated biosensing using a dual-channel surface plasmon resonance sensor system based on a planar lightpipe configuration," *Sensors and Actuators B-Chemical*, vol. 51, no. 1-3, pp. 38-45, Aug.1998.

- [3.6] J. Homola, H. B. Lu, and S. S. Yee, "Dual-channel surface plasmon resonance sensor with spectral discrimination of sensing channels using dielectric overlayer," *Electronics Letters*, vol. 35, no. 13, pp. 1105-1106, 1999.
- [3.7] R. C. Jorgenson and S. S. Yee, "A fiber-optic chemical sensor based on surface plasmon resonance," *Sensors and Actuators B: Chemical*, vol. 12, no. 3, pp. 213-220, Apr.1993.
- [3.8] M. Piliarik, J. Homola, Z. Mankova, and J. Ctyroky, "Surface plasmon resonance sensor based on a single-mode polarization-maintaining optical fiber," *Sensors and Actuators B: Chemical*, vol. 90, no. 1, pp. 236-242, 2003.
- [3.9] K. Kurihara, H. Ohkawa, Y. Iwasaki, O. Niwa, T. Tobita, and K. Suzuki, "Fiberoptic conical microsensors for surface plasmon resonance using chemically etched single-mode fiber," *Analytica Chimica Acta*, vol. 523, no. 2, pp. 165-170, 2004.
- [3.10] R. Slavik, J. Homola, J. Ctyroky, and E. Brynda, "Novel spectral fiber optic sensor based on surface plasmon resonance," *Sensors and Actuators B-Chemical*, vol. 74, no. 1-3, pp. 106-111, Apr.2001.
- [3.11] B. Christina, K. Gibum, C. Shuxin, G. Hannwen, and L. Timothy, "Looking towards label-free biomolecular interaction analysis in a high-throughput format: a review of new surface plasmon...,", 17 ed 2006, pp. 400-405.
- [3.12] C. E. H. Berger, T. A. M. Beumer, R. P. H. Kooyman, and J. Greve, "Surface Plasmon Resonance Multisensing," *Anal. Chem.*, vol. 70, no. 4, pp. 703-706, Feb.1998.
- [3.13] J. Homola, H. Vaisocherova, J. Dostalek, and M. Piliarik, "Multi-analyte surface plasmon resonance biosensing," *Methods*, vol. 37, no. 1, pp. 26-36, Sept.2005.
- [3.14] M. Piliarik, H. Vaisocherova, and J. Homola, "A new surface plasmon resonance sensor for high-throughput screening applications," *Biosensors & Bioelectronics*, vol. 20, no. 10, pp. 2104-2110, Apr.2005.
- [3.15] A. J. Haes and R. P. Van Duyne, "A unified view of propagating and localized surface plasmon resonance biosensors," *Analytical and Bioanalytical Chemistry*, vol. 379, no. 7 8, pp. 920-930, Aug.2004.
- [3.16] W. P. Hu, S. J. Chen, K. T. Huang, J. H. Hsu, W. Y. Chen, G. L. Chang, and K. A. Lai, "A novel ultrahigh-resolution surface plasmon resonance biosensor with an Au nanocluster-embedded dielectric film," *Biosens. Bioelectron.*, vol. 19, no. 11, pp. 1465-1471, June2004.

Chapter 4: SPR Sensor Layout

This chapter focuses primarily on the design layout of the sensor. The dimensions are provided and particular emphasis is laid on explaining design choices. The pros and cons of the chosen configuration are also discussed.

4.1 Diffractive Optical Elements

Over the years, diffractive optical elements (DOEs) have emerged as viable solutions to a number of optical design problems that were considered impossible with traditional refractive and reflective optical elements. DOEs are constructed with a periodic mirco-structure and it is the periodicity and spatial structure that determine the optical performance of the DOEs [4.1].

Two unique properties of diffractive structures have been mostly exploited: first is that diffractive elements exhibit very strong chromatic dispersion which is opposite to the dispersion displayed by refractive elements. In other words, diffractive elements bend light rays of longer wavelengths more than those of shorter wavelengths. This property can be used to correct aberrations caused by a refractive lens in a hybrid system. However, this property also limits the use of diffractive elements with polychromatic light, unless we want to separate the wavelengths for specific applications, e.g. wavelength demultiplexing. The second unique property and the real reason for the popularity of DOEs is the relative ease with which arbitrary phase profiles can be implemented, especially with semi-conductor fabrication techniques [4.2]. This approach produces a multi-level approximation to the ideal profile and as the number of levels increase, the multi-level structure approaches the continuous diffractive profile. Fig. 4.1 illustrates the conversion of a refractive element to a corresponding multi-level diffractive element.

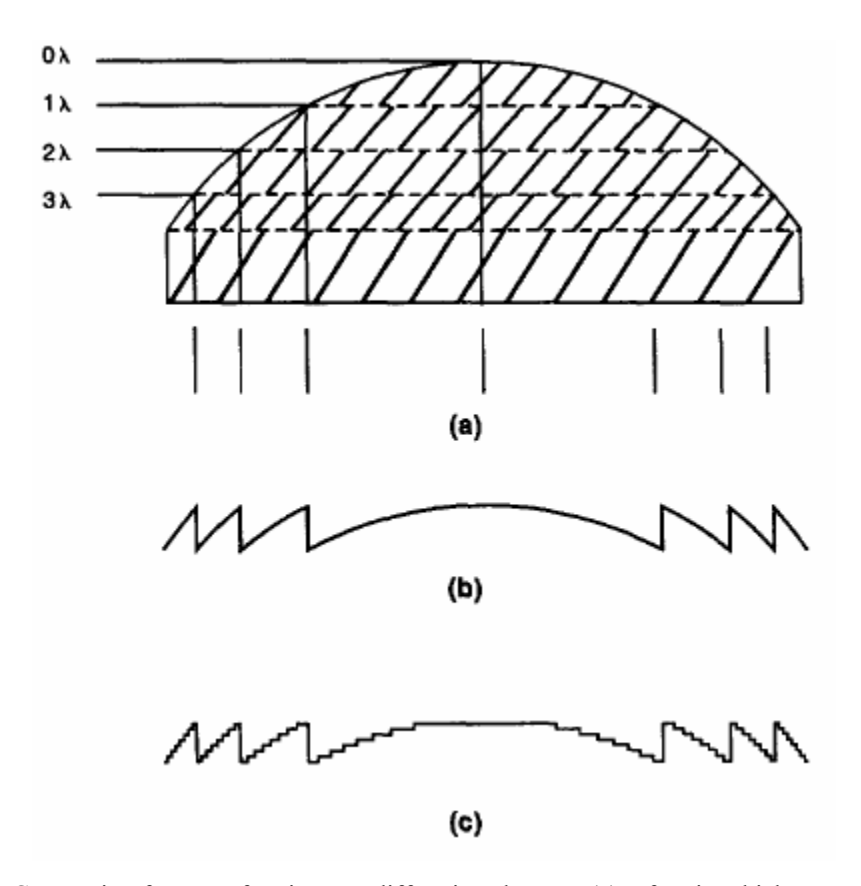


Fig. 4.1: Conversion from a refractive to a diffractive element: (a) refractive thickness profile, (b) continuous diffractive profile, (c) multi-level approximation to the continuous diffractive profile, after [4.3]

A diffractive lens is split up into zones, where each zone is shaped to direct the light such that it adds constructively at the focus. The zones are formed by modulating the lens thickness such that a plane wave incident upon it is never allowed to undergo a phase change of more than 2π . At the point where the phase change reaches 2π (one wavelength), the thickness is brought back down to zero as illustrated in Fig 4.1 (b,c). This has the effect of eliminating redundant glass while maintaining the same phase profile as that of an equivalent refractive element.

Diffractive lenses can have multiple focus points arising from multiple diffraction orders; hence, the aim is to design a lens such that most of the light is directed in a specific diffraction order so as to reduce stray light. The performance of any DOE can be classified on the basis of diffraction efficiency (DE), which quantifies how efficiently a DOE can direct light in a desired direction. An ideally blazed profile (Fig. 4.1(b)) can

have diffraction efficiency close to 100%. For a discretized DOE, however, DE depends on how closely the ideal continuous profile can be approximated with a staircase estimation. The DE increases as the number of levels in the multi-level approximation increase; however, there is a trade-off between the achievable diffraction efficiency and the minimum feature size.

4.2 Structural Model

We intend to design a system with an angular scanning scheme similar to the Spreeta sensor [4.4] that can provide the reflectivity data for a large angular range centered about the resonance angle and should be capable of detecting small changes in the refractive index of the sensing medium. It would be cumbersome and more error-prone to manually scan the laser through each angle to obtain the reflectivity data. Thus, a system that can accurately provide reflectivity data for an entire angular spectrum would be very desirable. An angular range of around 15° centered about the resonance angle (~70°) was chosen, i.e. an angular beam divergence between 63° and 78°, which would give the sensor a large dynamic operating range in terms of refractive index of analyte solutions that can analyzed.

The initial design that was proposed is shown in Fig. 4.2, in which a collimated light beam is incident on-axis onto a cylindrical diffractive mirror which focuses the light at the SPR sensor-head position to incorporate various incidence angles. Surface plasmon polaritons are generated only in the longitudinal direction where the resonant coupling angle conditions are met. Thus, we need focusing power only in the longitudinal plane to incorporate all the angles between 63° and 78°, which justifies the use of a cylindrical lens. A photodetector array can then be used to extract the reflectivity data.

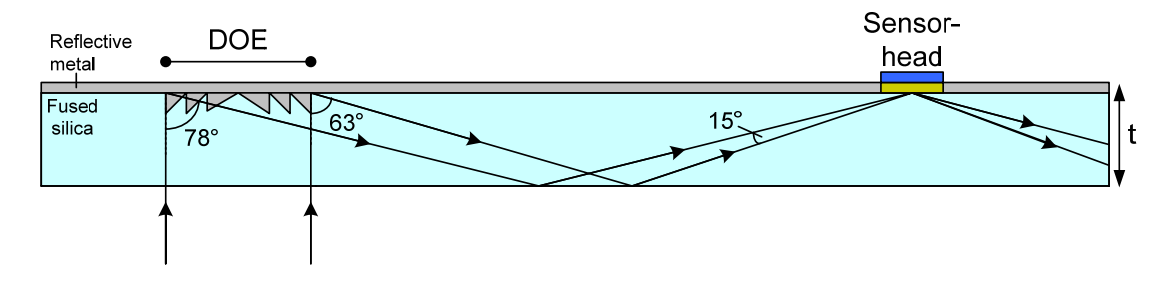


Fig. 4.2: Design configuration with on-axis illumination

Ideal as it may seem, such a design poses some serious fabrication challenges. The linear grating equation for normal incidence can be used to predict the zone periods required at the two extremes of the diffractive mirror that would deflect the light at 63° and 78° angles:

$$\Lambda \sin \theta_d = \frac{m\lambda}{n_{fs}}$$
 Eq. 4.1

where Λ is the grating period, m is the diffraction order and θ_d is the diffraction angle. For the first diffraction order i.e. m=1, the zone periods at the lens boundaries are 656.8nm and 598.3nm corresponding to the 63° and 78° angles, respectively. Thus, the zone periods would have to be modulated between the above stated periods, over the course of the lens aperture to successfully focus the beam. One of our goals with this project was to design and fabricate most of the device in-house. As a result, we did not want to design a device with feature sizes smaller than 1 μ m. To achieve the above submicron features with any sort of fidelity would, therefore, be very difficult in the McGill Microfab.

A very similar structure has already been demonstrated by Thirstrup et. al [4.5]. They fabricated a linear chirped blazed grating with submicron features (\sim 500nm) using laser beam holography combined with an injection molding process. At such small scales, it is quite difficult to fabricate devices with high precision and as expected, the diffraction efficiency of the devices in the above mentioned reference were quite low \sim 33%. The

unwanted scattered light contributes to noise in the system, and consequently, the detection limit of the sensor suffers.

In order to obtain devices with high diffraction efficiency and larger feature sizes, the only viable option is off-axis illumination, i.e. angular incidence of light onto the DOE as opposed to normal incidence. Intuitively, the focusing power requirements of the diffractive mirror can be minimized by choosing an incidence angle that lies in the middle of the desired angular range (63°-78°). Thus, an off-axis angle of 70° was chosen to maximize the mirror zone-periods, and thereby relaxing the fabrication constraints, as illustrated in Fig. 4.3.

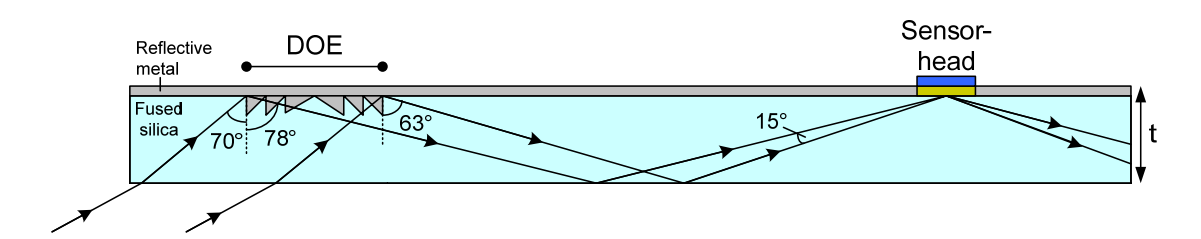


Fig 4.3: Design configuration with off-axis illumination

For such a setup, the linear grating equation for angular incidence can be used to again estimate zone periods of the two extremes of the required diffractive lens:

$$\Lambda(\sin\theta_d - \sin\theta_i) = \frac{m\lambda}{n_{fs}}$$
 Eq. 4.2

where θ_i is the angle of incidence and θ_d is the angle of the diffraction in the *m*th order. For the first diffraction order and $\theta_i = 70^\circ$, the zone periods at the lens boundaries are 12.02µm and 15.22µm corresponding to the 63° and 78° angles, respectively, which are almost 20 times larger than the feature sizes required for the normal incidence configuration. The advantage of having such large features is that we can then design a multi-level structure, as opposed to a binary (2-level) structure, to enhance the diffraction

efficiency of the DOE. The design and performance of the DOE are dealt with in detail in Chapters 5 and 6.

Using simple trigonometry, the aperture of the DOE can be determined by:

Aperture length =
$$2t(\tan 78^{\circ} - \tan 63^{\circ})$$
 Eq. 4.3

where t is the thickness of the substrate. The aperture length varies linearly with t; an increase in thickness would result in a bigger DOE, with a larger number of zones but with the same minimum feature size. A nominal substrate thickness of 1mm was chosen to give a reasonable aperture size of 5.484mm. This, however, raises another issue; coupling a beam, large enough to illuminate a 5.48mm aperture, to a 1mm thick substrate at a 70° incidence angle is not straightforward. The simplest solution is shown in Fig. 4.4(a), where a 30mm thick fused silica coupling slab is glued to the bottom of the substrate. The coupling slab has a 2µm deep ridge patterned on it, which creates an air gap once the substrate is glued on top. The air gap is used to totally internally reflect the light once it is reflected off the DOE. UV curing glue can be used to perform the dual task of gluing and providing some index-matching between the substrate and coupling slab. Many other elegant and more complicated designs were envisioned to provide coupling and for achieving the 70° incidence angle; however, in the interest of devising a first prototype device, we opted to go with the simplest configuration possible.

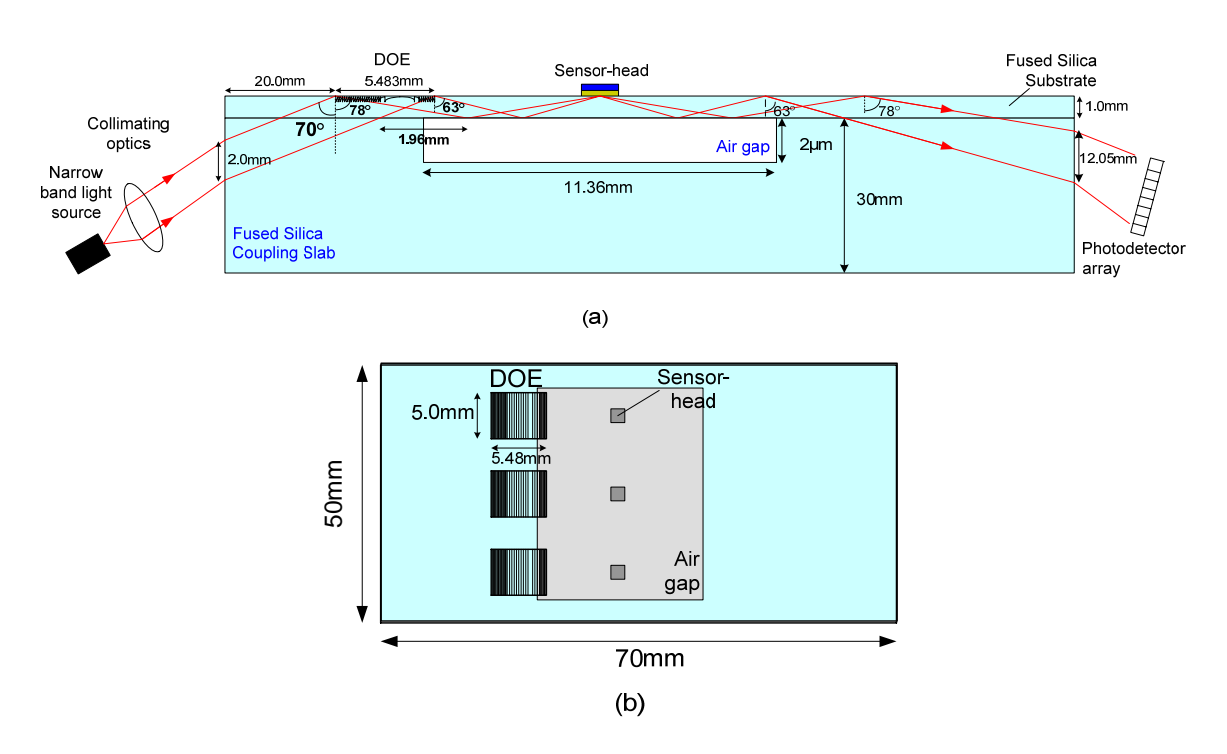


Fig. 4.4: Integrated SPR sensor schematic: (a) Cross-sectional view, (b) Top view.

The total size of the device is 70x50x31mm. The width was generously chosen to be 50mm to allow for any microfluidics setup on top and to accommodate a couple extra DOEs for testing and diagnostic purposes. The width of one DOE is 5.0mm, and can allow for multi-channel sensing if multiple sensing spots are immobilized on the surface. A single DOE is placed 20mm from one edge of the substrate to allow a collimated beam of light with 2.0mm beam diameter to completely illuminate the diffractive mirror. The ridge in the 30mm thick coupling slab is only 2µm deep. The position and length of the ridge is critical: the boundary of the ridge must be located within a 1.96mm span on the DOE side of the sensor-head and should have a length of 11.36mm as shown in Fig. 4.4(a), in order to allow the full beam to propagate through the device. These dimensions are calculated using simple geometry. Lastly, the thickness of the coupling slab was chosen to be 30mm to comfortably accommodate the diverging light beam at the output.

The diverging beam can be collimated by placing another DOE, symmetrically about the sensor-head, at the output side as shown in Fig. 4.5. Both designs, with single and double

DOEs, were implemented experimentally. However, devices with two DOEs are expected to be noisier due to extra stray reflections from the second DOE.

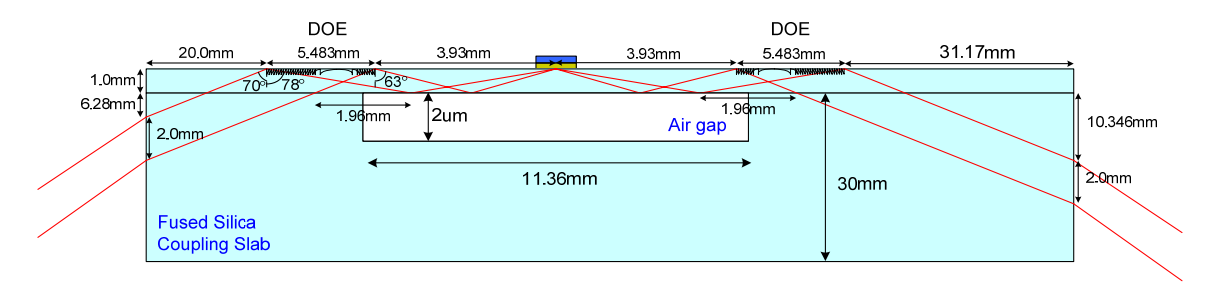


Fig. 4.5: Integrated SPR sensor configuration with an additional DOE for output collimation

4.3 Discussion

The design presented in the previous section was adopted for two primary reasons: simplicity and practicality. The sensor can be easily assembled and can provide reflectivity data for a 15° angular range simultaneously. The off-axis incidence relaxes the constraints on the DOE, allowing us to develop a high-fidelity sensor which can be fabricated and tested in-house. It is reasonably compact with plenty of room for shrinking the dimensions further. Many DOEs can be placed in parallel together to create a multichannel device with independent channels. Conversely, multichannel sensing can be performed by having multiple sensing spots immobilized using an integrated microfluidics device. The flatness of the sensor is great for developing simple and effective microfluidics on top of the substrate to deliver analytes to the sensor-head. It also opens up the exciting possibility of using imprinting and injection molding techniques to produce cheap, disposable yet accurate devices.

The configuration also has some disadvantages. For instance, achieving the required angle of incidence precisely, can be a challenge and could be a source of error in the system. Also the requirement of a coupling slab to couple the light successfully into the substrate is an extra expense and makes the device bulkier. Additional micromachining is required to fabricate the ridge in the coupling slab. Lastly, an index-matching gel is

required to fill the tiny but existent air gap between the substrate and the coupling slab once they are placed together. However, these minor setbacks are clearly outweighed by the advantages and experimental opportunities this prototype device creates.

4.4 References

- [4.1] S. Sinzinger, J. Jahns, "Microoptics", Wiley-VCH, (1999)
- [4.2] G. J. Swanson, "Binary Optics Technology: Theoretical limits on the diffraction efficiency of multilevel diffractive optical elements", MIT Technical Report 914 (1991)
- [4.3] M. B. Stern, "Pattern transfer for diffractive and refractive microoptics", Microelectronic Engineering, Vol. 34, 299 319 (1997)
- [4.4] J. Melendez, R. Carr, D. U. Bartholomew, K. Kukanskis, J. Elkind, S. Yee, C. Furlong, and R. Woodbury, "A commercial solution for surface plasmon sensing," *Sensors and Actuators B-Chemical*, vol. 35, no. 1-3, pp. 212-216, Sept.1996)
- [4.5] C. Thirstrup, W. Zong, M. Borre, H. Neff, H. C. Pedersen, and G. Holzhueter, "Diffractive optical coupling element for surface plasmon resonance sensors," *Sensors and Actuators B: Chemical*, vol. 100, no. 3, pp. 299-309, May2004

Chapter 5: DOE Surface-relief Profile Modeling

As mentioned in the previous chapters, the DOE required for our application is a cylindrical diffractive mirror. This chapter is focused on modeling the surface relief profile of mirror.

5.1 Cylindrical Diffractive Mirror Model

Typically, diffractive optical elements are designed by converting the desired phase distribution of a refractive element to a diffractive thickness profile [5.1-2]. Bendickson et al. [5.3] have presented a very intuitive model based on optical path differences for obtaining the thickness profiles of cylindrical metallic diffractive mirrors. Two types of designs are presented: the first one ignores the thickness of the mirror by treating it as an infinitely thin phase shifting element, referred to as the Zero-thickness design. The second is the Finite-thickness design which takes into account the individual thickness of each zone.

5.1.1 Zero-thickness Design

The geometry for the Zero-thickness design is shown in Fig. 5.1. S1 is the dielectric region with refractive index n_d whereas S2 is metallic region that forms the structure of the mirror. The positive and negative zone boundaries are denoted by x_m^{\pm} . B⁻ and B⁺ denote the two extremities of the mirror. Any beam incident on the mirror gets focused to a point (x_f, f) in the focal plane. The optical path difference accumulated by a ray incident at x_0 should be $m\lambda_1$ less than that of a ray incident at x_m^{\pm} , the inner boundary of the mth zone, where λ_1 is the wavelength in the region S1. This condition can be mathematically used to locate the zone boundaries:

$$x_m^{\pm} = \left(-m\lambda_1 \sin \alpha \pm \sqrt{(m^2\lambda_1^2 + 2m\lambda_1 f \cos \alpha)}\right) \sec^2 \alpha \qquad \text{m} = 1, 2, \dots,$$
 Eq. 5.1

where α is the angle of incidence, m is the zone number and f denotes the focal length of the mirror.

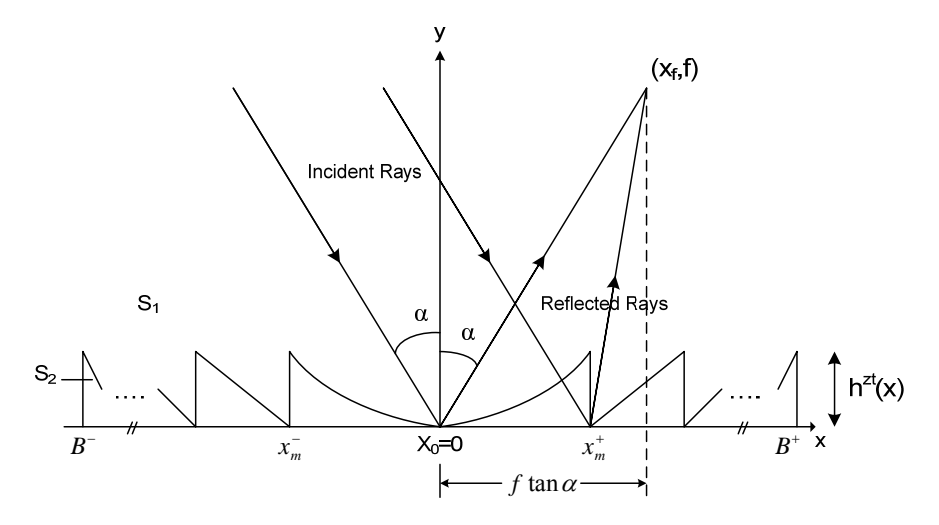


Fig. 5.1: Geometry used to derive the Zero-Thickness model

Once the zone boundaries are located, the phase difference can be used to determine the mirror profile. The phase difference between a ray incident at x_0 and a ray incident anywhere else on the mirror must be an integer multiple of 2π . This condition translates into the thickness profile of the mirror to be

$$h^{zt}(x) = \frac{1}{2} \left[x \sin \alpha + ((x - x_f)^2 + f^2)^{1/2} - f(\cos \alpha + \tan \alpha \sin \alpha) - m\lambda_1 \right]$$
 Eq. 5.2 for $x_m^+ \le x \le B^+$ if $x \ge x_0$ and $x_m^- \le x \le B^-$ if $x \le x_0$

The reader is referred to [5.3] for a detailed derivation of the above equations. The continuous thickness profile can be converted to a discretized multi-level profile by solving:

$$h^{zt}(x_{m,i}^{\pm}) - i\frac{h^{\max}}{N} = 0$$
 for $i=1,2,...,N-1$

where N is the number of levels, h^{max} is the maximum thickness and $x_{m,i}^{\pm}$ is the transition point for the *i*th level within the *m*th zone.

5.1.2 Finite-thickness Design

The simplified Zero-thickness design discussed earlier works quite well for on-axis configurations, and off-axis configurations with small incidence angles. However, for large angles of incidence, there is a marked degradation in the performance of the model, especially in terms of diffraction efficiency. Thus, for our configuration, with a large angle of incidence of 70°, there is a definite need for a more accurate model.

The geometry for the Finite-thickness design is shown in Fig. 5.2. The zone boundaries are located exactly the same way as those for the Zero-thickness design, using Eq. 5.1; however, the maximum thickness of each zone is no longer assumed to be constant. In this design, the surface profile for each zone is determined independently. For constructive interference of all the rays reflected from the *m*th zone of the mirror the following equation must hold, which is expressed mathematically as

$$k_1 \delta(x) + k_1 [(x - x_f)^2 + (f - h^{fi}(x))^2]^{1/2} - k_1 [(x_m^{\pm} - x_f)^2 + f^2]^{1/2} = 0$$
 Eq. 5.4

where $k_1=2\pi/\lambda_1$ is the wave-vector, $h^{ft}(x)$ is the thickness profile of the mirror and $\delta(x)$ is the phase difference between a ray incident at the zone boundary x_m^{\pm} and a ray incident anywhere in the *m*th zone, before reflection.

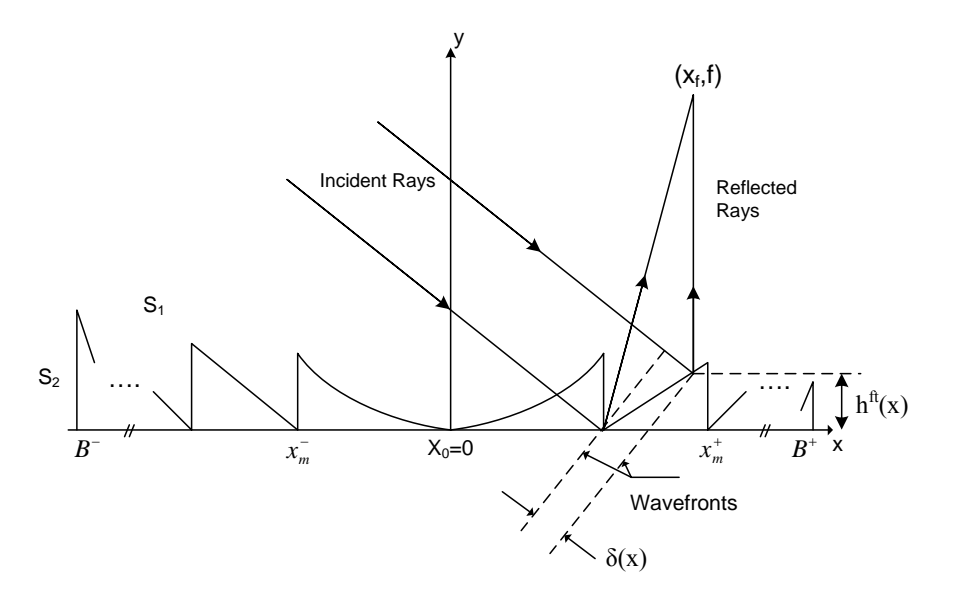


Fig. 5.2: Geometry used to derive the Finite-Thickness model

The thickness profile can then be expressed as

$$h^f(x) = \frac{C_2 - \sqrt{C_2^2 - 4C_1C_3}}{2C_1},$$
 where
$$C_1 = \sin^2 \alpha$$
 Eq. 5.5
$$C_2 = -2f(1 + \cos^2 \alpha) - 2\cos \alpha (f \tan \alpha \sin \alpha - x \sin \alpha + m\lambda_1),$$

$$C_3 = (x - f \tan \alpha)^2 + f^2 - (f \cos \alpha + f \tan \alpha \sin \alpha - x \sin \alpha + m\lambda_1)^2$$
 for $x_m^+ \le x \le B^+$ if $x \ge x_0$ and $x_m^- \le x \le B^-$ if $x \le x_0$

For the Finite-thickness design, the maximum thickness of each zone is not constant, as illustrated in Fig. 5.2. This sort of DOE becomes almost impossible to fabricate with lithographic techniques because the zones cannot be discretized into N equal levels. A viable solution is to take the average thickness of all the zones and use Eq. 5.6 to discretize the structure.

$$h^{ft}(x_{m,i}^{\pm}) - i\frac{h^{avg}}{N} = 0$$
 for $i=1,2,...,N-1$ Eq. 5.6

where h^{avg} is the average thickness of all the zones in the mirror.

5.2 Analytical Modeling Results

In this section, the results from applying the cylindrical mirror models to our sensor configuration are presented. Figure 5.3 shows the unfolded geometry of the sensor configuration. The angle of incidence is 70° and the focal length of the mirror is twice the thickness of the substrate. A ray reflected off from the center of the lens reaches the focus at the same angle of 70° . In order to have a scan range between 63° and 78° , we simply need to locate the boundaries B^{+} and B^{-} for the off-axis mirror that give the required angles.

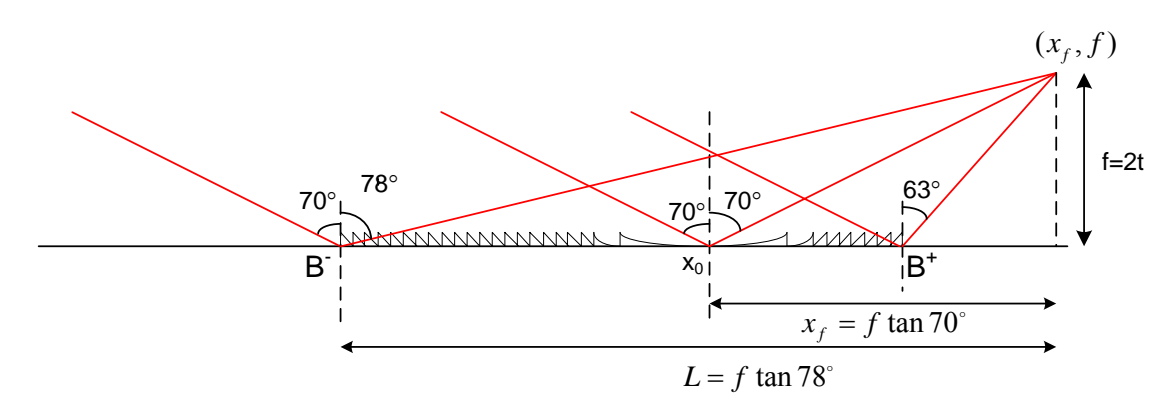


Fig. 5.3: Unfolded sensor geometry

The distance L between the sample and mirror is given by $L = f \tan 78^{\circ}$ as illustrated, where f = 2mm is the focal length equal to twice the thickness of the fused silica substrate. The required zone boundary B to achieve a 78° reflection is then simply located at a distance $L - x_f = f (\tan 78^{\circ} - \tan 70^{\circ})$ from the center. Similarly, the boundary B needed to achieve a reflection angle of 63° is then located at a distance of $f (\tan 70^{\circ} - \tan 63^{\circ})$ from the center. These distances are then used to solve Eq. 5.1 for m.

The results show that in order to achieve an angular scan range between 63° and 78° , we would need a cylindrical mirror with an aperture of 5.483mm, giving it an f-number of 0.365. 160 negative zones are required with the minimum zone width being $15.204\mu m$ and 56 positive zones are required with the smallest zone having a width of $12.02\mu m$.

Once the zone boundaries are located, Eq. 5.3 can be used to obtain the thickness profile using the Zero-thickness model as shown in Fig. 5.4. The maximum optimum thickness of each zone is 292.6nm.

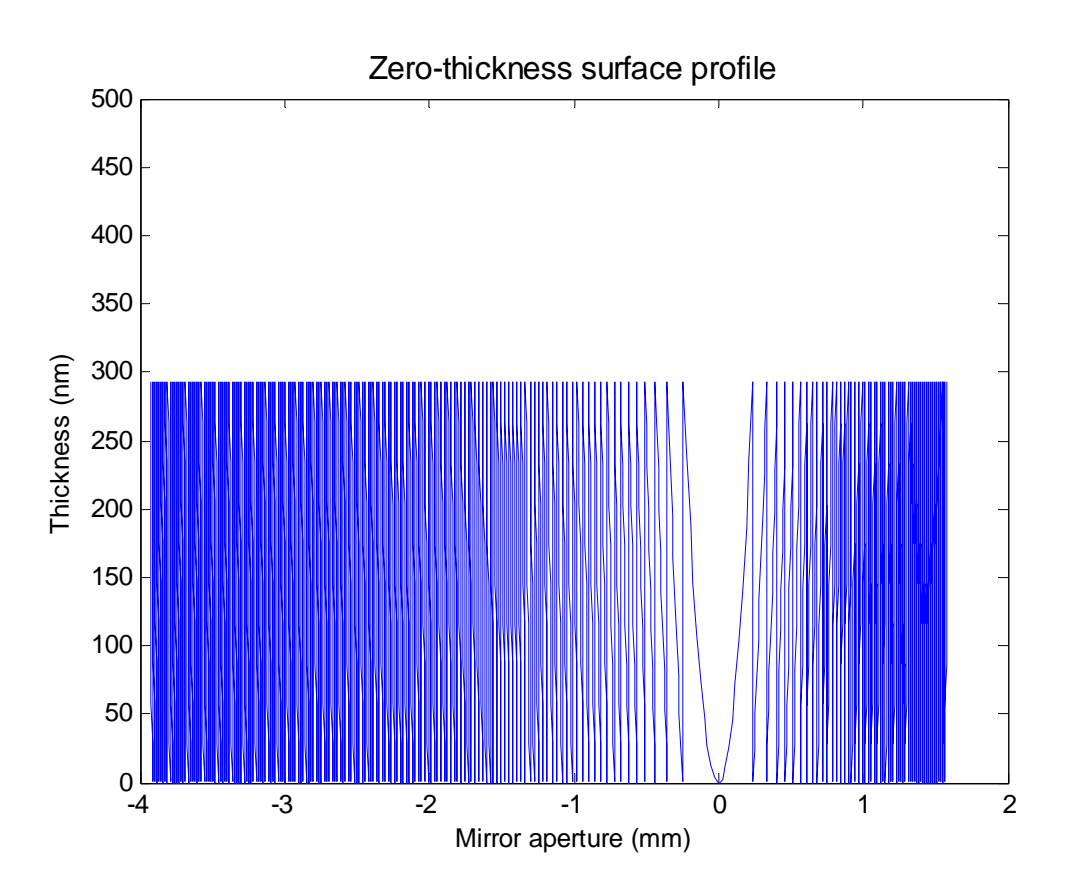


Fig. 5.4: Continuous mirror thickness profile obtained using the Zero-thickness model

Similarly, the finite-thickness profile, illustrated in Fig. 5.5, can be obtained using Eq. 5.4.

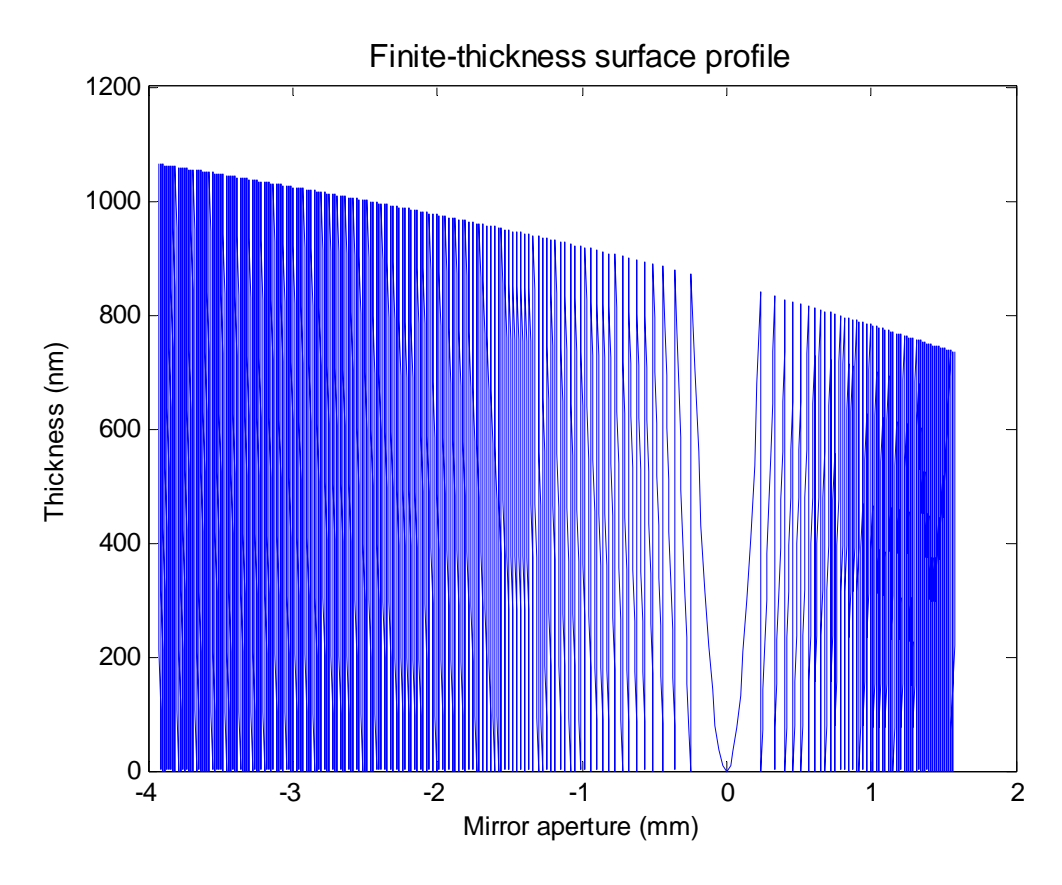


Fig. 5.5: Continuous thickness profile with zone height varying between 1.065μm and 0.734μm

It is evident that the maximum zone thicknesses are not constant. The height varies between $1.065\mu m$ and $0.734\mu m$, which is significantly different from the constant 292.6nm zone height of the Zero-thickness surface profile. A thorough comparison of the performance of these two designs is presented in the subsequent chapters.

Lastly, we need to discretize the above continuous profiles since it is impossible to fabricate continuous blazed profiles using microlithographic techniques. The most important parameter in the discretization process is the number of levels N, which is usually of the form $N=2^l$, where l is the number of photo-masks that will be employed in the fabrication process. The choice of levels depends purely on our ability to fabricate small features since the feature sizes decrease as the number of levels increase. The smallest feature size in the thickness profiles is $12.02\mu m$ – the width of the smallest positive zone in the mirror, and as mentioned before, the smallest feature size we can fabricate in-house is $1\mu m$. Thus, we can not use more than 8 (2^3) levels.

Eq. 5.6 can then be used to discretize the continuous thickness profiles. Discretization of the Zero-thickness design is trivial. For the Finite-thickness design, however, the average maximum zone thickness of 0.90µm must be used in Eq. 5.6. The discretized 8-level finite-thickness profile of the mirror is shown in Fig. 5.6. Each step in the staircase has a height of 112.5nm.

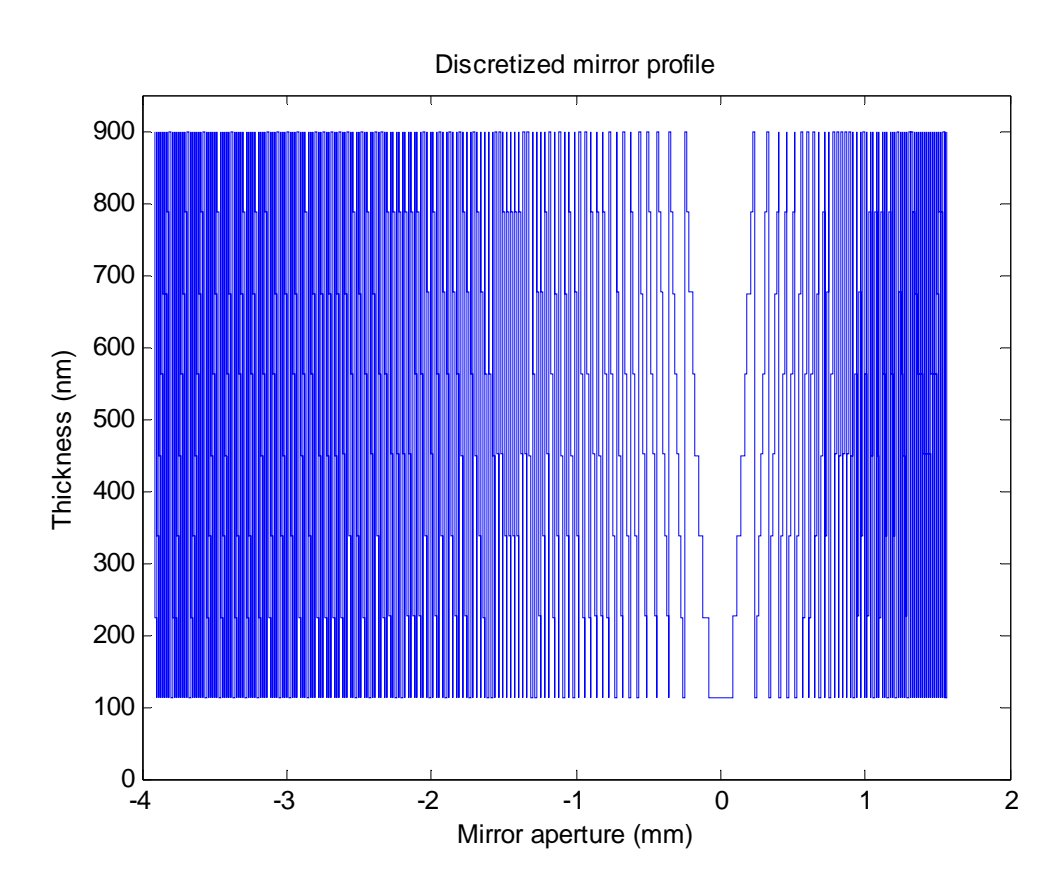


Fig. 5.6: Discretized 8-level finite thickness surface profile with fixed zone height of 0.9μm. Each phase step has a height of 112.5nm

5.3 References

- [5.1] J.A. Jordan, Jr. P. M. Hirsch, L. B. Lesem, and D. L. Van Rooy, "Kinoform Lenses", Applied Optics 9, 1883 1887 (1970)
- [5.2] E. Noponen, J. Turunen and A. Vasara, "Electromagnetic theory and design of diffractive-lens arrays", J. Opt. Soc. Am. A, Vol. 10, 434-443 (1993)
- [5.3] J. M. Bendickson, E. N. Glytsis and T. K. Gaylord, "Metallic surface-relief on-axis and off-axis focusing diffractive cylindrical mirrors", J. Opt. Soc. Am. A, Vol. 16, 113 130 (1999)

Chapter 6: Phase and Ray-trace Modeling

This chapter focuses on developing the phase profile of the diffractive mirror modeled previously. A ray-tracing software package – Code V, is then used to simulate the SPR sensor optics.

6.1 Background theory

Previously, we directly obtained the thickness profile of the cylindrical mirror using optical path differences. Typically, diffractive optic design is a two step procedure where a desired phase profile is first converted into a diffractive phase profile, which can be then translated to a thickness profile [6.1,6.2]. The diffractive phase distribution can simply be obtained by taking the modulo- 2π of the continuous phase profile, mathematically expressed as:

$$\Phi_d(x) = \Phi(x) + 2m\pi, \qquad x_m < x < x_{m\pm 1}$$
 Eq. 6.1

where $\Phi(x)$ represents the desired continuous phase distribution of a corresponding refractive element, $\Phi_d(x)$ is the diffractive phase profile and x_m represents the zone boundaries of the diffractive profile [6.3]. The procedure is illustrated in Fig. 6.1.

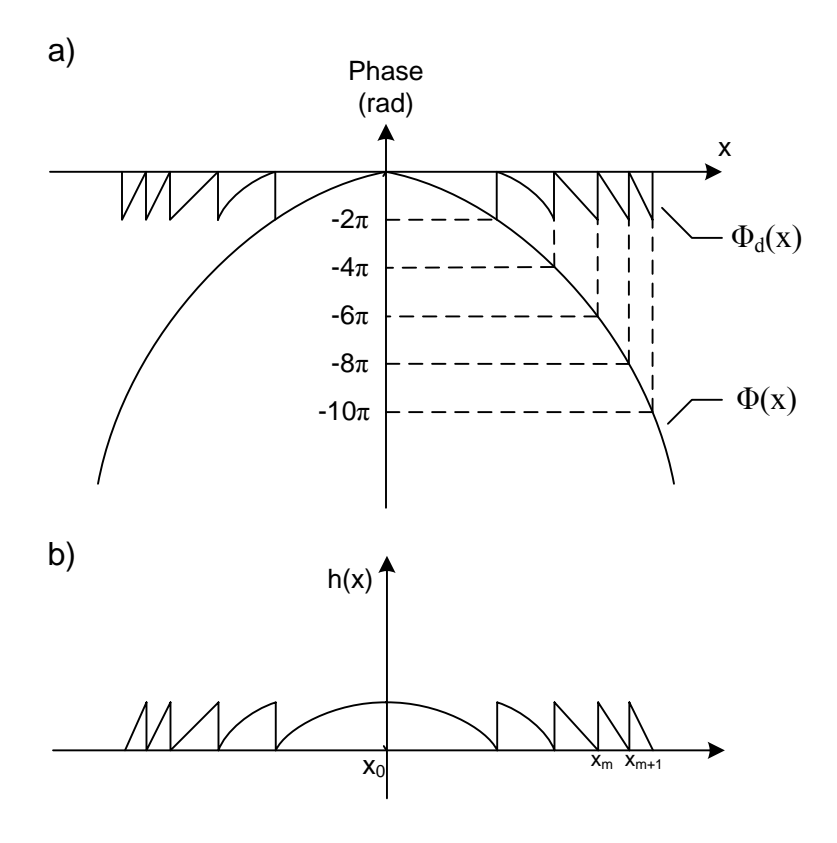


Fig. 6.1: (a) Phase profile of a diffractive lens, (b) thickness profile

The phase distribution and the thickness profile are typically assumed to be linearly related in literature [6.1-3] as follows:

$$h(x) = \frac{\Phi_d(x)}{k\mu}$$
 Eq. 6.2

where $k = 2\pi/\lambda$ is the wave number, h(x) is the thickness profile and $\mu = -2n_0$ is the constant of proportionality for a reflective microrelief, where n_0 is the refractive index of the adjacent medium.

The above equation is an approximation because it does not take into account the local slopes of the incident and output beams or the orientation of the substrate with respect to the incident beam. A more generalized model is presented in [6.4] that is valid for arbitrary angles of incidence and substrate curvature, and takes into consideration the

above mentioned approximations. The constant of proportionality μ for a reflective diffractive lens according to this more accurate model is given by:

$$\mu = -n_0(\cos\theta_i + \cos\theta_d)$$
 Eq. 6.3

where θ_i is the angle of incidence and θ_d is the angle of diffraction off the lens.

6.2 Ray-trace simulation

Code V is a ray-tracing software package provided by Optical Research Associates, which was used to model the beam-steering optics of the SPR sensor. Designing the cylindrical mirror was the primary challenge with the software. The diffractive mirror was modeled as an infinitely thin phase screen whose phase function is defined by an arbitrary phase polynomial. The software can then optimize the coefficients of the polynomial to achieve the required focusing. An alternative to the thin phase screen model is the well-known Sweatt model which has been traditionally used to design DOEs and holographic lenses [6.5]. The Sweatt model allows modeling a diffractive lens using a simple refractive lens with a very high refractive index $\sim 10^3$. However, a huge disadvantage is the fact that accuracy of ray-tracing equations fall drastically for large refractive index values making ray-tracing analysis ineffective.

Fig. 6.2 shows the Code V ray-trace model for the first diffraction order. The light is incident at an angle of 60.22° to the vertical and then gets refracted to an angle of 70° before it reaches the diffractive mirror. The light is then reflected twice, inside the 1mm thick substrate, before being coupled out.

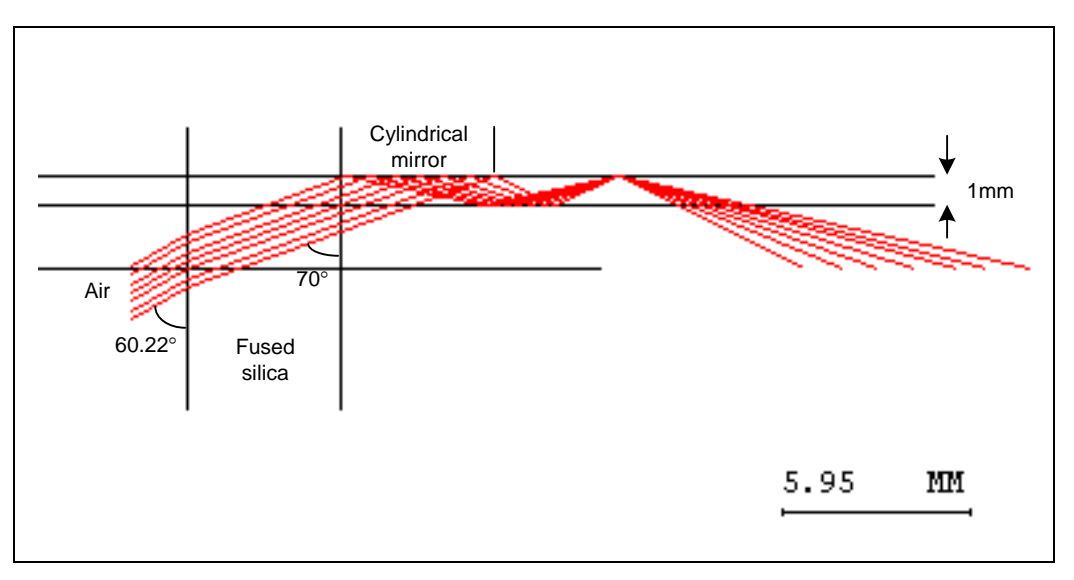


Fig. 6.2: Code V ray-tracing model

6.2.1 Phase Modeling

Since our mirror is asymmetrical, i.e. the number of positive and negative zones is not equal, we would expect the phase profile to be asymmetrical as well. The built-in general phase polynomial for kinoforms in Code V is of the form of $G(x) = \frac{2\pi}{\lambda} \sum_{i=0}^{N} g_i x^{2i}$, which is ideal for modeling symmetrical phase profiles. One way to simulate asymmetrical phase profiles more accurately is to use two polynomials, one each for the negative and positive sides of the mirror. The customized polynomial then had the form:

$$U(x) = \frac{2\pi}{\lambda} \{ N(x) + P(x) \} = \frac{2\pi}{\lambda} \left\{ \sum_{i=0}^{4} n_i x^{2i} \bigg|_{x < 0} + \sum_{i=0}^{4} p_i x^{2i} \bigg|_{x \ge 0} \right\}$$
 Eq. 6.5

where n_i and p_i represent the phase coefficients of the negative-side and positive-side polynomials, respectively. The maximum value of i was chosen to be 4 because there we're no notable improvements in the system for a larger number of coefficients. Once optimization was performed, the customized polynomial showed a distinct improvement

over the general polynomial in terms of image quality. The optimized phase coefficients are tabulated below:

Negative-side		Positive-side	
n ₀	0.00	p_0	0.00
n ₁	-8.8053x10 ⁻³ /mm ⁻¹	p ₁	-1.0823x10 ⁻² /mm ⁻¹
n ₂	3.8595x10 ⁻⁴ /mm ⁻³	p ₂	-1.0431x10 ⁻³ /mm ⁻³
n ₃	-2.1543x10 ⁻⁵ /mm ⁻⁵	p ₃	2.9137x10 ⁻⁵ /mm ⁻⁵
n ₄	5.0570x10 ⁻⁷ /mm ⁻⁷	p ₄	-1.3203x10 ⁻⁶ /mm ⁻⁷

Table 6.1: Optimized phase polynomial coefficients for Code V diffractive mirror model

Phase profile comparisons of the Code V model and the analytical models developed in Chapter 5 are shown in Fig. 6.3. The phase profiles of the Zero-thickness and Finite-thickness models have been obtained from the thickness profiles using Eqs. 6.2-3.

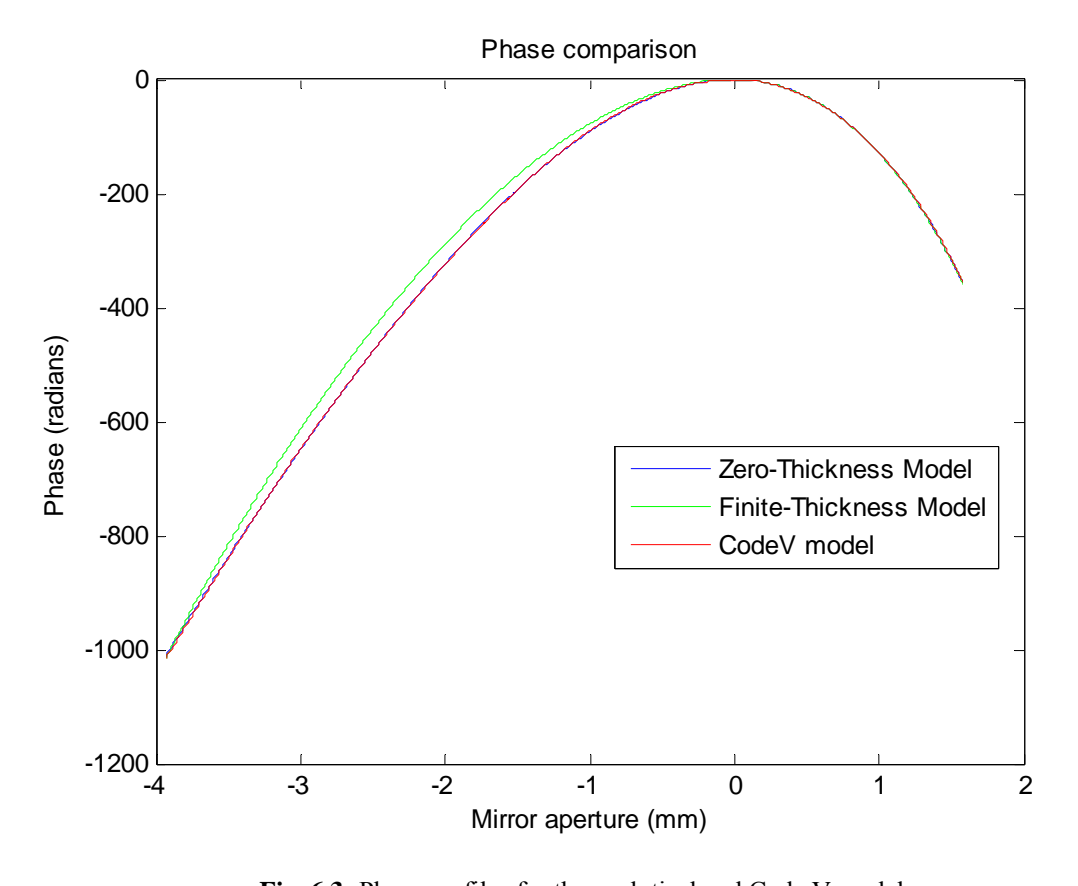


Fig. 6.3: Phase profiles for the analytical and Code V models

The Code V model and the Zero-thickness model are matched very closely; as such the phase profiles are barely distinguishable. The finite-thickness model phase profile is a bit off owing to some geometric simplifications used in developing the phase [6.4] and thickness [6.6] models. The results prove the validity of the analytic designs, by showing that they do provide, almost exactly, the phase-shift required to achieve the desired focusing.

6.2.2 System Performance Metrics

Various performance metrics for the whole system, simulated with Code V, are presented in this section. The geometric spot size at the focus is 210µm as shown by the spot diagram in Fig. 6.3. Note that there is focusing only in one direction since the mirror is cylindrical. However, the line spread function (Fig. 6.4) shows that most of the power is actually confined within a much smaller region of about 50µm. It must be noted that no rigorous diffraction analysis is performed in Code V, as such, the diffractive mirror is assumed to have 100% diffraction efficiency in the linespread function calculations.

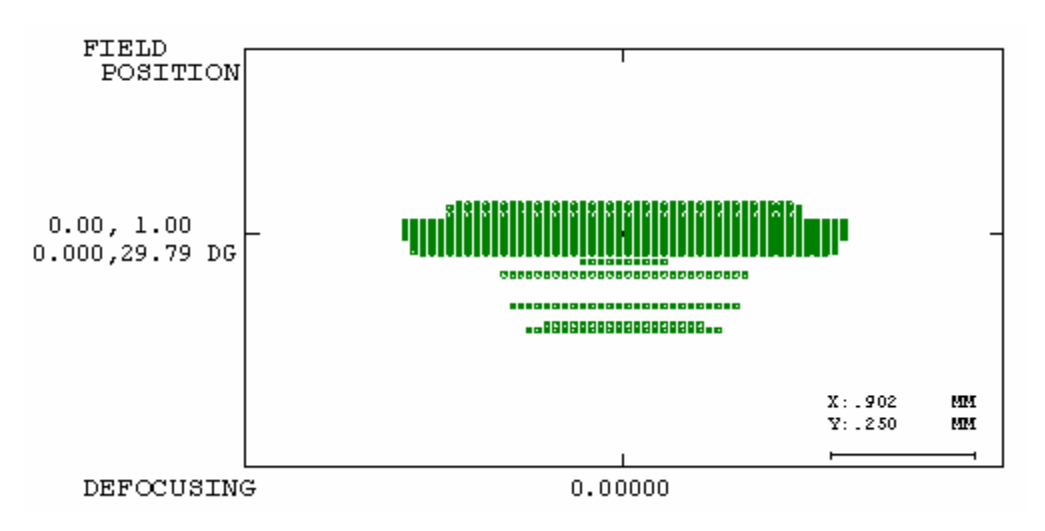


Fig. 6.3: Geometric Spot Diagram: spot size is 210 μm

Diffraction intensity profile linespread function

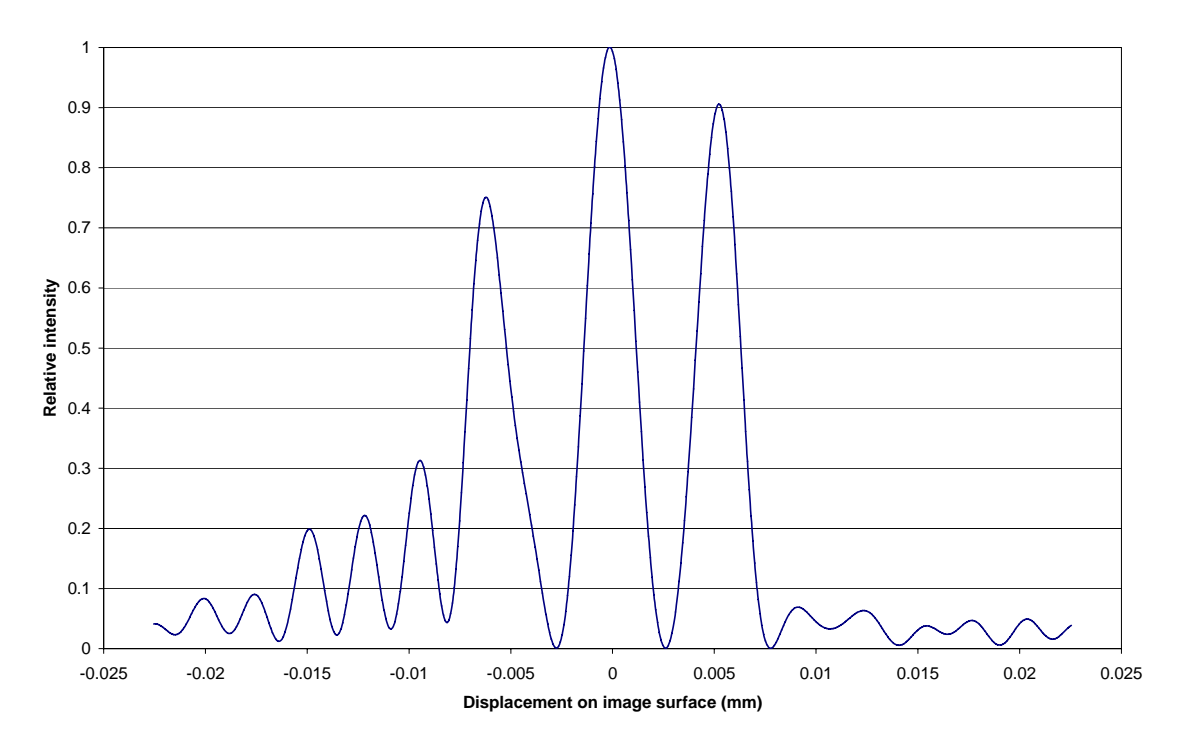


Fig. 6.4: Linespread function showing intensity profile at the sensor-head (focus). Most of the power is confined within a 50μm region

The transverse ray aberrations are shown in Fig. 6.5. The results are limited by higher-order spherical aberrations. The negative aperture of the mirror, indicated right of the origin in the figure, shows larger aberrations than the positive side, corresponding with the spot diagram data. This is an inherent result of the largely off-axis nature of the configuration and the choice of phase polynomial that is used to model it. However, more advanced optimization procedures in Code V could be used to slightly improve the results.

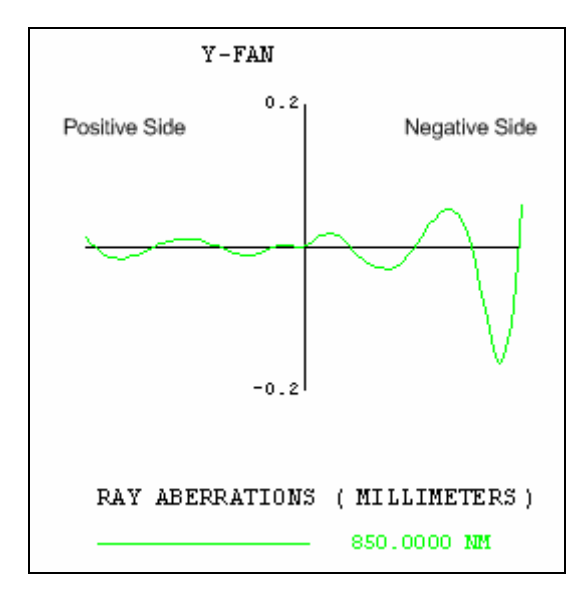


Fig. 6.5: Transverse ray aberration curve

The model for the entire system is shown in Fig. 6.6. The output beam has a diameter of 12.05mm at the output edge of the sensor. Fig. 6.7 shows the beam intensity profile at the output edge obtained using the beam-propagation option (BPR) in Code V. The BPR option incorporates the effects of diffraction by using a combination of near-field and far-field diffraction, as opposed to ray-tracing and is therefore more accurate. The intensity profile shown in Fig. 6.7 is non-uniform with most of the power being concentrated in the center of the image.

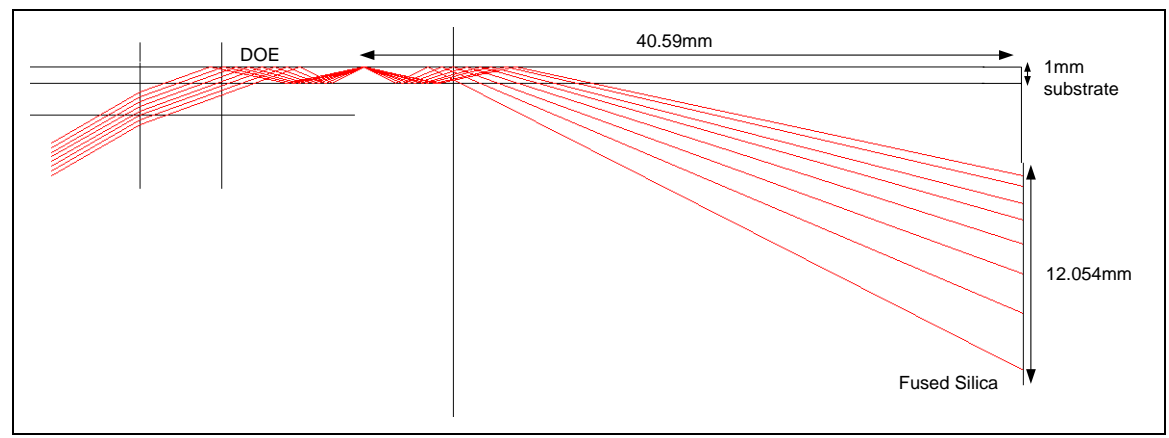


Fig. 6.6: Code V model of the SPR sensor with the image plane located at the output edge of the sensor

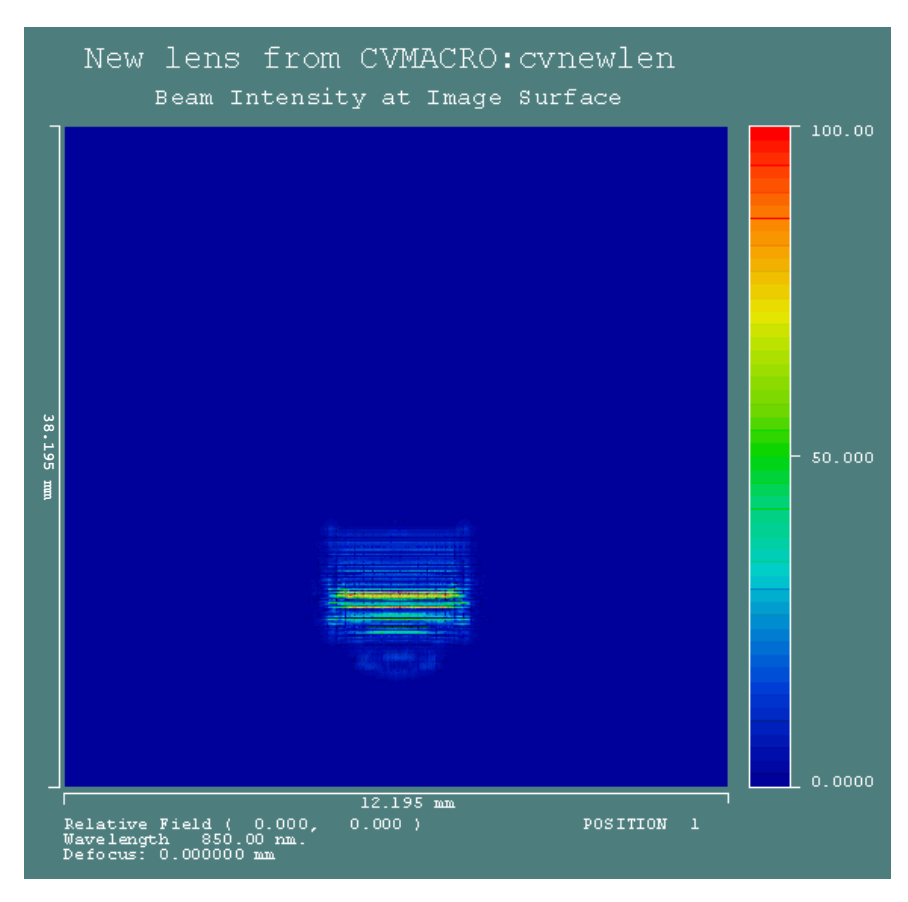


Fig. 6.7: Intensity profile at the output edge of the SPR sensor generated using the BPR option in Code V

6.3 References

- [6.1] J. A. Jordan, P. M. Hirsch, L. B. Lesem, and D. L. Vanrooy, "Kinoform Lenses," *Applied Optics*, vol. 9, no. 8, p. 1883-&, 1970.
- [6.2] E. Noponen, J. Turunen, and A. Vasara, "Electromagnetic Theory and Design of Diffractive-Lens Arrays," *Journal of the Optical Society of America A-Optics Image Science and Vision*, vol. 10, no. 3, pp. 434-443, Mar.1993
- [6.3] H. Nishihara and T. Suhara, "Micro Fresnel Lenses," *Progress in Optics*, vol. 24, pp. 1-37, 1987.
- [6.4] M. A. Golub, "Generalized conversion from the phase function to the blazed surface-relief profile of diffractive optical elements," *Journal of the Optical Society of America A-Optics Image Science and Vision*, vol. 16, no. 5, pp. 1194-1201, May1999.

- [6.5] L. N. Hazra, Y. Han, and C. A. Delisle, "Kinoform Lenses Sweatt Model and Phase Function," *Optics Communications*, vol. 117, no. 1-2, pp. 31-36, May1995.
- [6.6] J. M. Bendickson, E. N. Glytsis and T. K. Gaylord, "Metallic surface-relief on-axis and off-axis focusing diffractive cylindrical mirrors", J. Opt. Soc. Am. A, Vol. 16, 113 130 (1999)

Chapter 7: Diffraction Efficiency Modeling

This chapter is devoted to the diffraction efficiency analysis of the multi-level diffractive mirror designed in Chapter 5 using scalar and rigorous diffraction theories. Brief overviews of the scalar and rigorous methods employed, are provided. Simulation results are presented, thereafter.

7.1 Background Theory - Diffraction Efficiency

The discussion in the previous chapters focused on achieving the desired phase or thickness profile of the diffractive lens/mirror. The ability of diffractive lenses to split light into multiple beams raises the question: how much energy does each beam carry? The answer lies in finding the diffraction efficiency (DE); a key parameter that is used to determine the performance of any DOE. The absolute diffraction efficiency for a linear grating is defined as the fraction of incident light intensity that is directed into the desired diffraction order. For a diffractive lens/mirror, however, the definition is more ambiguous. A number of definitions for DE can be found in literature [7.1], however, the definition for DE used in this thesis is: the ratio of intensity of light within a small defined region on the image plane to the total intensity of the incident light.

Calculating the diffraction efficiency can be quite a challenge. DE is a function of a number of parameters such as the refractive index of the substrate, wavelength, angle of incidence and polarization of the incident light, and the surface profile. In theory, Maxwell's equations can be used to calculate, exactly, the diffraction efficiency of any DOE; however, it is not possible to obtain exact solutions most of the time in practice. A number of theories and methods have been developed for solving the DE problem which can be divided into two regimes: scalar methods and rigorous methods. Scalar methods are simpler and easier to implement, but are less accurate than rigorous methods, which have a drawback of being computationally intensive. The following sections provide an overview of the scalar and rigorous techniques that have been employed in this thesis.

7.2 Scalar Method

7.2.1 Scalar diffraction theory

The scalar theory of diffraction for a surface relief structure is based on simplifying the Maxell's equations by assuming that light can be treated as a scalar as opposed to a vector field and that the electric and magnetic field components are uncoupled [7.2]. Also assumed is the absence of external excitement sources, the medium is linear, homogeneous and isotropic and that the incident wave is time-harmonic. These assumptions lead to the Helmholtz equation which is valid for both the electric and magnetic fields and all their components.

$$(\nabla^2 + k^2)\vec{L} = 0$$
 Eq. 7.1

where k is the wave-vector and L can be any of the E or H field components. It must be stressed that the vectorial nature of light can only be ignored if there is little coupling between the various components of the E and H fields. Coupling can be enhanced if the medium is not homogeneous or by introducing boundary effects such as those caused by apertures and diffractive elements with sharp transition points. Thus, the scalar approximation will be valid only if the DOEs have large features compared to the wavelength, so that the medium appears homogeneous due to the relatively large spacing between the transition points, thereby minimizing the boundary effects.

Scalar theory for focusing continuous diffractive mirrors has been presented in [7.3] which is based on applying the Green's Theorem to the Helmholtz equation. However, the method is mathematically quite arduous. In theory, the diffraction efficiency of an arbitrary DOE can be directly related to the diffraction efficiency of a grating by a local linear grating approach [7.4,7.5]. To achieve this end, the focus of this section is primarily on developing a scalar diffraction theory for a surface-relief grating (multi-level).

The Fraunhofer approximation can be used to obtain an integral solution of the propagation of the light field. The Fraunhofer approximation is valid when the image plane is located far enough ($z\gg a^2/\lambda$ where a is the width of the diffractive aperture) so that the arriving wavefronts appear planer. Mathematically, Fraunhofer diffraction is expressed by:

$$U(f_x, f_y) = A(x, y) \int_{-\infty}^{\infty} \int_{-\infty}^{\infty} U(x_0, y_0) \exp[(-i2\pi (f_x x_0 + f_y y_0))] dx dy$$
 Eq. 7.2

where $f_x = x/\lambda z$ and $f_y = y/\lambda z$, and the initial light field $U(x_0,y_0)$ has propagated a distance z, resulting in the light field $U(f_x,f_y)$. A(x,y) is a multiplicative phase factor that can be ignored [7.6]. For a periodic structure such as a linear grating, it turns out that the diffraction efficiency can be calculated for different diffraction orders simply by a Fourier transformation of the grating reflectance function.

$$U(f_x, f_y) = F\{U(x_0, y_0)\}\$$
 Eq. 7.3

This principle has been used in [7.6] to find the scalar DE for multi-level transmission gratings. A modified version of their derivation is presented here to accommodate reflective gratings.

Figure 7.1 shows the surface relief profile of a 1-D multilevel phase grating. The grating has a period of Λ with N subperiods of width Λ /N, where N is the number of phase levels. Each phase step has a height of δ h. In order to calculate the DE of this structure, the far-field of one grating period has to be determined. This can be accomplished by the summation of the reflectances of all the subperiods within one period.

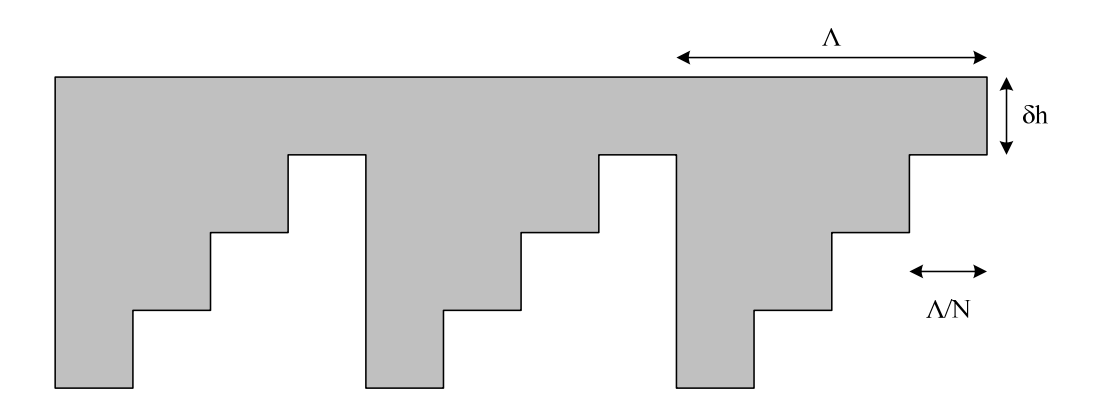


Figure 7.1: 1-D multilevel phase grating with N subperiods

Each subperiod is a rect function of width Λ/N centered at $x = (m + \frac{1}{2})\Lambda/N$, where m is an integer from 0 to N-1. Also, each subperiod imparts a phase delay (in waves) of $\phi = m\phi_0/N$ where ϕ_0 is the largest phase delay of all subperiods. The far-field distribution of one subperiod can then be expressed using Eq. 7.3 with $f_x=f_y=f$ (since grating is 1-D):

$$U_{subperoiod}(f) = \sin c \left(\frac{\Lambda f}{N}\right) \exp \left(i2\pi (m+1/2)\frac{T}{N}f\right) \exp \left(\frac{i2\pi m\phi_0}{N}\right)$$
 Eq. 7.4

The far-field amplitude distribution of an entire period can be expressed as a summation of the amplitude distributions of each subperiod:

$$U_{period}(f) = \frac{1}{N} \sum_{m=0}^{N-1} U_{subperiod}$$
 Eq. 7.5

The total energy can be calculated by including an infinite number of periods. The total energy in each diffraction order and the far-field amplitude of the *l*th diffraction order can be written as:

$$A_{l} = \exp\left(-i\pi \frac{l}{N}\right) \frac{\sin(\pi l/N)}{\pi l/N} \left(\frac{1}{N}\right) \sum_{m=0}^{N-1} \exp\left(-i2\pi(\phi_{0} - l)\frac{m}{N}\right)$$
 Eq. 7.6

The diffraction efficiency of the *l*th order is then given by $A_l A_l^*$:

$$\eta_l^N = \left\lceil \frac{\sin(\pi(\phi_0 - l))}{\pi l} \frac{\sin(\pi l/N)}{\sin(\pi(\phi_0 - l)/N)} \right\rceil^2$$
Eq. 7.7

The phase parameter ϕ_0 depends on the grating height, angle of incidence and the wavelength of light. For an N-level reflective multi-step grating ϕ_0 is given by

$$\phi_0 = -\frac{N\delta h}{\lambda} n(\cos\theta_i + \cos\theta_d)$$
 Eq. 7.8

where n is the refractive index of the substrate, δh is the step height of each phase step, and, θ_i and θ_d are the incident and diffracted angles, respectively. Eq. 7.7 in tandem with Eq. 7.8 can then be used to calculate the diffraction efficiency.

It must be stressed that the scalar theory developed above is only valid for gratings with large period-to-wavelength ratios; for grating with periods comparable to the wavelength, the scalar theory completely breaks down. The primary cause of this fall-off of the scalar model is the assumption that the phase delay that an incident wave experiences, occurs within an infinitely thin layer. Thus, the scalar theory ignores the effects of finite grating height and period-to-wavelength ratio altogether. Swanson [7.6] used geometric ray-tracing to show that DE is indeed a function of both grating depth and period and that for aperiodic structures like lenses, the depth must vary with the period in order to maximize the diffraction efficiency.

Another effect that was demonstrated with ray-tracing is known as "light-shadowing" and it must be added to our scalar theory in order to predict more accurate results. Fig. 7.2 illustrates the light shadowing effect resulting from a finite-thickness grating. The grating has a period Λ and depth d. After reflection, the light deflected in, say the first diffraction

order does not completely fill the aperture. The ratio of the area filled with light to the total area is known as the duty cycle (DC) and is equal to $\Delta\Lambda/\Lambda$.

$$DC = \frac{\Delta \Lambda}{\Lambda} = \frac{\Lambda}{\Lambda + d \tan \theta_d}$$
 Eq. 7.9

where d is the total depth of the grating and θ_d is the angle of the diffracted beam in the first order.

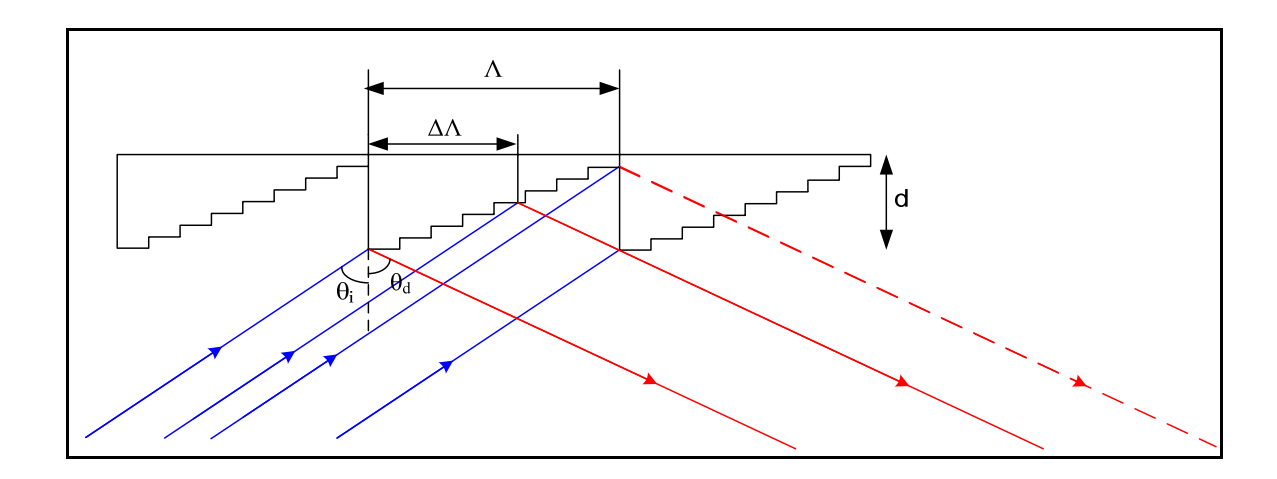


Fig 7.2: Illustration of the light-shadowing effect

Thus, the fraction of light equal to the DC is lost and new first order diffraction efficiency is given by:

$$\eta_{scalar} = DC^2 \eta_1^N$$
 Eq. 7.10

7.2.2 Local linear grating model

As mentioned in the previous section, the scalar diffraction theory is valid only for periodic structures such as gratings. Our cylindrical focusing mirror is an aperiodic structure and as such the scalar theory can not be applied directly to compute the diffraction efficiency. However, Sheng et al. [7.5] have demonstrated that the diffraction efficiency of an aperiodic structure can be calculated in a piece-wise fashion using a very intuitive local linear grating model. The aperiodic structure is basically divided into subsections consisting of M zones, where M≥10. Starting from one edge of the mirror, the subsections are formed by shifting the M-zone window by one zone each time to obtain a new subsection. The scalar (or rigorous) diffraction theory is then applied to a linear grating having a period equal to the local average of zone periods in a subsection. Finally, the mean of the diffraction efficiencies of all subsections gives the DE of the aperiodic structure.

7.3 Rigorous Method

There are several rigorous methods that can be used to analyze diffractive structures such as the boundary element method, integral method, differential method, coupled mode theory, coupled wave method, finite difference method and finite element method. The finite difference time domain (FDTD) method was employed for the purposes of this thesis. Theoretically, the FDTD method can be applied directly to our aperiodic diffractive mirror, however, due to the large aperture, the computation time would be excessively long. Therefore, we revert to the local linear grating model by applying FDTD on periodic gratings, and then averaging over the entire aperture of the mirror.

The FDTD method is based on dividing a period of the grating in a finely spaced grid. Partial derivatives of the Maxwell's Equations are then calculated for each grid space using finite differences. The E-field and H-field are calculated in a time-stepped approach: the E-field at a given instant in time depends on the stored value of the E-field and the spatial distribution of the H-field, according to the Maxwell's Equations, and the H-field has a similar dependence on the E-field. Thus, the E-field and H-field are calculated in an alternating manner along the finite grid. Multiple periods of the grating can then be included in the calculations to emulate an infinitely extended linear grating [7.7]. Details on the implementation of the FDTD method can be found in Refs [7.8,7.9].

The *FDTD Solutions* package by Lumerical Solutions Inc. [7.10] was used to perform the analysis.

7.4 Results and discussion

As mentioned earlier, the local linear grating model was employed for both scalar and rigorous modeling. Each subsection of the diffractive mirror was chosen to contain 11 zones (M=11) and all the subsections are created using the method detailed in Section 7.2.2.

For scalar modeling, the average zone period of each subsection is found and Eq. 7.7 – 7.10 are then used to calculate the diffraction efficiency for each corresponding local grating. The required parameters have all been computed in the previous chapters: N=8, l=1, d=900nm, δh =112.5nm, n=1.4525, λ =850nm, θ_i = 70° and θ_d is calculated using Eq. 4.2.

For FDTD modeling, simulations were not performed for every subsection of the mirror primarily due to long simulation times, which were in excess of 6 hours per simulation on average. Instead, 25 subsections were chosen uniformly around the aperture of the mirror and the results were interpolated between data points to obtain the trend.

The results in Fig. 7.3 show that the FDTD results complements the simpler scalar model. As expected, the scalar model provides an upper bound to the actual obtainable diffraction efficiency, calculated with FDTD. The scalar model is fairly accurate owing to the large period-wavelength ratios (>14) of the diffractive mirror. The discrepancy between the two models is larger towards the edges of the grating, where the diffraction angles become large and the periods become smaller. The largest discrepancy is around 11% towards the negative edge of the mirror, which can be attributed to the assumptions and simplifications made in the Fraunhofer diffraction theory.

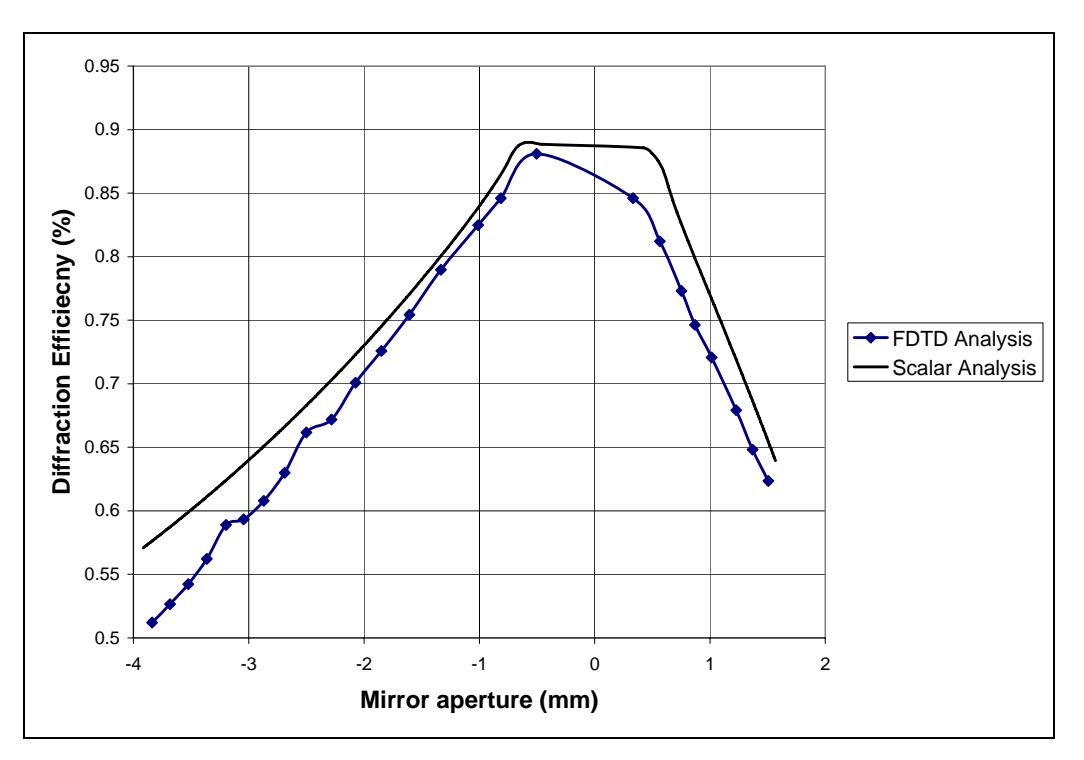


Fig. 7.3: Diffraction efficiency analysis using scalar and rigorous methods

The mirror has high diffraction efficiency, as large as 88% in the center of the aperture, and the DE falls off towards the edges, the minimum being 51.2% at the negative edge. This roll-off is a direct consequence of the zone-height averaging that was performed while discretizing the mirror. The overall diffraction efficiency of the mirror is 70.1%, which is fairly high, considering the large off-axis incidence angle and the resulting shadowing losses.

7.5 References

- [7.1] C.Alleyne, "Determination of off-axis diffraction efficiency for Fresnel microlenses using rigorous coupled wave analysis." M. Eng. Thesis, McGill University, 2003.
- [7.2] H. P. Herzig, *Micro-optics: Elements, systems and applications* Taylor & Francis, 1997.
- [7.3] J. M. Bendickson, E. N. Glytsis, and T. K. Gaylord, "Metallic surface-relief on-axis and off-axis focusing diffractive cylindrical mirrors," *Journal of the Optical*

- Society of America A-Optics Image Science and Vision, vol. 16, no. 1, pp. 113-130, Jan.1999.
- [7.4] E. Noponen, J. Turunen, and A. Vasara, "Electromagnetic Theory and Design of Diffractive-Lens Arrays," *Journal of the Optical Society of America A-Optics Image Science and Vision*, vol. 10, no. 3, pp. 434-443, Mar.1993.
- [7.5] Y. L. Sheng, D. Z. Feng, and S. Larochelle, "Analysis and synthesis of circular diffractive lens with local linear grating model and rigorous coupled-wave theory," *Journal of the Optical Society of America A-Optics Image Science and Vision*, vol. 14, no. 7, pp. 1562-1568, July1997.
- [7.6] G.J.Swanson, "Binary Optics Technology: Theoretical limits on the diffraction efficiency of multilevel diffractive optical elements," *MIT Technical Report 914*, 1991.
- [7.7] H. A. Kalhor and M. K. Moaveni, "Analysis of Diffraction Gratings by Finite-Difference Coupling Technique," *Journal of the Optical Society of America*, vol. 63, no. 12, pp. 1584-1588, 1973.
- [7.8] J.M.Jarem and P.P.Banerjee, Computational methods for electromagnetic and optical systems New York: Marcel Dekker, 2000.
- [7.9] K. S. Kunz and R. J. Luebbers, *The finite difference time domain method for electromagnetics* CRC Press, 1993.
- [7.10] Lumerical Solutions website: www.lumerical.com, 2006.

Chapter 8: Fabrication

This chapter focuses on the fabrication of the SPR sensor, which was carried out entirely in the McGill Micro-fabrication Lab. Fabrication was broken down into two parts, namely, the fabrication of the diffractive mirror, and the coupling slab. The mask designs and complete fabrication process-flows for both are presented.

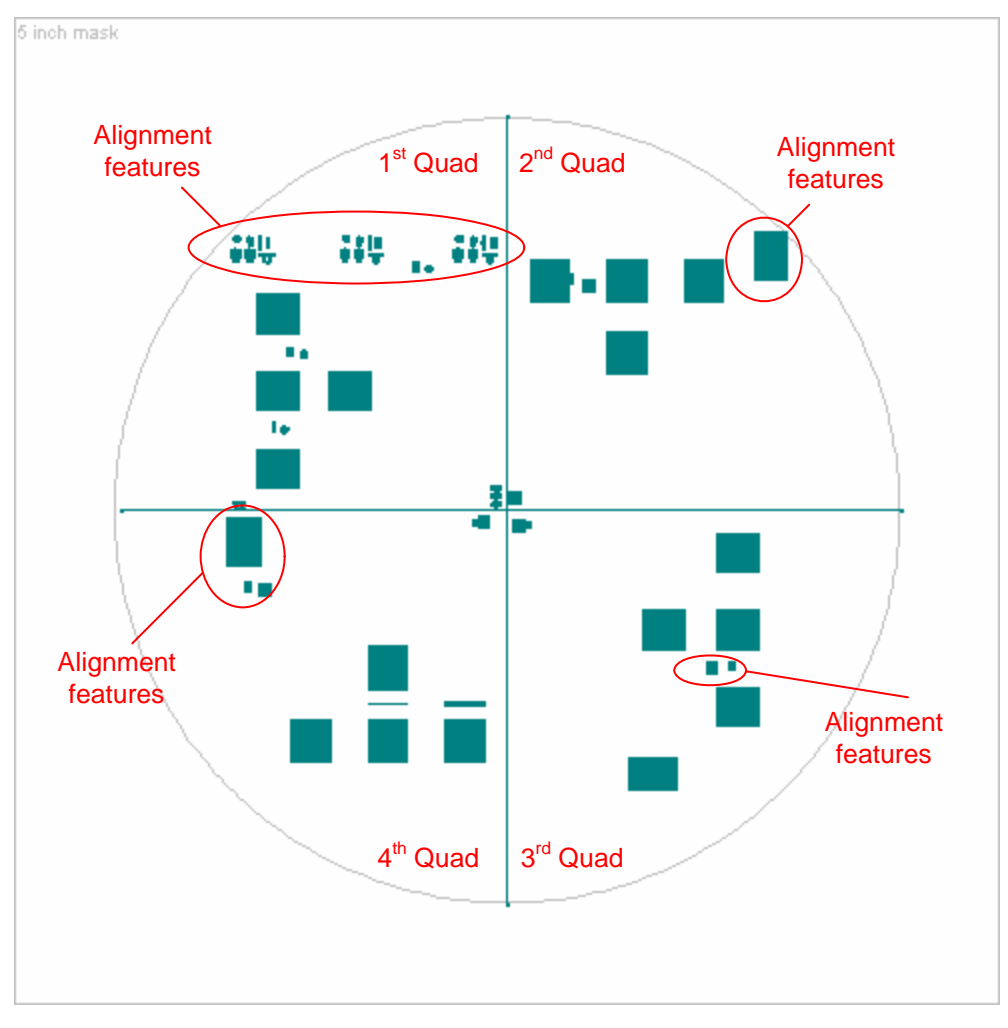
8.1 Diffractive mirror fabrication

The diffractive mirror and sensing surface are fabricated on a 1mm thick, rectangular (70mm x 50mm) fused silica substrate. The diffractive mirror profile is fabricated using multiple photolithographic exposure and pattern transfer steps. A binary coding scheme is used to quantize the phase profile in order to reduce number of pattern transfer steps required. N=2^M phase levels can be fabricated with M number of masks. Thus, 3 masks levels and 2 alignment steps are required to fabricate a structure with 8 phase levels: the first mask creates a binary profile, whereas the subsequent masks double the phase levels. Typically, the mask with smallest features is replicated first and each subsequent mask has features that are twice the width of the previous mask and requires etching to twice the depth [8.1].

Reactive Ion Etching (RIE) is generally performed to achieve directional etching with good aspect ratios. In our case, CHF₃ chemistry is used for RIE, which incidentally has poor selectivity with fused silica and photoresist. Thus, a hard mask must be formed to achieve high aspect ratios. Once the 8-level diffractive profile is created, aluminum is deposited on it using lift-off to make it reflective. Aluminum is generally more difficult to deposit with lift-off than some of the other available metals like chrome or gold, but has superior reflectance properties.

8.1.1 Mask Design

The photomask was designed using AutoCAD. The mask is basically split into four quadrants as shown in Fig. 8.1, and the features in each quadrant are rotated 90° clockwise with respect to the features in the previous quadrant. This is done to avoid fabricating individual photo-masks for each set of features. The three mask levels required for fabricating the 8-level profile are placed in the first three quadrants, in the order of increasing feature sizes. The first quadrant consists of the mask with the smallest features and is used to create a binary profile. As such, it will be referred to as "1-bit Mask" throughout this document. Similarly, the second binary mask located in the second quadrant creates a 4-level profile and will be referred to as "2-bit Mask". The "3-bit Mask" is located in the third quadrant and has the largest features. The feature sizes of all these masks were obtained using the analytical model developed in Chapter 4. The fourth quadrant consists of a simple mask pattern that is used to deposit aluminum on the 8-level diffractive profile to make it reflective and will be referred to as "AL Mask". A number of alignment features were also added in the corners and middle part of each quadrant, with alignment verniers having resolutions varying from 0.2 µm to 1 µm, as shown in Fig. 8.2. The photo-mask was fabricated on a 5"x5" quartz substrate by Benchmark Technologies Inc. with a feature resolution of ± 100 nm. All the drawn features in Figure 8.1 and 8.2 appear as transparent on the actual mask, while the rest of the area is Chrome.



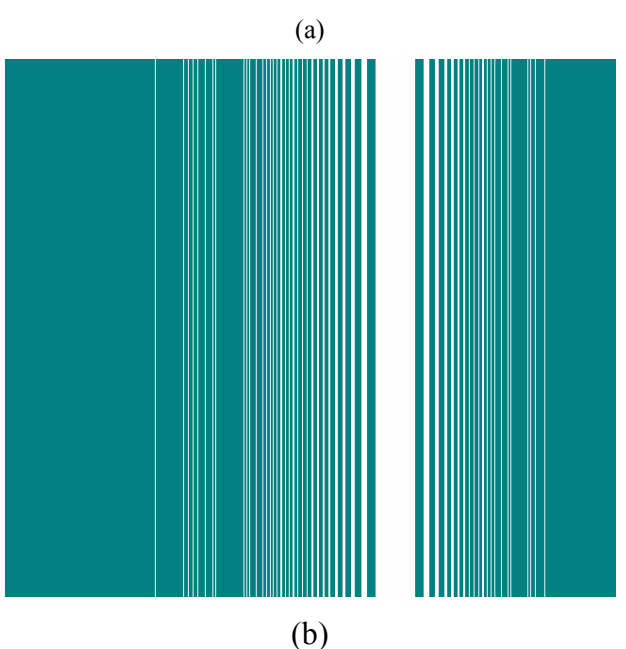


Fig. 8.1: (a) Photmask layout, (b) Zoomed in image of a grating in the 1st quadrant

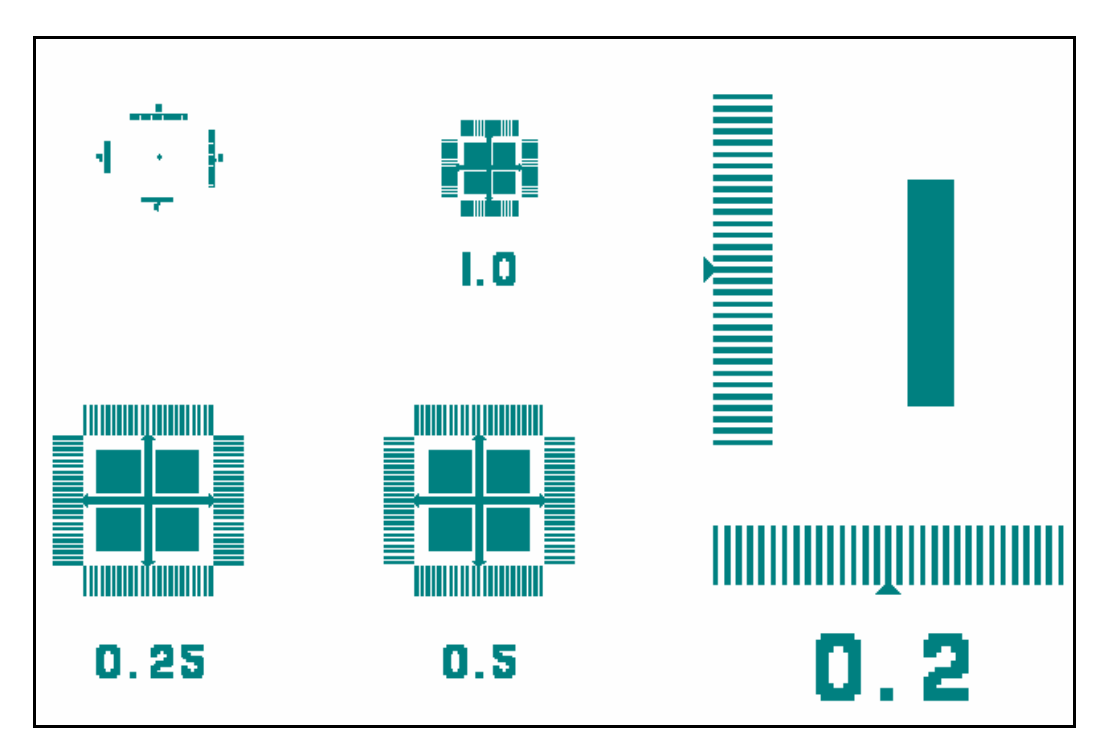
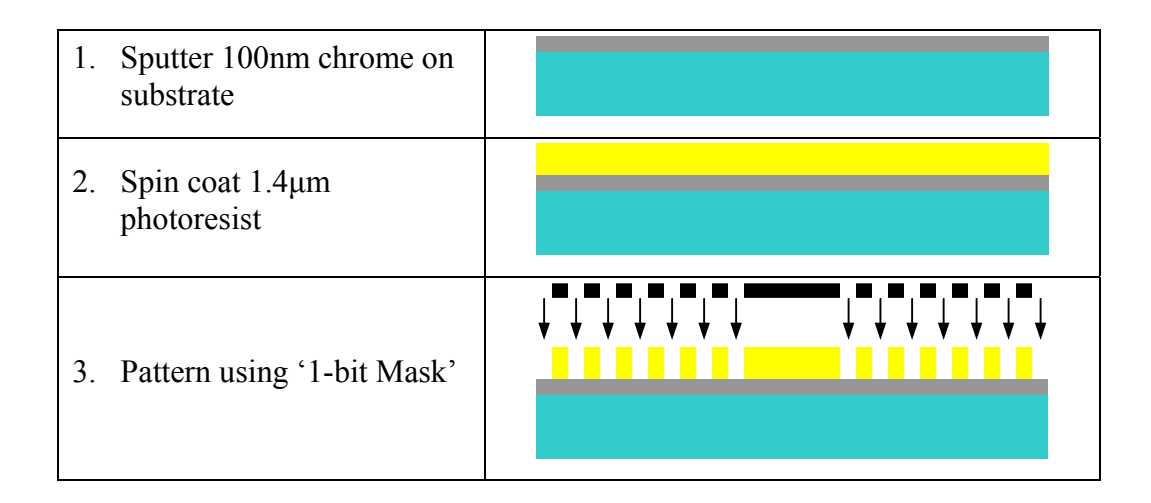


Fig. 8.2: Variety of alignment features with vernier resolutions varying from 0.2μm to 1μm.

8.1.2 Process-flow

Fig. 8.3 provides a summary of the process flow. The detailed steps are listed thereafter.



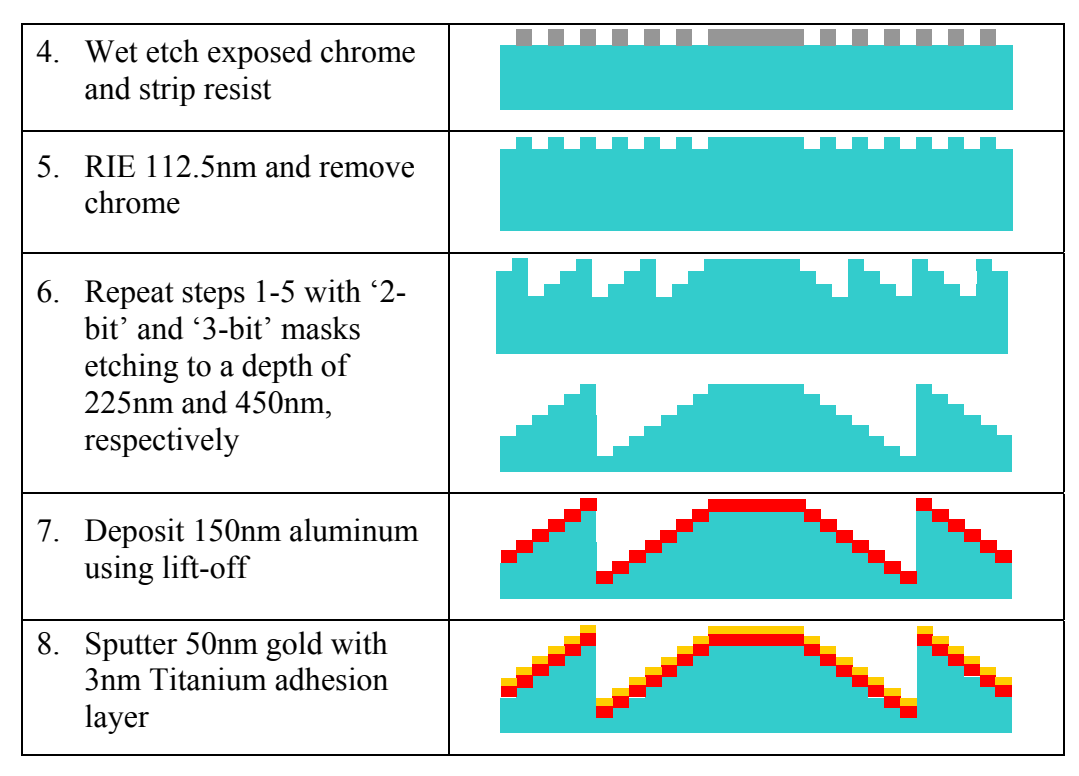


Fig. 8.3: Summary of diffractive mirror fabrication process-flow

Step 1: Clean sample

Perform solvent cleaning procedure:

- Set ultrasonic bath temperature to 40°C and power to 100%.
- Soak wafer in acetone in a glass dish.
- Place dish in ultrasonic bath for 10 minutes.
- Repeat with iso-propanol (IPA) for 10 minutes.
- Rinse sample in de-ionized (DI) water.
- Blow dry with nitrogen gas.

Step 2: Sputter 100nm Chrome

Sputter 100nm Chrome using the MRC Sputter tool.

 Place sample on designated wafer holder. Button tape should be used at the corners of the sample to hold it in place. - Run a recipe with the following parameters:

o Power: 1 kW

o Pressure: 5 mTorr

o Speed: 19.5 cm/min

o Hi Vac: $6x10^{-7}$ Torr

o Gas: Sput 1 (Chrome Target)

Scan number: 1

Step 3: Clean sample

Repeat Step 1.

Step 4: Spin-on photoresist

Since the sample is rectangular in shape, the semi-automatic BidTec R&D spinner should be used to spin photoresist.

- Place Teflon chuck on spinner.
- Place an o-ring on chuck. O-ring must have at least 1.5" diameter.
- Place substrate on o-ring and center as much as possible.
- Using a disposable pipette, dispense enough Shipley 1813 photoresist to cover the entire substrate. Make sure no air bubbles are present in the resist.
- Select Recipe #0 on the tool. Spin sample at 500rpm for 5 seconds, followed by spin speed of 3950rpm for 30 seconds.
- Using a swab dipped in acetone, carefully remove the photoresist edge-bead from around the edges of the sample.
- Soft bake sample in convection oven at 90°C for 10 minutes.

Step 5: "1-bit Mask" Exposure

The EVG Aligner tool is used for this step. This first exposure step does not require any alignment, but the placement of the substrate with respect to the mask is tricky. The

substrate must be placed such that the gratings are 20mm from the left edge, as discussed in Chapter 4. This can be achieved with reasonable accuracy by using a transparency of the mask pattern.

- Use the "Top-side 5-inch mask custom" recipe on the EVG Aligner.
- Modify the recipe by changing the 'Separation' distance to 500μm. Select constant energy exposure with 50mJ. Select the 'Hard Contact' mode.
- Use the 6" wafer chuck. Since the sample is much smaller than a 6" wafer, the vacuum suction is reduced, unfortunately.
- Poke holes in the transparency so that vacuum suction can be transferred to the sample once it is placed on top.
- Place the transparency on the chuck and align with the mask. Do NOT continue with exposing the transparency. Move transparency back out from underneath the mask.
- Using a ruler or vernier caliper, place the substrate on top of the transparency such that grating pattern on the transparency is 20mm from the edge of the sample.
- Expose sample and store in photoroom until developed.

Step 6: Develop sample

- Immerse sample in a beaker with MF-319 solvent and agitate slowly for 45 seconds.
- Thoroughly rinse in DI water and blow dry with nitrogen.

Step 7: Hard bake sample

- Bake sample in convection oven for 25 minutes at 90°C.
- Allow sample to cool to room temperature.

Step 8: Wet etch Chrome

- Immerse sample in a beaker with chromium etchant (Cyantek CR-14S or CR-7S) for around 90 seconds or more, until the exposed areas become transparent.
- Thoroughly rinse in DI water and blow dry with nitrogen.

Step 9: Strip photoresist

The photoresist is stripped to reveal the chrome hard mask. Since the photoresist has been

hard baked, it is difficult to remove. Complete removal of the resist is absolutely

essential, as such, resist stripping is performed in two steps:

Solvent clean sample as in Step 1.

Immerse sample in Piranha solution (H₂SO₄:H₂O₂ in 3:1 ratio) for 10 minutes.

Thoroughly rinse in DI water and blow dry with nitrogen.

Step 10: RIE 112.5nm fused silica

RIE is performed using CHF₃ and Argon chemistry using the Applied Materials P5000

tool. Target etch depth is 112.5nm. The preprogrammed 'Nanotools Fused Silica Etch'

recipe is used. The etch rate is around 90nm/min. However, the etching time should be

split into several intervals and the etch depth should be measured in between intervals to

get a better estimation of the etch rate.

- Place sample on a clean 6" silicon dummy wafer. The wafer can be cleaned using a

Solvent Clean if necessary. A thermal conductive paste is applied in a very small

quantity at the corners of the sample to provide adhesion with the wafer. Excessive

paste can cause overheating of sample and result in poor etching results.

- Perform RIE for around 75 seconds using the following etch recipe:

o Step 1: Stabilization

Time: 15 seconds

Pressure: 50 mTorr

RF Power: 0.0 W

Magnetic Field: 0.0 Gauss

Mixture: CHF₃: 30 sccm, Ar: 70 sccm

o Step 2: Etch

Time: ~75 seconds

Pressure: 50 mTorr

RF Power: 250 W

65

Magnetic Field: 70.0 Gauss

■ Mixture: CHF₃: 30 sccm, Ar: 70 sccm

o Step 3: Residue Evac

■ Time: 10 seconds

Pressure: Throttle open

RF Power: 50 W

Magnetic Field: 0.0 Gauss

Mixture: Ar: 70 sccm

- Immerse sample and dummy wafer in warm acetone at 40°C in an ultrasonic bath for a few minutes to dissolve the thermal conductive paste.
- Solvent clean both the sample and dummy wafer separately.

Step 11: Wet etch chrome hard mask

- Place sample in chromium etchant (Cyantek CR-14S or CR-7S) for 2 hours or more until all the chrome is completely etched.
- Thoroughly rinse in DI water and blow dry with nitrogen.

Steps 12 – 15: Clean sample, sputter 100nm chrome and spin-on photoresist

Repeat Steps 1 – 4.

Step 16: Clean mask

The photomask is cleaned before every exposure step in order to facilitate and improve alignment:

- Solvent clean mask as in Step 1.
- For stronger cleaning a 'mild' Piranha solution can be used (H₂SO₄:H₂O₂ in 5:1 ratio) for 10 minutes.
- Spin-dry mask in a Laurell Spin Dryer with the appropriate mask chuck.

Step 17: "2-bit Mask" Exposure

Just as in Step 5, the alignment and exposure are performed again on the EVG aligner, but with the "2-bit Mask'. The transparency can be used again to aid the placement of the sample underneath the mask. Once the sample and mask are aligned, the former can be exposed using the same recipe as Step 5.

Steps 18 – 21: Develop sample, hard bake, etch chrome and strip resist

Repeat Steps 6 – 9.

Step 22: RIE 225nm fused silica

Repeat Step 10 with etch time of around 150 seconds to create a 2-bit profile.

Step 23: Wet etch chrome hard mask

Repeat Step 11

Steps 24 – 35: Pattern and etch cycle for creating 8-level profile

Repeat Steps 12 – 23 with "3-bit Mask" and RIE etch time of around 300 seconds to achieve an etch depth of 450nm.

Step 36: Clean Sample

Repeat Step 1.

Step 37: Spin-on Photoresist

Repeat Step 4, only edge-bead removal is not performed, since we do not want aluminum

to be deposited all around the edges.

Steps 38 – 39: "AL Mask" exposure and develop

Repeat Step 17 but with the "AL Mask" to expose sample. Repeat Step 6 to develop

sample. Sample is not hard baked thereafter, in order to facilitate lift-off.

Step 40: Sputter 150nm Aluminum

Sputter 150nm aluminum using the MRC Sputter tool.

- Place sample on designated wafer holder. Button tape should be used at the corners of

the sample to hold it in place.

- Run a recipe with the following parameters:

o Power: 3.16 kW

o Pressure: 10 mTorr

o Speed: 31.8 cm/min

 \circ Hi Vac: $6x10^{-7}$ Torr

o Gas: Sput 3 (Aluminum target)

o Scan number: 1

Step 41: Perform Lift-off

Aluminum can be difficult to lift-off and as such the following process should be

repeated multiple times if necessary:

- Soak sample in Acetone followed by IPA for 20 minutes each in an ultrasonic bath at

40°C.

Rinse thoroughly with DI water.

68

Blow dry with nitrogen gas.

- Repeat acetone and IPA treatment in a new set of glass dishes if aluminum residue is

still present in unwanted regions.

Step 42: Sputter 3nm Titanium and 50 nm Gold

The Denton RF/DC Sputter tool is used to sputter a 3nm Titanium adhesion layer

followed by a 50nm gold layer for SPR sensing, in situ, using the following recipe

parameters:

- Min. vacuum setpoint: 1.0E-05 Torr

Argon Gas setpoint: 25sccm for Ti and 50sccm for Au

Gas pressure: 5 mTorr

DC source current: 0.5A for Ti and 0.2A for Au

Sputter time: 20 seconds for Ti and 600 seconds for Au

Step 43: Clean Sample

Repeat Step 1.

8.2 Coupling slab fabrication

As discussed in Chapter 4, we need to create a cavity in the rectangular (70mm x 50mm)

coupling slab in order to create an air gap once the substrate is glued on top. The cavity

has a depth of 2µm and a length of 11.38mm. The position of the cavity is critical in

order to couple all the light through. The slab itself is quite bulky with a thickness of

30mm, as such, is difficult to work with in the microfab where most of the tools are

designed for operation with much thinner substrates. Ideally, we would like to achieve

vertical cavity sidewalls using reactive ion etching; however, the size of the slab makes it

incompatible for use with the Applied Materials P5000 RIE tool. Thus, isotropic wet

etching was performed using buffered oxide etch solution (6:1 40% NH₄F: 49% HF).

69

8.2.1 Mask Design

The simple mask pattern was laid out in AutoCAD, as shown in Fig. 8.4. The chrome photomask was fabricated on a 5"x5" quartz substrate.

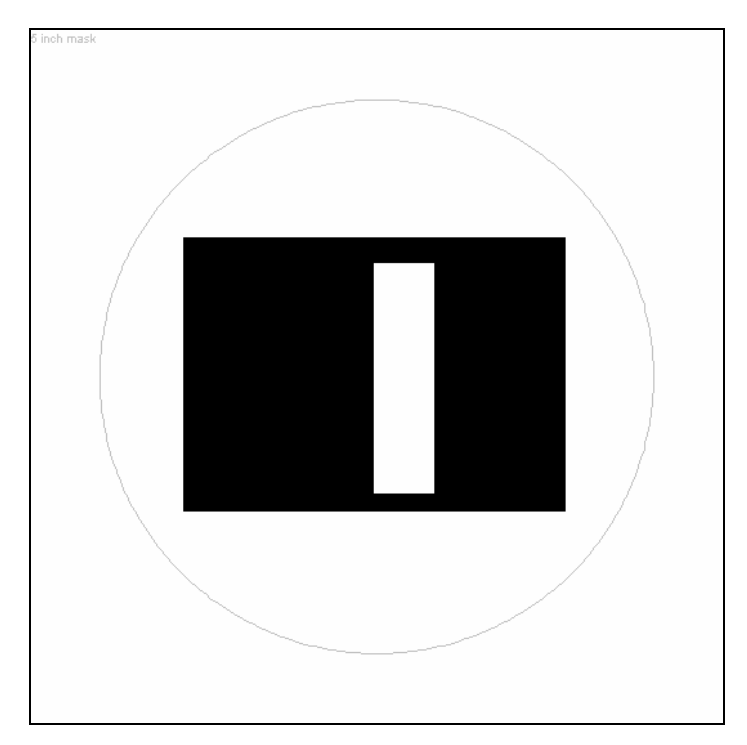
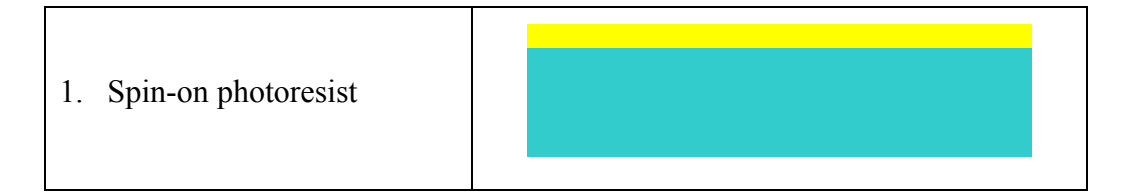


Fig. 8.4: Mask layout for coupling slab

8.2.2 Process-flow

Fig. 8.5 provides a summary of the process flow. The detailed steps are listed thereafter.



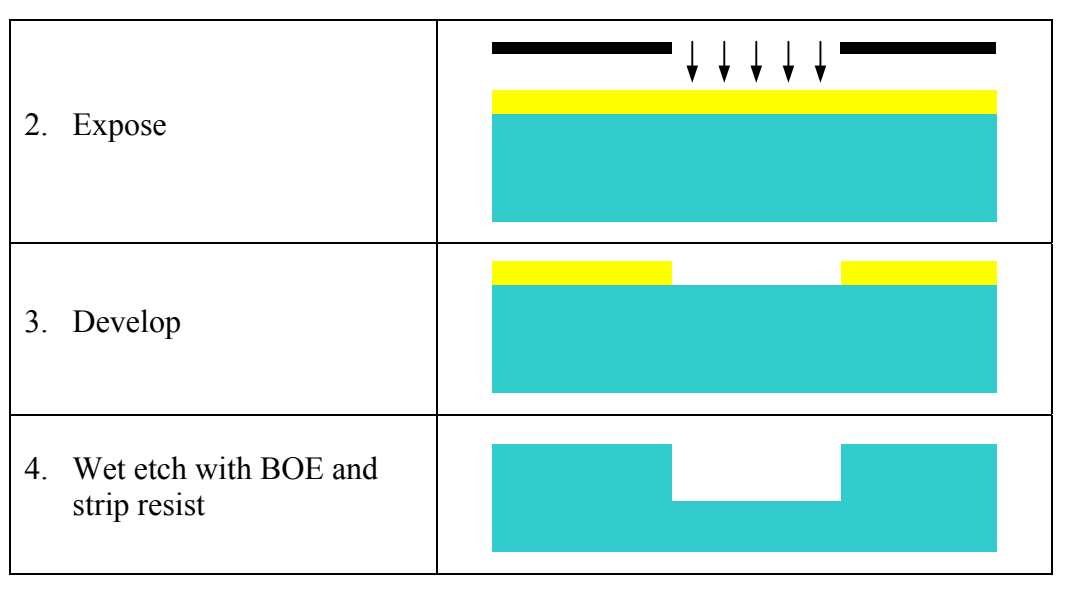


Fig. 8.5: Summary of coupling slab fabrication process-flow

Step 1: Clean sample

Perform solvent cleaning procedure:

- Set ultrasonic bath temperature to 40°C and power to 100%.
- Soak sample in acetone in a glass dish.
- Place dish in ultrasonic bath for 10 minutes.
- Repeat with iso-propanol (IPA) for 10 minutes.
- Rinse sample in de-ionized (DI) water.
- Blow dry with nitrogen gas.

Step 2: Spin-on photoresist

The semi-automatic BidTec R&D spinner should be used to spin photoresist.

- Place Teflon chuck on spinner.
- Place an o-ring on chuck. O-ring must have at least 1.5" diameter.
- Place sample on o-ring and center as much as possible.
- Using a disposable pipette, dispense enough Shipley 1818 photoresist to cover the entire top surface of the sample. Make sure no air bubbles are present in the resist.

- Select Recipe #1 on the tool. Spin sample at 500rpm for 5 seconds, followed by spin speed of 1000rpm for 30 seconds. Resist thickness is around 4.2μm.
- Soft bake sample in convection oven at 90°C for 10 minutes.

Step 3: Mask Exposure

The EVG Aligner tool is used for this step.

- Use the "Flood exposure" recipe on the EVG Aligner.
- Place sample on the 6" wafer chuck.
- Place mask on top of sample. Align manually with care, making sure the mask pattern covers the entire coupling slab surface completely.
- Expose sample for 13 seconds and store in photoroom until developed.

Step 4: Develop sample

- Dispense sufficient MF-319 solvent on top of sample and agitate slowly for 2 minutes.
- Thoroughly rinse in DI water and blow dry with nitrogen.

Step 5: Hard bake sample

- Bake sample in convection oven for 25 minutes at 90°C.
- Allow sample to cool to room temperature.

Step 6: Wet etch fused silica

Buffered oxide etch (BOE) solution is used for wet etching.

- Place sample in a plastic beaker.
- Using a plastic disposable pipette, dispense BOE solution on the exposed fused silica area only. The photoresist cavity serves to nicely confine the BOE solution in the exposed area.
- Etch for 30 minutes at room temperature. Etch rate is ~68nm/min.

Rinse sample thoroughly in DI water and blow dry with nitrogen gas.

Step 7: Strip photoresist and clean sample

- Solvent clean sample as in Step 1.

8.3 Fabrication results

Three complete devices were fabricated with consistent results. Fabrication is evaluated with scanning electron microscopy (SEM), optical microscopy and stylus profilometry. Fig. 8.6 shows a microscope image of the top view of one of the 8-level diffractive mirrors. Alignment can be extremely critical towards device performance. After two alignment steps the smallest lateral misalignment achieved was $0.3\mu m$, which can be seen in the SEM image of the positive edge (smallest zone) of the mirror in Fig. 8.7. The misalignment estimated using the alignment verniers on the mask/substrate was $0.2 \mu m$, which is very close to the SEM results. The small discrepancy can be attributed to insufficient resolution of the optical microscope to decipher such small misalignments.

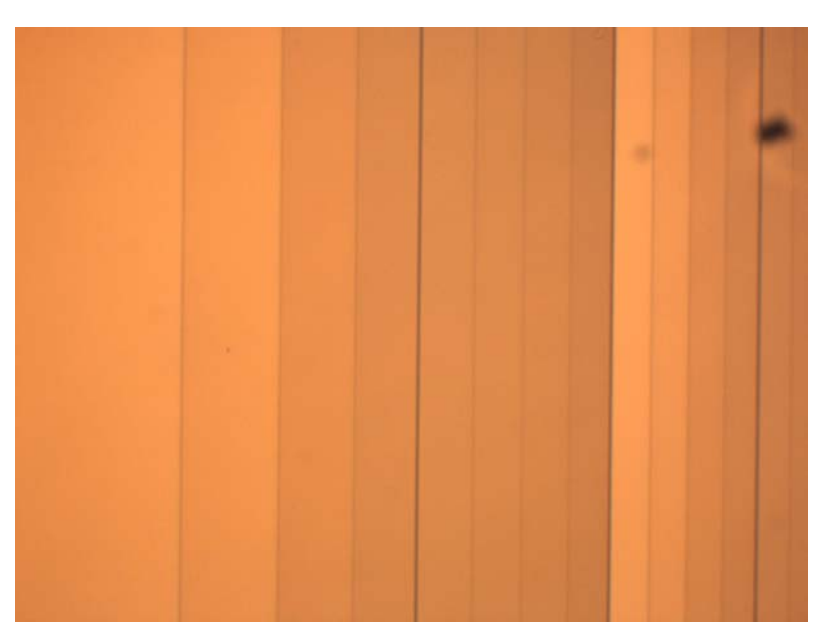


Fig. 8.6: Top-view of the first zone obtained with an optical microscope

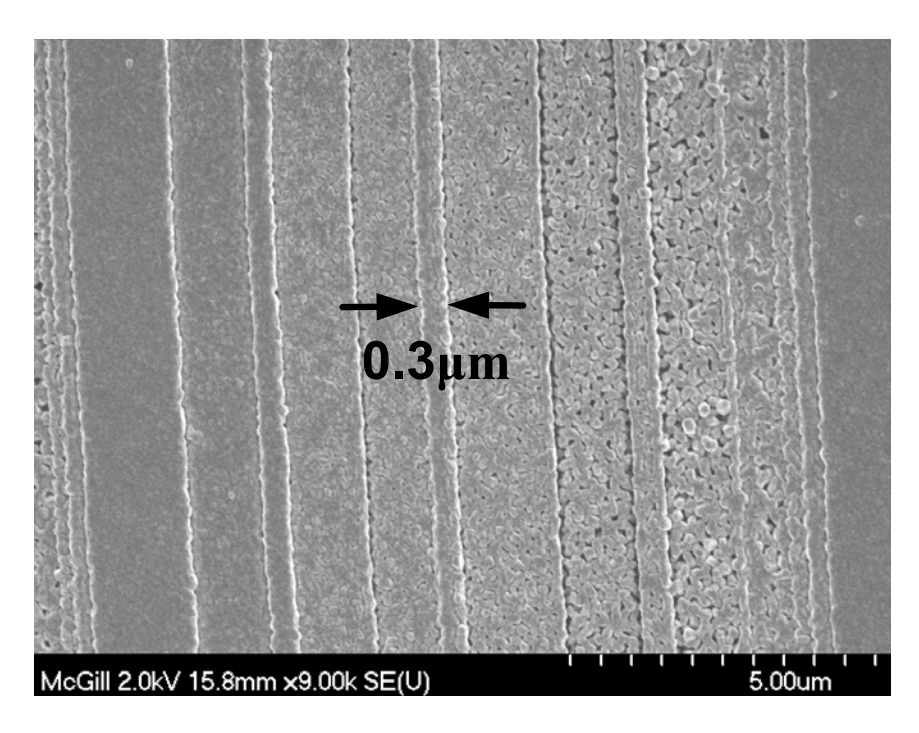


Fig. 8.7: SEM Image of the smallest zone, showing 0.3μm of misalignment

Cross-sectional view of the first zone, obtained with a stylus profilometer is shown in Fig. 8.8. The phase steps are fairly uniform; however, there are some non-uniformities in the phase steps caused by reactive ion etching errors. RIE is a very dynamic process, and the etch rate can be tricky to predict exactly. Moreover, the gas mixture also slowly attacks chrome (etch rate $\sim 1-2$ nm/min), making the fused silica etch depth even harder to predict. Lastly, the misalignment peaks shown in Fig. 8.8 are exaggerated owing to the low resolution of the stylus profilometer.

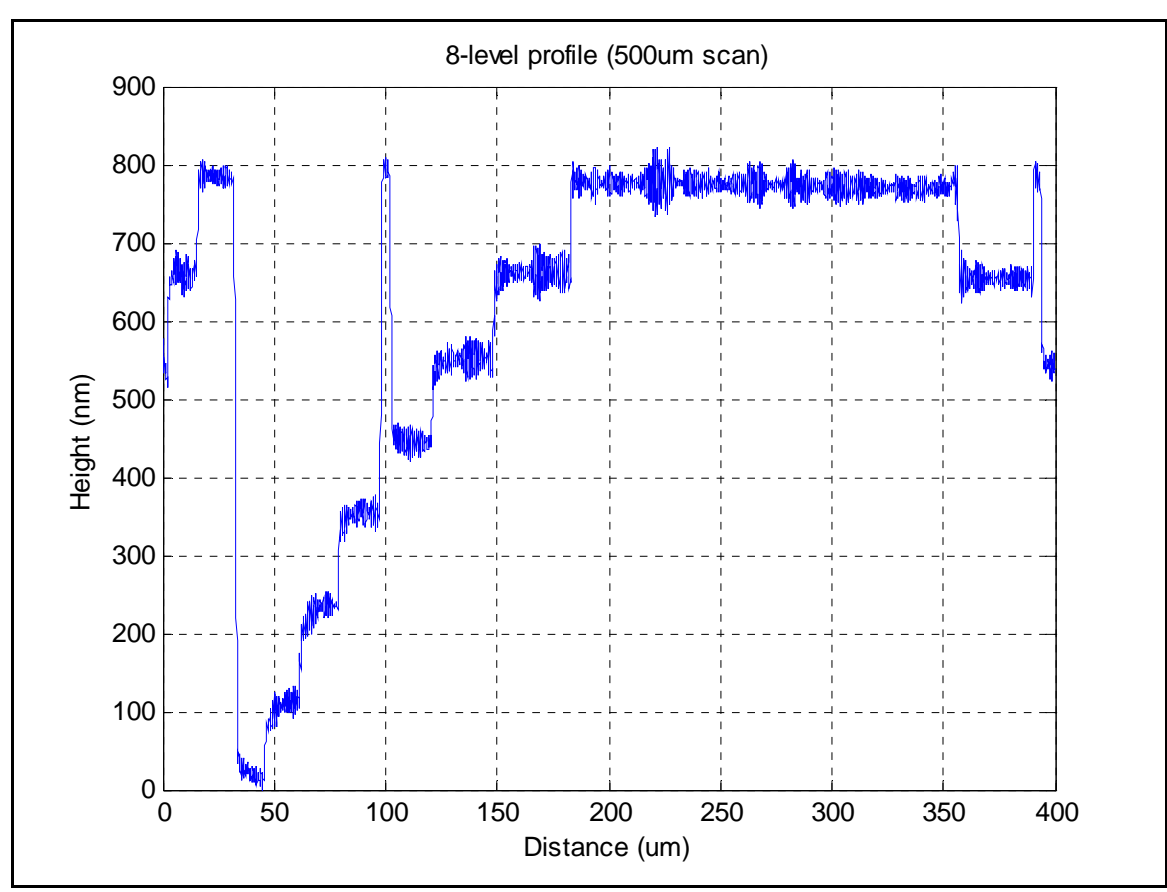


Fig. 8.8: Cross-sectional view of the first zone obtained with a stylus profilometer, showing 8 phase-steps. Average step height is 114.3nm.

Fig. 8.9 shows an optical microscope image of the cavity etched in the fused silica coupling slab. There is some over-etching at the corners, which is typical with wet etching. The width of the cavity boundaries is less than a $50\mu m$, which is quite acceptable for the performance of the device, however.

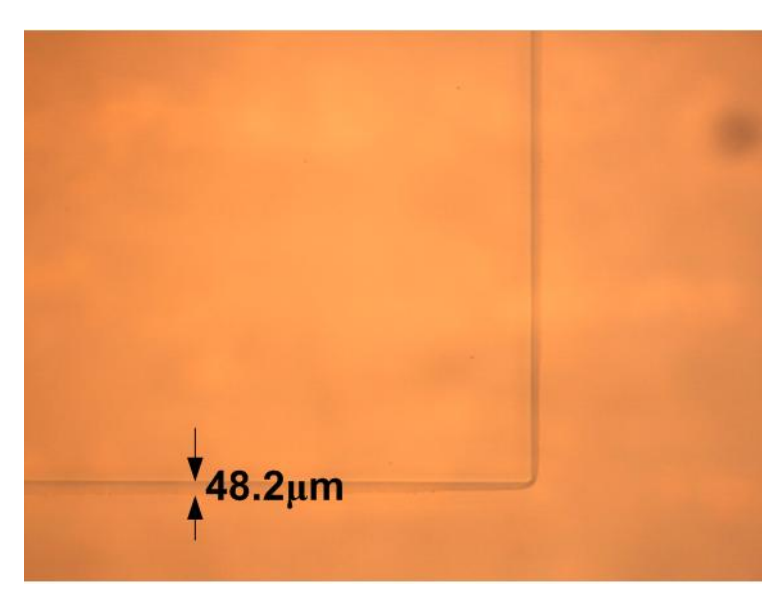


Fig. 8.9: Top-view of the coupling slab cavity obtained with an optical microscope showing edge boundaries smaller than 50μm

Fig. 8.10 shows the cross-sectional view of the cavity. The step height is a fraction over the targeted $2\mu m$ depth. RCWA simulations show that an air gap of $2\mu m$ would totally internally reflect 99.9% of light.

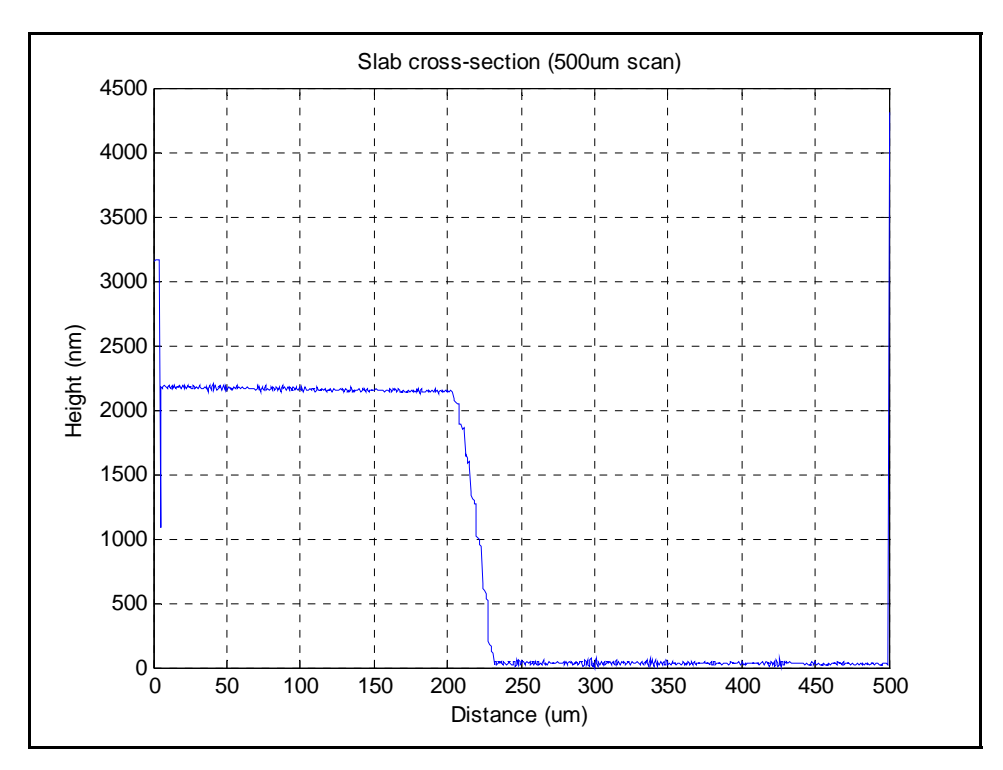


Fig. 8.10: Cross-section of an edge of the cavity in the coupling slab showing a step height of 2.1μm

The 1mm substrate and coupling slab were joined together using index matching fluid from Cargille Labs, which has a refractive index of 1.4554 at 589.3nm wavelength. The capillary forces hold the two components together quite strongly. Fig. 8.11 shows an image of a completed device.

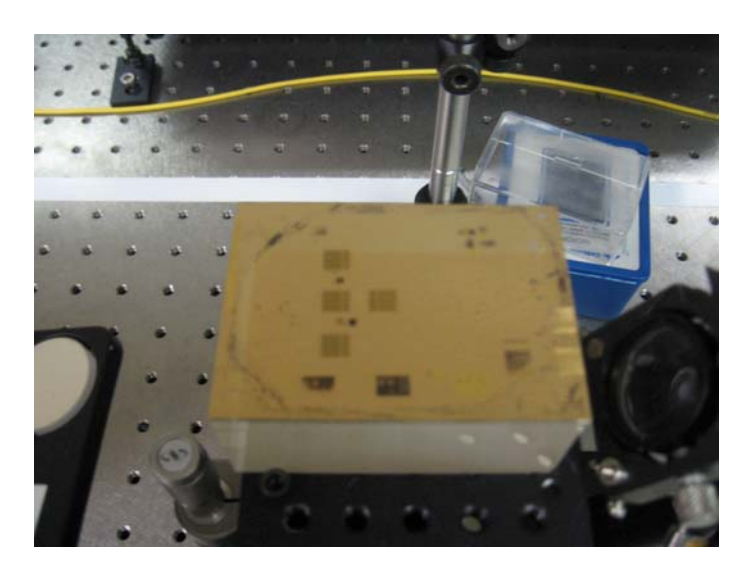


Fig. 8.11: Image of a completed SPR sensor

The index matching fluid is dispensed onto the coupling slab in a very small quantity using a syringe. It can be quite difficult to get the quantity and placement of the fluid exactly right in order to prevent it from flowing into the cavity. The trial and error nature of the procedure makes it quite impractical. A much simpler alternative would be to use two coupling slabs, one for the input and output each, as opposed to one big slab. The extra cost of the additional slab would be offset by the cost and time of etching the cavity in the single slab.

8.4 References

[8.1] M. B. Stern, "Pattern transfer for diffractive and refractive microoptics," *Microelectronic Engineering*, vol. 34, no. 3-4, pp. 299-319, Dec.1997.

Chapter 9: Testing and Results

This chapter is dedicated to testing of the SPR sensor. The final results and some future considerations are also discussed.

9.1 Test Setup

The test setup is shown in Fig. 9.1. The light source is an SDL 8360 diode laser that has an emission peak at wavelength of 852nm. The laser is fiber-coupled and is inserted in the setup via a coupler (OZ Optics [9.1]), which is used to collimate the light coming out of the fiber. A 2x beam expander, formed using two spherical lenses, spaced 60mm apart and having focal lengths of 20mm and 40mm, are used to obtain a collimated beam with the required diameter of 2mm. The input from the laser is very close to being TMpolarized, so a polarizer with the transmission axis set to vertical, is used to achieve TM polarization. Although SPR only occurs with TM polarized light, TE polarization data is often used for normalization purposes. Thus a combination of a half-wave plate, followed by another high-precision polarizer, is used to rotate the polarization between TM and TE. The extinction ratio of the setup was around 16dB. A neutral density filter is placed thereafter to attenuate the beam intensity. A silvered mirror is used to deflect the light at the desired angle (14.89°). The fabricated SPR sensor is placed on an XYZ stage, such that the incoming beam is horizontally aligned with one of the DOEs on the device. The output beam is captured using a Watec 502B monochrome CCD camera. The CCD has a sensing area of 5mm x 8mm, which is much too small to capture the entire output spectrum. Thus, some collimating optics are used at the output end as well to map the image at the output edge of the SPR device on to the CCD.

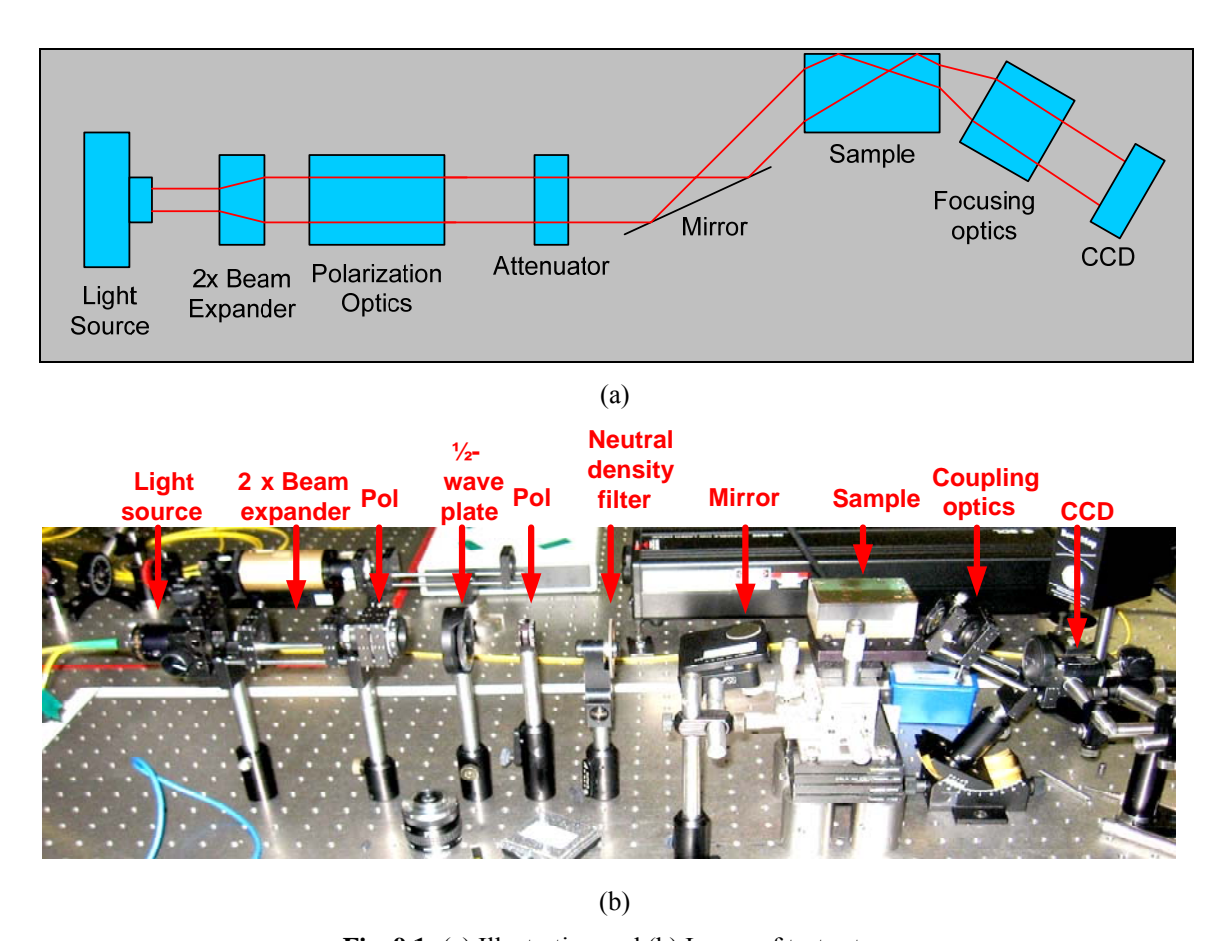


Fig. 9.1: (a) Illustration and (b) Image of test setup

Obtaining the correct input angle is very important for device operation. This is accomplished using a high-precision mirror tilt stage. To ascertain correctness of the mirror tilt, another technique is also employed: the beam is aimed at a plain region of the device so that it is simply reflected and no diffraction occurs. The vertical position of the beam spot on the input and output facets are measured using a vernier caliper and the beam angle inside the device is then computed using simple trigonometry. Once the angle is determined and fixed, the XYZ stage can be simply adjusted to ensure that the beam completely illuminates the DOE.

It must be pointed out that the set of diffractive mirrors fabricated in the middle of the sensor, which were supposed to form a device with both focusing and collimating DOEs, could not be used due to a mask design error. The distance between the two DOEs was

incorrect on the mask, thus rendering them useless, unfortunately. Therefore, testing results for double DOE device will not be presented.

The characterization and collimation of the laser, and output coupling optics design are discussed in detail in the following sections.

9.1.1 Laser characterization

The output spectrum of the SDL Laser was interrogated using an optical spectrum analyzer for various input powers. Fig. 9.2 shows that the lasing peak is located at 852nm. The noise attributes of the laser are quite poor; the noise floor is significantly high between the 840nm – 860nm range, which will inevitably translate to poor noise characteristics of the sensor. At low input driving power of 100mW, the Signal-to-Noise Ratio (SNR) is only around 9.5dB. The laser has to be pumped at a much higher input power of 350mW to achieve a better SNR of around 29dB. At this input, the output power out of the fiber, after coupling losses, is around 9mW which is quite excessive for the operation of the SPR device. Thus, most of the power has to be attenuated, in order to avoid saturating the CCD during SPR experiments, which is very wasteful. Even at high pump powers, the laser suffers from mode-hopping which translates to poor noise characteristics.

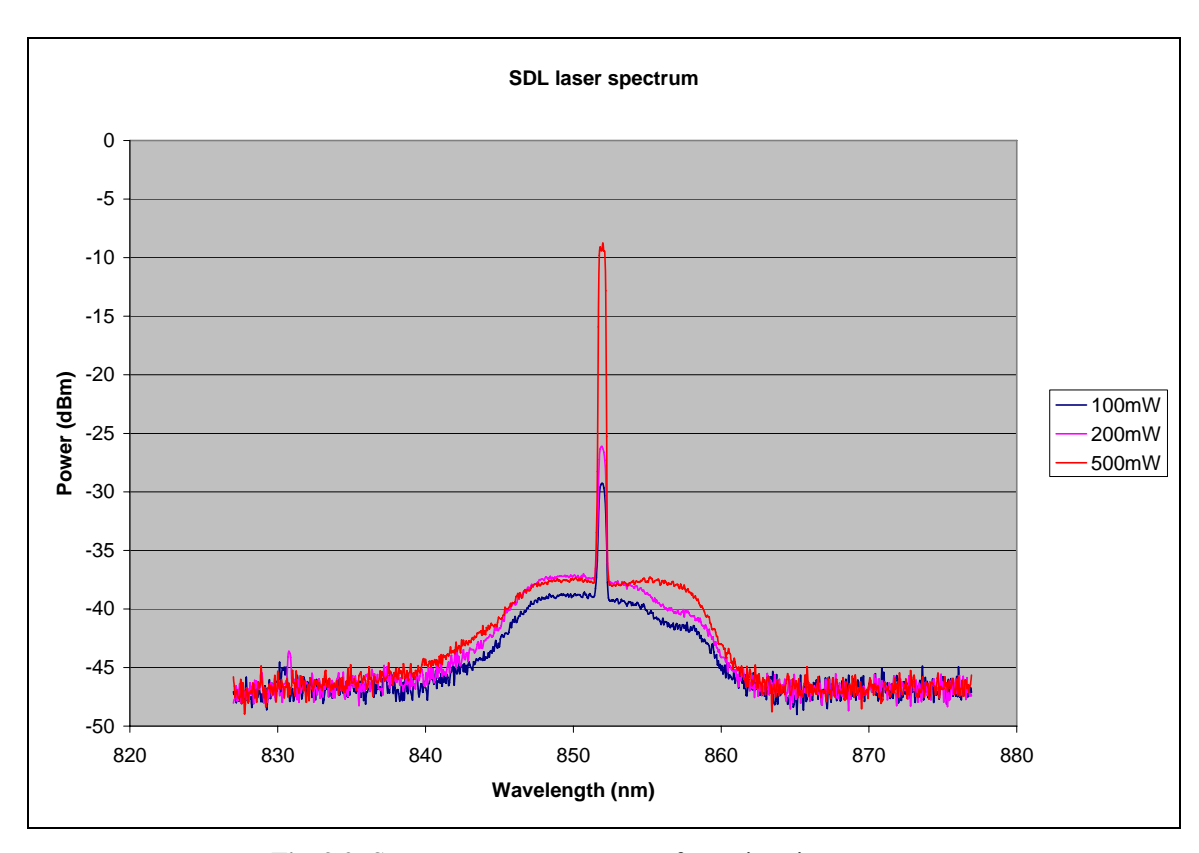


Fig. 9.2: SDL Laser output spectrum for various input powers

9.1.2 Beam Profile

The beam was profiled using a DataRay Beam Profiler. The profiler can simultaneously capture five images of the beam as it impinges on 5 planes situated $50\mu m$ apart from each other on the scan head. Fig. 9.3 shows the profile of the laser output from the OZ-coupler/collimator with an input power of 200mW. The beam has a fairly Gaussian profile and a spot size of around $909\mu m$.

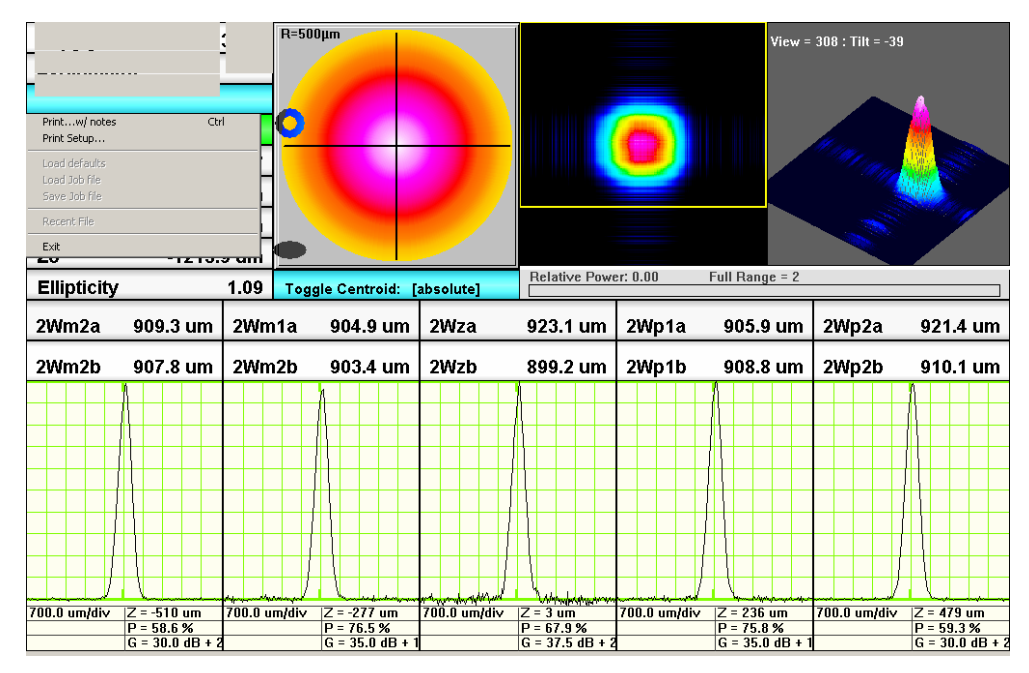


Fig 9.3: Laser output before beam expander: Input power = 200mW, Image distance = 200mm, Spot size ~ 909 μ m

The output after passing through the 2x beam expander is shown in Fig. 9.4. The spot size is around 1.98mm, but the profile is not as perfectly Gaussian as before. Some form of spatial filtering could be used to improve the profile, however, no such method was employed in this case. The beam collimation is checked by taking measurements at various image distances. For image distances varying from 100mm to 200mm, the total increase in spot size is around 0.05mm, which suggests that the beam is fairly well collimated.

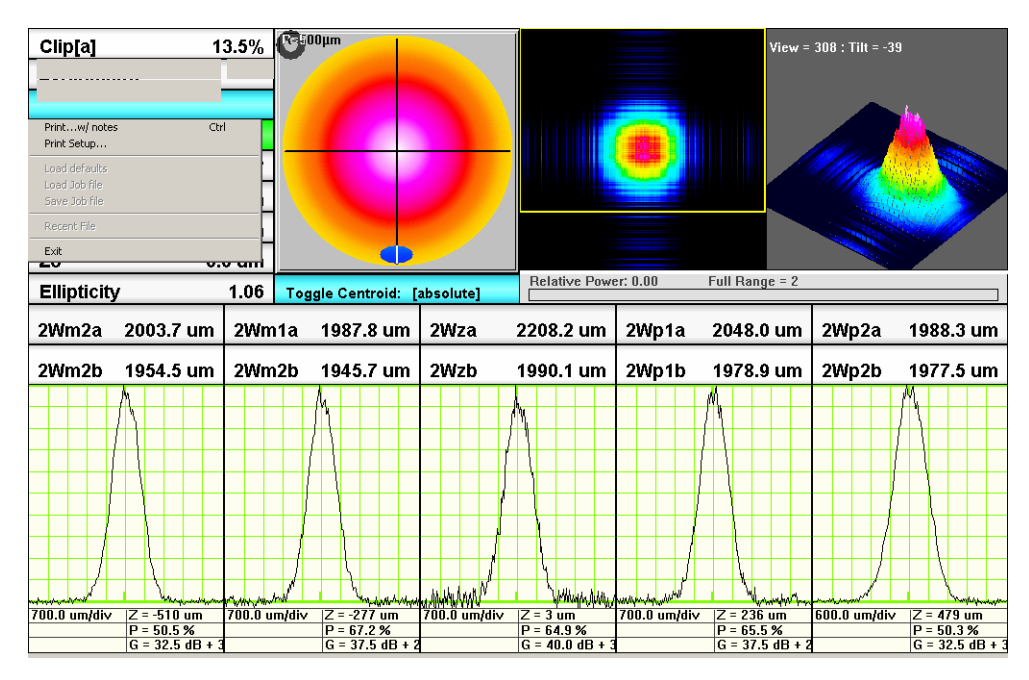


Fig. 9.4: Laser output after 2x beam expander: Input power = 200mW, Image distance = 200mm, Spot size ~ 2.00 mm.

9.1.3 Design of output focusing optics

As detailed in the analytical design of Chapter 4, the output beam after traversing through the system is a diverging beam with an angular spectrum ranging from 63° to 78° and has a beam diameter of 12.05mm at the output edge of the sensor (Fig. 9.5). The CCD camera employed has a sensing area of only 5mm x 8mm, which is clearly insufficient to capture the entire image. Thus a simple optical system was devised to map the image at the output edge of sensor onto the CCD.

Code V was used to model the focusing optics at the output, as shown in Fig. 9.6. The chief ray of the output beam makes an angle of 29.79° with the horizontal, after refraction at the fused silica/air interface. Thus, the optical axis is bent at this angle, and two lenses with focal lengths of 50mm and 80mm are placed in turn to collimate and then focus the beam, respectively. The first lens is placed 20mm from the edge of the sensor, whereas the distance of the second lens can be adjusted to alter the image size. The CCD sensing

area has a length of 8mm, so in the optimum case, a lens separation of 20.5mm results in an image that illuminates the CCD completely.

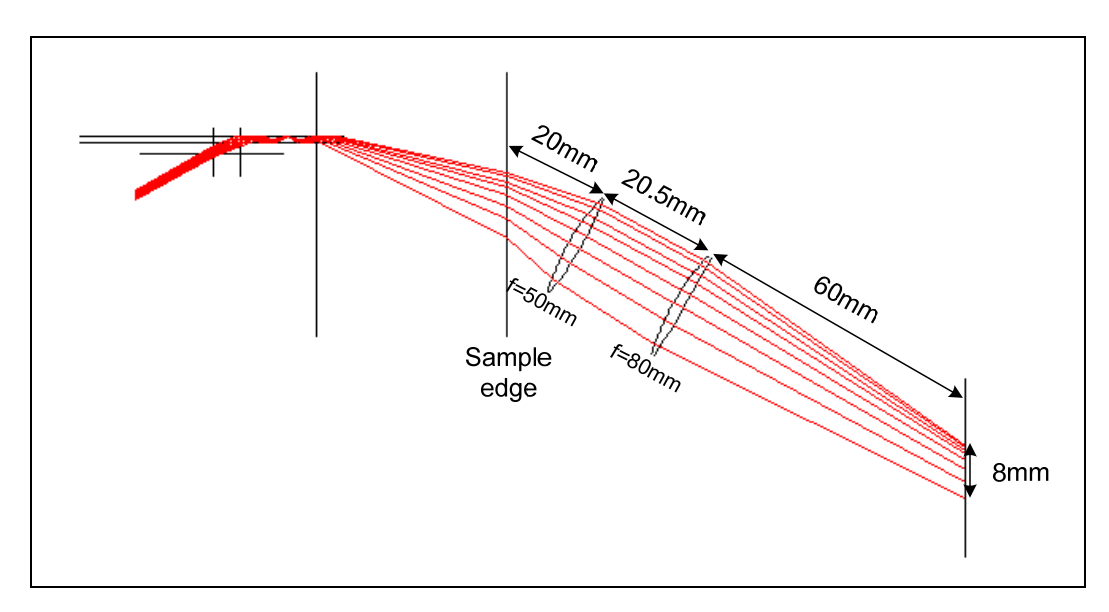


Fig. 9.6: Extended Code V model with output focusing optics

9.1.4 Flow cell

The flow cell used to deliver analyte solutions to the SPR sensing surface is a simple Teflon chamber with a 12.7mm diameter. The chamber also has a height of 12.7 mm, giving it a total volume of $6.4~\mu l$. The flow cell has two smaller holes with 1.5 mm diameters on the side. Rubber tubes are inserted into the holes as shown in Fig. 9.7 to flow liquid in and out. The flow cell is placed on top of the gold surface, in the SPR sensing region, and is held in place using adhesive tape. The chamber is sealed using an o-ring with a microslide clamped on top, so that liquid inside the chamber can effectively be flushed out by a new solution that is pumped in. Analyte solutions are manually pumped in through one of the rubber tubes using a syringe.

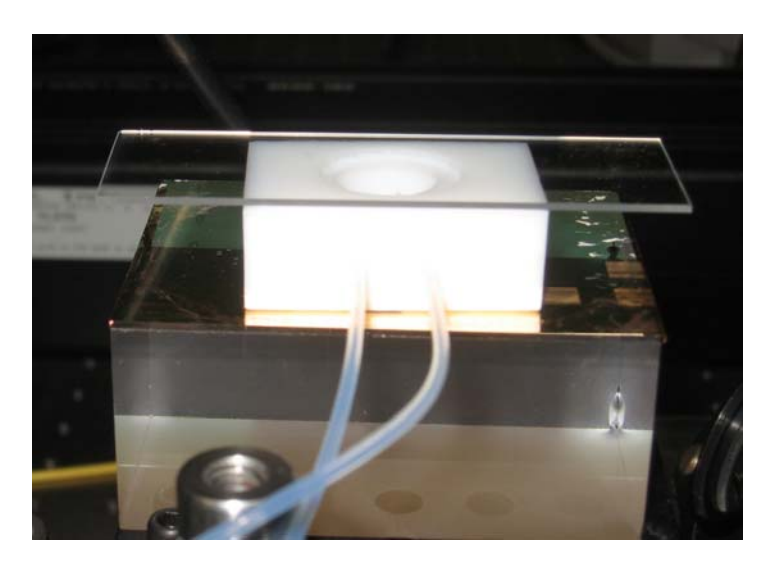


Fig. 9.7: Image of Teflon flow-cell placed on top of the sample

9.2 Results and Discussion

A typical image captured by the CCD is shown in Fig. 9.8. It resembles the Code V BPR intensity plot shown in Fig. 6.7 very closely; most of the power is concentrated towards the center and it falls off towards the edges. In terms of angular mapping, the left edge of the image corresponds to an angle of incidence 63° (with the vertical), the right edge corresponds to a 78° angle, whereas the bright region in the center corresponds to 70°.

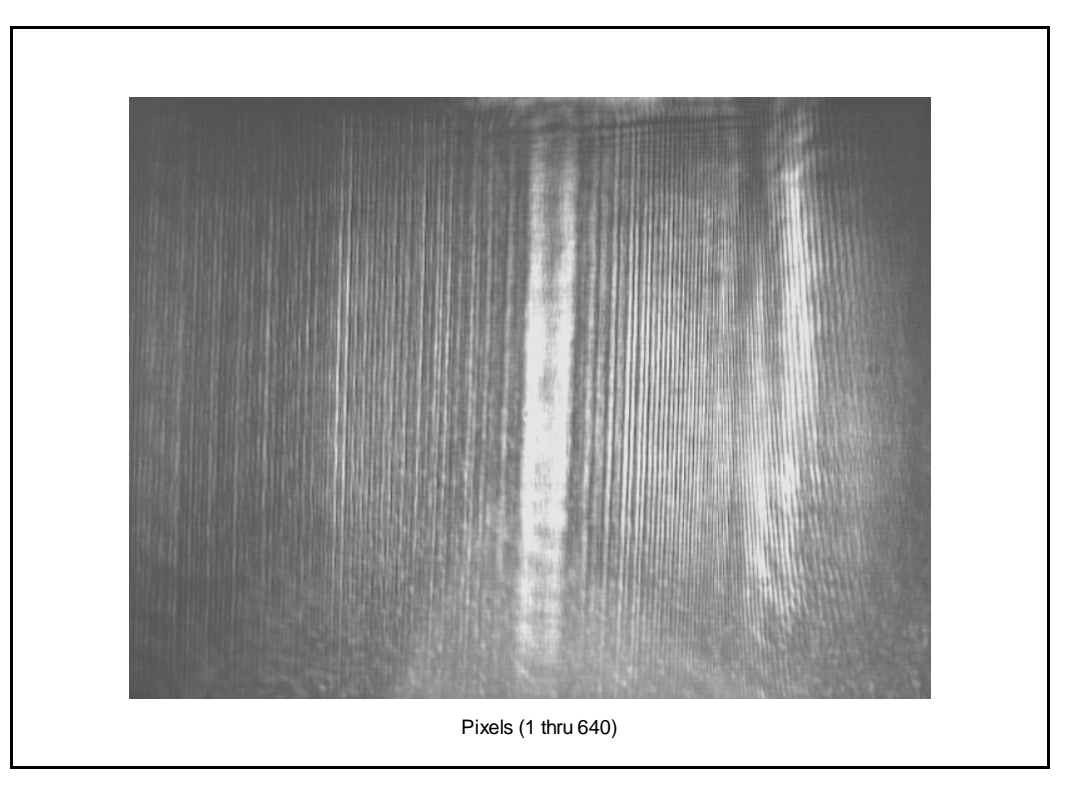


Fig. 9.8: A typical image captured on the CCD at the output of the SPR sensor

There are some key issues that need to be addressed about the image quality. Firstly, the image contains an unexpected fringing pattern. It seems to be a result of interference occurring between the first order and the zero order, which happens to be located in the middle of the desired angular range. This is a key design issue that was unfortunately overlooked in the initial design process and could have been avoided by choosing an angle of incidence outside the desired angular range, at the cost of a decrease in the minimum feature size of the DOE. The piecewise staircase profile of the DOE and the large shadowing effect discussed in Chapter 7 might also contribute to the fringing effect.

Another problem caused by the zero-order signal is that it contaminates the first-order signal. During SPR measurements, some of the adverse effects from the zero-order can be mitigated by normalization, however it does result in unwanted noise and shallow SPR dips. Also since the diffraction efficiency is non-uniform across the angular spectrum; it becomes impossible to accurately separate the power in the first order from the zero-order, even with post-processing techniques in software.

Lastly, there is another bright region which is located between the 70° and 78° region in Fig. 9.8. This unwanted light is a result of stray light reflected from the outer edges of the diffractive mirror and the edges of air cavity in the coupling slab. These stray reflections get coupled through the system and get focused, through the output focusing optics, on to the CCD and can cause large errors in SPR measurements. One method of reducing this stray light is to reduce the size of the beam incident on the DOE, so that no light is reflected off the edges. However, the CCD is extremely sensitive and can pick up even very low powers, and as such, the beam size has to be reduced considerably by modifying the Beam Expander configuration in the setup. This leads to very non-uniform illumination of the DOE thereby increasing the noise susceptibility of the system.

A second approach is to sacrifice the CCD resolution by focusing the light on to a smaller number of pixels, such that the edge of the angular spectrum lies outside the stray peak, as shown in Fig. 9.9. The 78° edge lies just outside the stray peak, whereas the 63° edge is barely distinguishable due to the overlap with the zero-order. The additional focusing is achieved by moving the 80mm output focusing lens closer to the 50mm one.

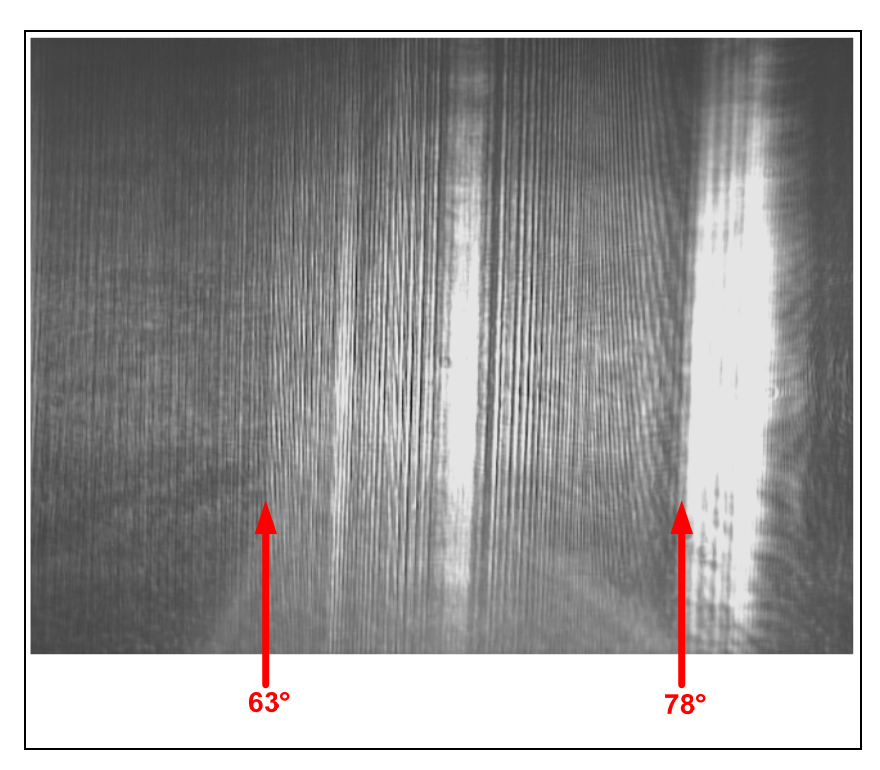


Fig. 9.9: Image taken with increased focusing. The first-order then lies outside the stray light region.

The zero-order can be partially blocked using a slit aperture at the output of the sensor before the collimating optics. Fig. 9.10 shows an image taken with a slit in place where the first-order is clearly visible.

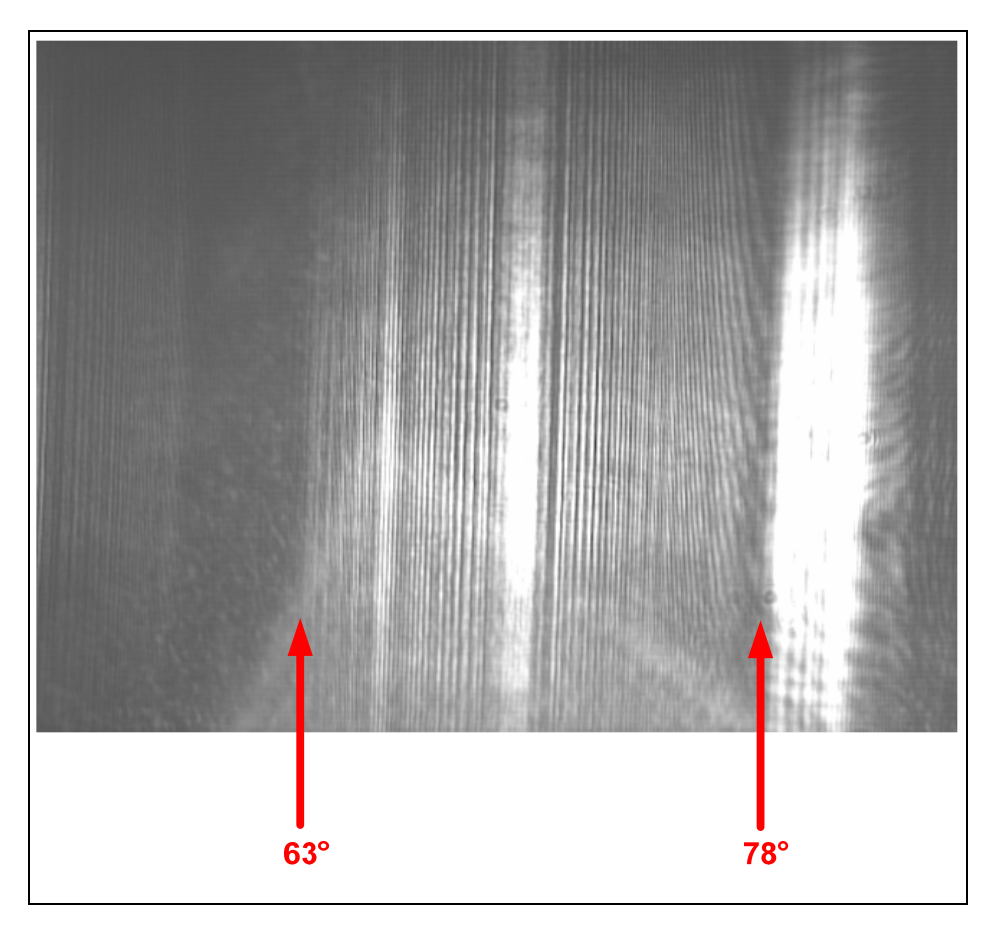


Fig. 9.10: Image taken with a slit aperture at the output which partially blocks the zero-order

9.2.1 Diffraction Efficiency Calculations

As mentioned before, it is impossible to accurately measure the diffraction efficiency due to the presence of the zero-order within the operating range. However, an estimation can be made by blocking out part of the zero-order using a slit aperture, as was done to obtain the image in Fig. 9.10. Using a power meter, the power is measured at the input facet of the sensor and at the output just before the CCD. As light propagates through the system, Fresnel losses are incurred at every interface. These loss coefficients have been

calculated using RCWA for each interface. Eq. 9.1 can then be used to estimate the diffraction efficiency of the diffractive mirror:

$$\eta_{DOE} = \frac{P_{out}}{P_{in}(1 - R_{in})R_{air}R_{SPR}R_{air}R_{SPR}(1 - R_{out})(1 - R_{lens})^2}$$
Eq. 9.1

where $P_{out} = 9.53 \mu W$ is the output power, $P_{in} = 24.80 \mu W$ is the input power, $R_{in} = 2.13\%$ is the Fresnel reflection coefficient at the input facet, $R_{air} = 100\%$ is the ideal total internal reflection coefficient due to the air cavity between the coupling slab and the sensing substrate, $R_{SPR} = 82.98\%$ is the Fresnel coefficient due to the SPR film consisting of 3nm Titanium and 50nm Gold layers, $R_{out} = 2.13\%$ is the Fresnel reflection coefficient at the output facet, and finally $R_{lens} = 1\%$ is an assumed value for the loss as the output beam travels through the two output collimating lenses. Using these values the diffraction efficiency of the DOE was calculated to be 59.45%. This value is only an upper bound, since the zero-order is not completely removed by the slit aperture. The diffraction efficiency is lower than the expected theoretical value (70.1%). The most likely origins of these additional losses are RIE depth errors and misalignment.

9.2.2 SPR Measurements

The functionality of the SPR sensor was tested using NaCl solutions with varying concentrations. It is absolutely vital that the gold sensing surface is clean because the system does respond to the presence of contaminants even in very small quantities. Before every experiment, the surface is cleaned using ethanol, which is dispensed on top of the surface using a dropper and then blow dried with an air gun.

At the beginning of an experiment, an image is captured with the laser turned off, in order to capture the background noise, which is then subtracted from all subsequent images taken with the laser switched on. Temporal averaging is performed on every image that is captured, using a simple program implemented in LABVIEW [9.2]. 50 images are averaged together, which has the effect of cutting down temporal variations due to laser

and CCD fluctuations by a factor of $\sqrt{50}$. However, it takes roughly 60 seconds to capture and average 50 images. Thus, this setup is not very suitable for obtaining kinetic data.

The laser is then switched on and the input power is slowly increased to 350 mW. The reasons for using such a high input power have been discussed earlier in Section 9.1.1. The power, however, has to be attenuated using neutral density filters, to around $25 \mu W$ at the sensor input, in order to avoid saturating the CCD.

With the polarization at the sensor input set to TM, a first measurement is made without any solution in the flow cell. Since there is no SPR coupling for a naked gold surface, this image is used to normalize all subsequent SPR measurements. Normalization of SPR spectra is quite typical, and any non-resonant data can be used for this purpose. Since SPR only occurs with TM polarization, it is common to take an image with TE polarization, and then divide the corresponding TM data with the TE data. This technique could not be used in our case because changing the polarization causes a shift in the interference fringes present in the output, thereby rendering any normalization with TE data impossible.

Next an aqueous solution is pumped into the flow-cell using a syringe. Fig. 9.11 shows the raw data before and after the addition of water to the flow-cell. Only one half of the 640 pixels are used in order to cut out the unwanted stray peaks and zero-order signal. Fig. 9.11 shows that part of the bright peak in the middle is absorbed due to the addition of de-ionized water on top of the gold surface.

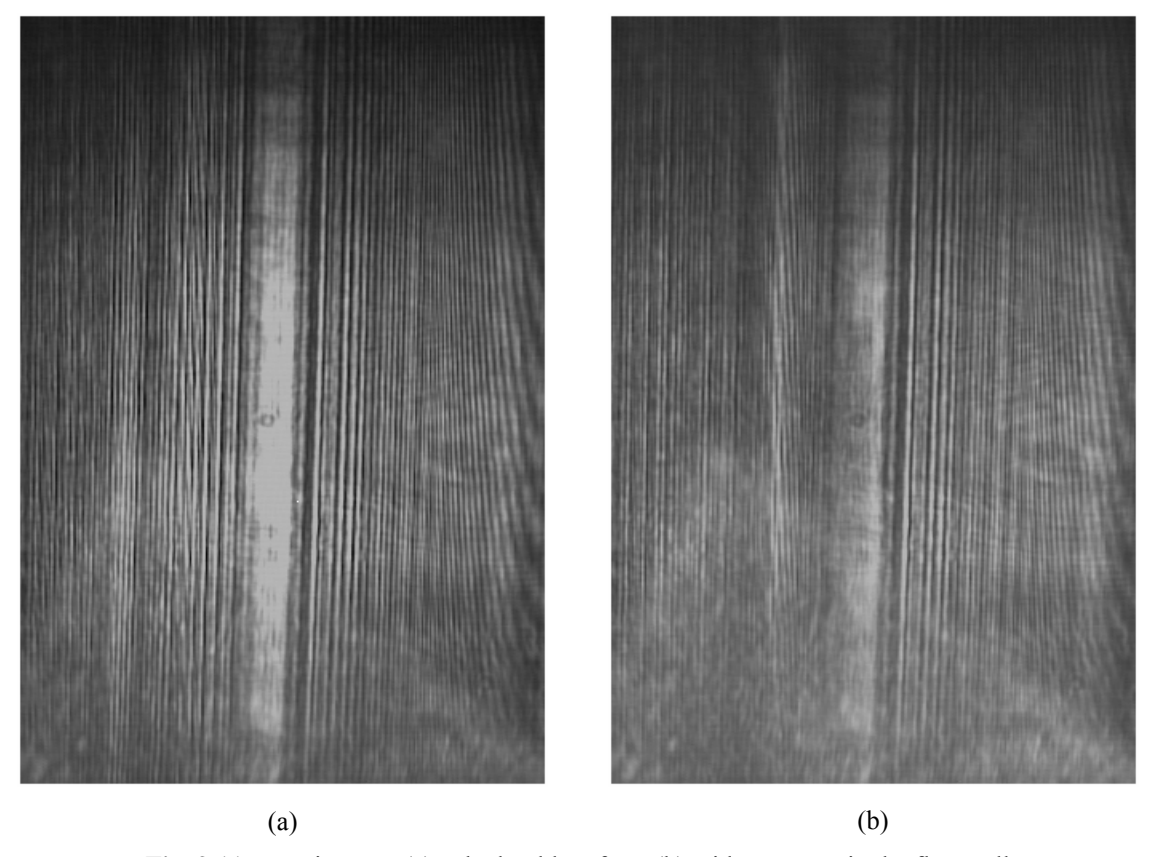


Fig. 9.11: Raw images: (a) naked gold surface, (b) with DI water in the flow-cell

Fig. 9.12(a) shows the results after the data has been normalized with the TM data obtained with a naked gold surface. The normalized data is then averaged using a spatial averaging filter in MATLAB to smooth out the data.

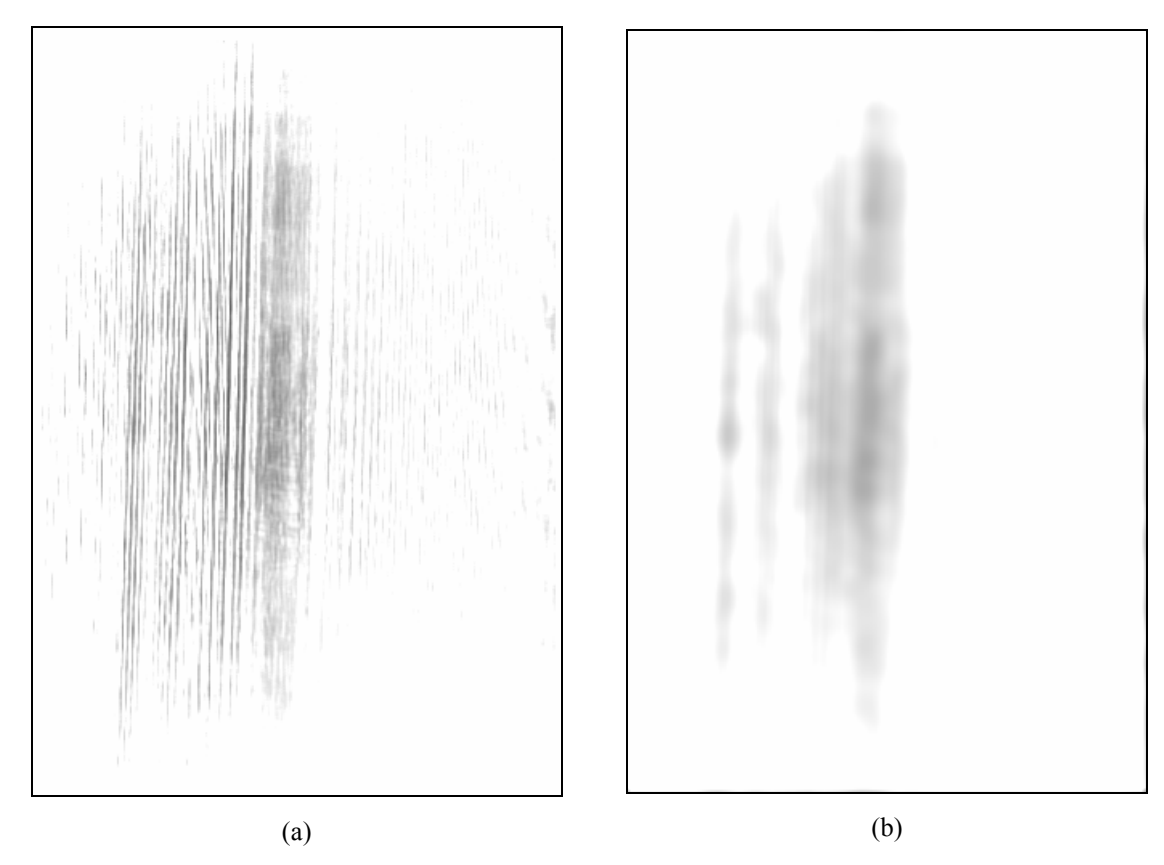


Fig. 9.12: (a) Normalized data, (b) Averaged normalized data

A horizontal cross-section through the 2-D normalized and averaged image reveals the familiar SPR dip. The mapping between pixels and angular domain is achieved by a two-step process; first the non-resonant raw data from Fig. 9.11(a) is considered and the pixel located in the middle of the central bright region is noted. This pixel is assigned a value of 70°, which happens to be the angle of incidence and also the mean of our angular range. Secondly, since the total number of pixels corresponds to a length of 12.054mm, the angular values corresponding to each pixel are calculated using the geometry of the device and simple trigonometry. Fig. 9.13 shows the SPR dip for DI water.

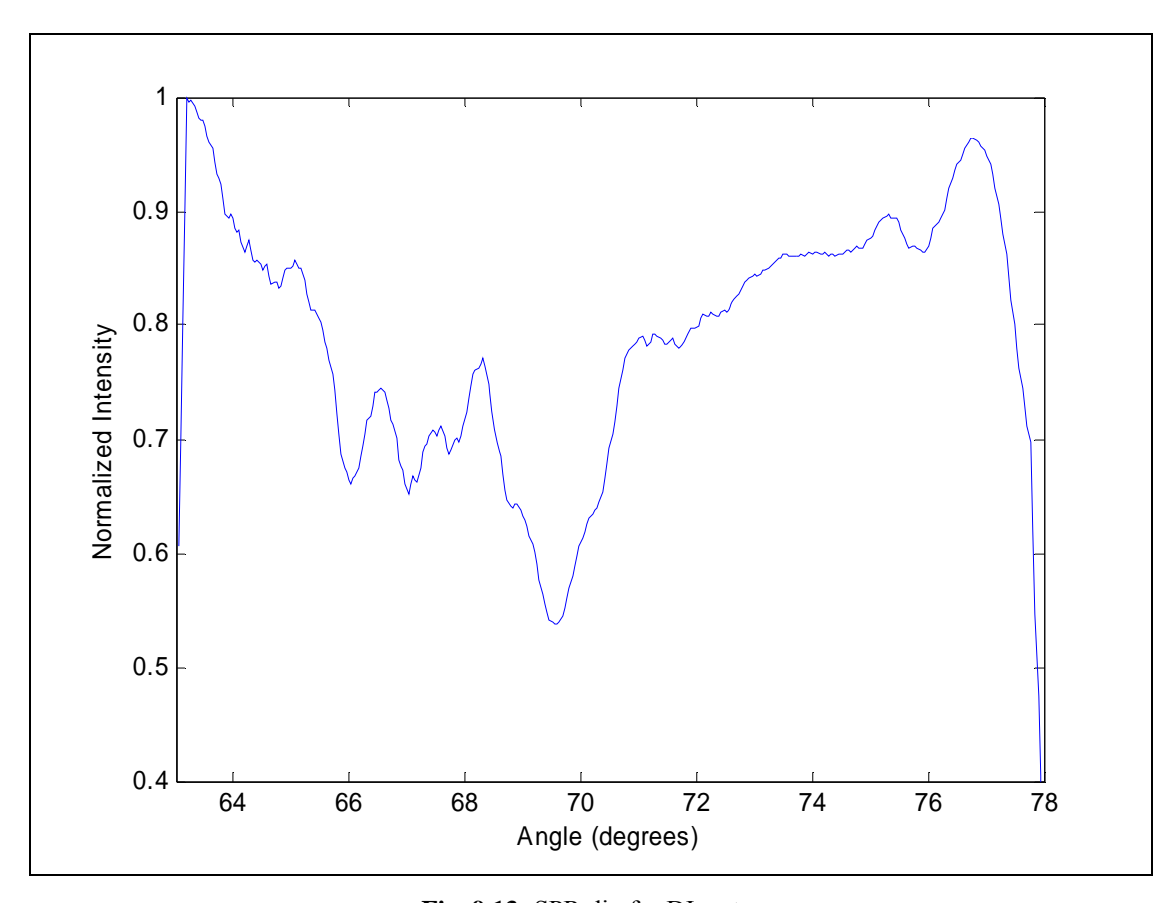


Fig. 9.13: SPR dip for DI water

The SPR coupling angle is not necessarily located at the minimum of the normalized intensity curve due to system noises. Dip tracking has been the focus of a lot of research as of late and various techniques such as the centroid method [9.3], polynomial curve fitting, dynamic baseline adjustments [9.4] and optimal linear data analysis have been proposed [9.5]. The simple centroid algorithm [9.3] is employed in our case to determine the geometric center of the resonance minimum. The algorithm is applied to pixels, and hence angles, with intensity values lower than a certain threshold value I_{th}, using the following equation:

$$\theta_{cen} = \frac{\sum_{m} \theta_m (I_{th} - I_m)}{\sum_{m} (I_{th} - I_m)}$$
 Eq. 9.2

where θ_m and I_m corresponding to the angle and intensity of the *m*th horizontal pixel, respectively. Using Eq. 9.2, the SPR dip for water in Fig. 9.13 is located at an angle of 69.56°. This result was compared with RCWA simulation results for a model with 3nm of Titanium and 50nm Gold on a fused silica substrate, shown in Fig. 9.14. The theoretical dip is located at 69.61°, which is in close agreement with the experimental value. The small (0.07%) discrepancy between the theoretical and experimental results can be attributed to impurities in the DI water, any residue or contaminants present on the gold surface, various noise sources in the experimental setup, angular misalignments, and limited CCD resolution.

Even though the dip locations are extremely close in the theoretical and experimental results, there is a significant difference in the depth of the dips, owing to two major factors: firstly, the zero-order light and noise from the laser within the measured spectrum does not couple into the SP mode. Secondly, the dip depth is very sensitive to the thickness of the gold surface. A 5nm change in the 50nm gold thickness can cause the dip to be as much as 15% higher. Thus any inconsistencies in the gold and titanium deposition can cause large discrepancies. However, most SPR measurements are based on relative changes in the dip location rather than absolute position and depth of the dip. Therefore, our results should not be affected too badly by these adversities.

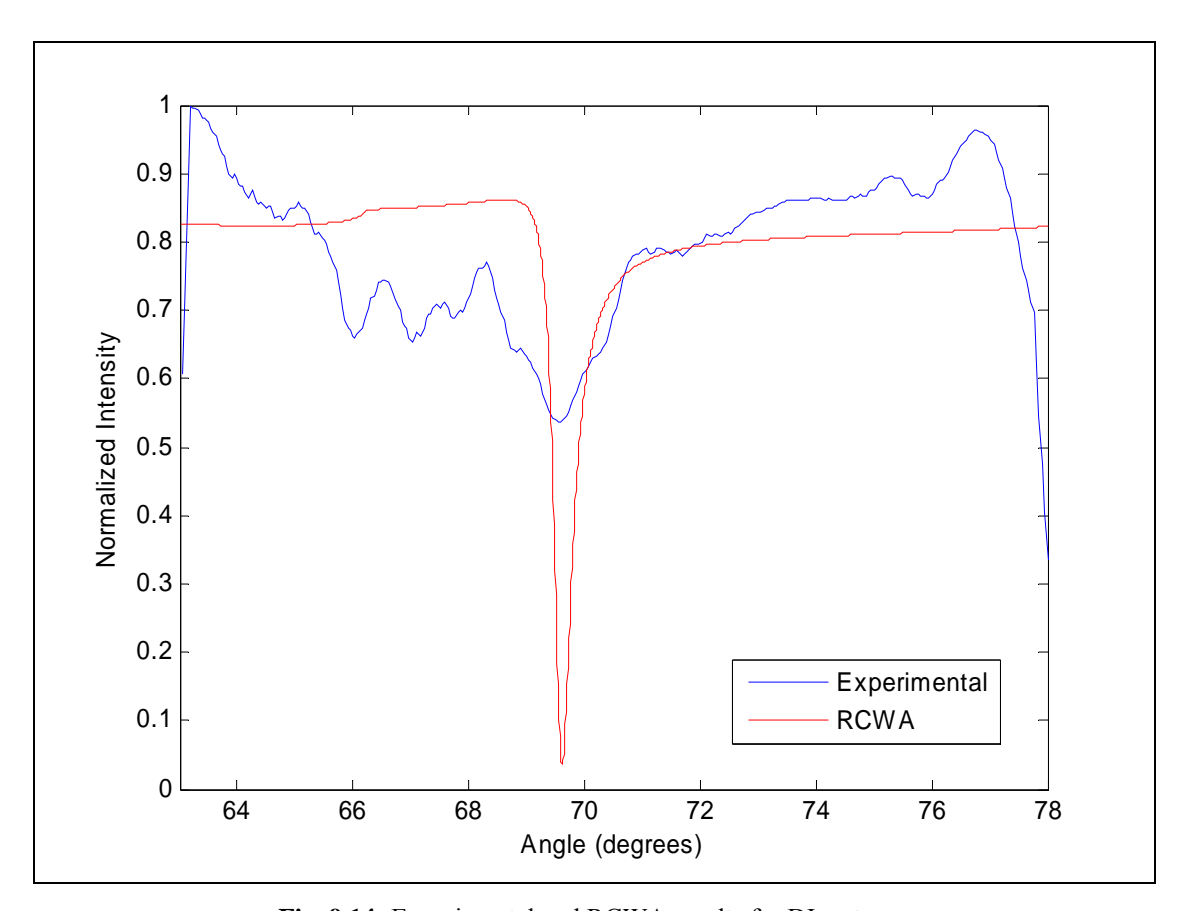


Fig. 9.14: Experimental and RCWA results for DI water

Next the dynamic range of the system was tested using NaCl solutions with concentrations of 0M (DI Water), 1M, 1.5M, 2M, 2.5M and 3M. The solutions were pumped into the flow-cell in increasing order of concentration. The normalized and averaged 2D images obtained for these solutions are shown in Fig. 9.15. The dip position shifts from left to right, that is, to larger coupling angles as the concentration of NaCl increases.

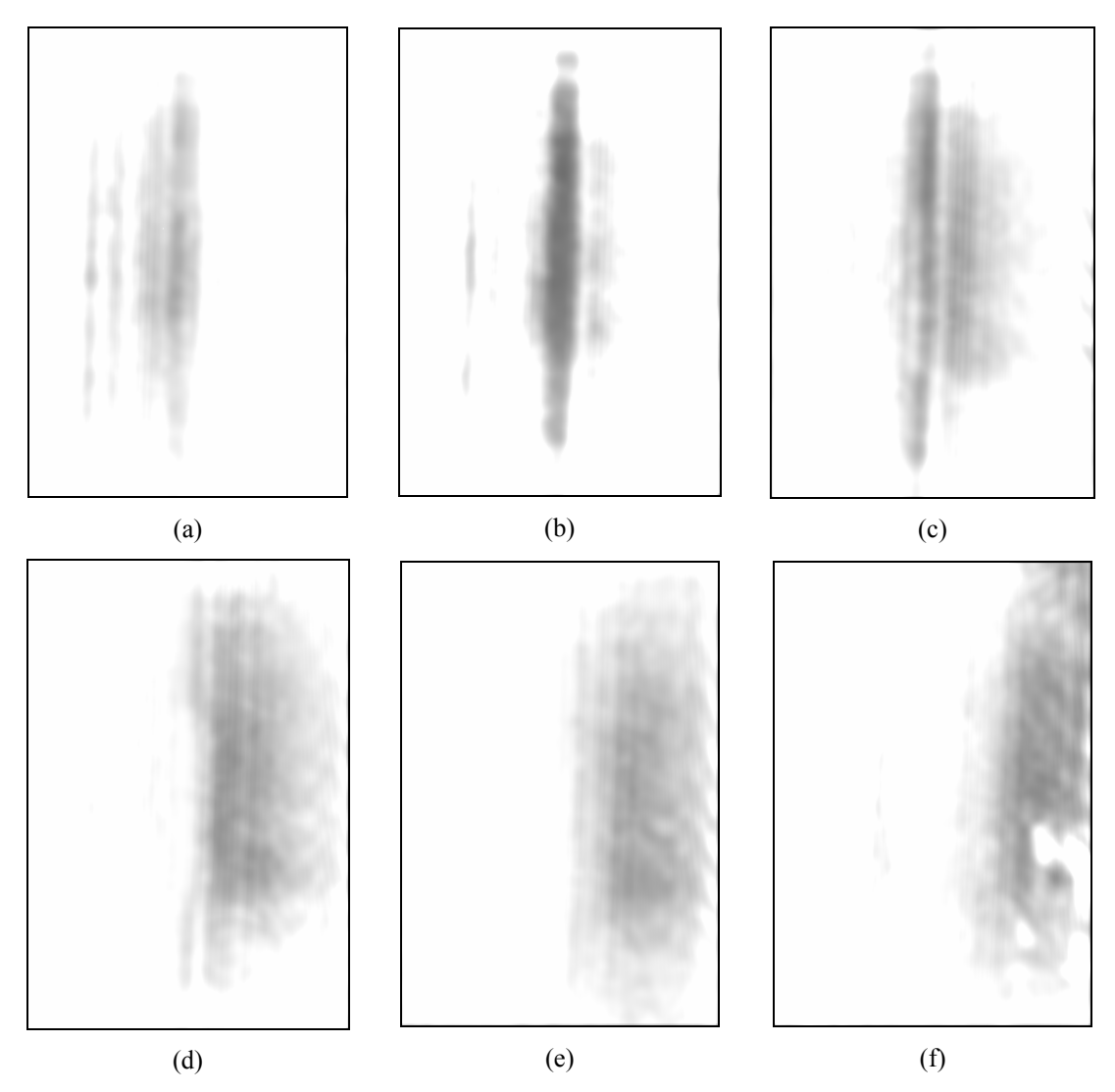


Fig. 9.15: Normalized and averaged 2D images obtained with NaCl solutions with concentration of (a) 0.0M (DI water), (b) 1M, (c) 1.5M, (d) 2M, (e) 2.5M and (f) 3M. The SPR coupling angle shifts to larger angles for higher concentrations of NaCl.

Horizontal cross-sections through each of these images are plotted in Fig. 9.16. It must be pointed out that the cross-section for each image is normalized independently; hence, Fig. 9.16 does not give an accurate comparison of the relative intensities for each analyte solution.

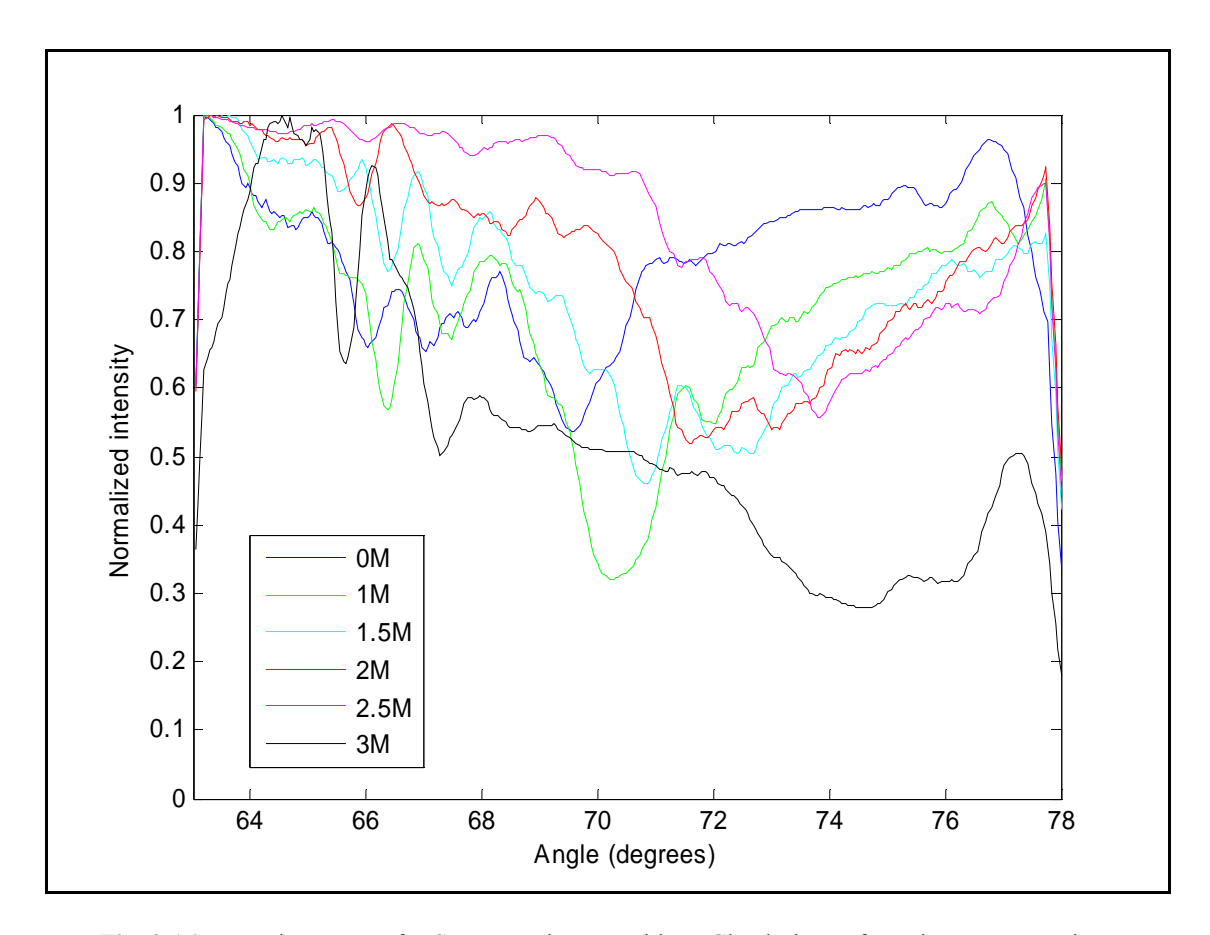


Fig. 9.16: Intensity spectra for SPR experiments with NaCl solutions of varying concentrations

The centroid algorithm is again applied to each intensity spectrum to locate the dip positions. It can be seen from Fig. 9.16 that SPR dips can be quite wide, spreading over several degrees in angle, however, this is not uncommon for experimental data reported in the literature. The refractive index of the NaCl solutions can be determined from these measurements by equating Eq. 2.1 and Eq. 2.2 and re-arranging:

$$n_D = \sqrt{\frac{\varepsilon_M (n_{FS} \sin \theta_{res})^2}{\varepsilon_M - (n_{FS} \sin \theta_{res})^2}}$$
 Eq. 9.3

where n_{FS} is the refractive index of fused silica, ϵ_M is the dielectric constant of gold at 850nm and θ_{res} is the SPR coupling angle. The coupling angles and corresponding refractive indices for the salt solutions are tabulated below:

Table 9.1: SPR coupling angles for NaCl solutions of various concentrations

NaCl Concentration (M)	0	1	1.5	2	2.5	3
Coupling angle	69.564°	70.876°	71.308°	72.809°	73.904°	74.628°
Refractive index	1.3288	1.3387	1.3424	1.3535	1.3609	1.3655

It must be noted that the data in Table 9.1 corresponds to Fig. 9.15 only. These experiments were carried out numerous times, both in increasing and decreasing order of concentration, and the variations in the measured refractive indices were as large as 0.7%. The variations were particularly large during experiments with solutions in decreasing order of concentration. A number of factors contribute to these discrepancies. For instance, the fringes caused by the zero-order can reduce the accuracy of the centroid method to determine the resonance angle. More importantly, however, the SPR phenomenon is very sensitive and any contamination in the salt solutions or the gold surface at the beginning of experiments can result in noticeable errors. The chances of contamination are particularly high when starting off with high concentration solutions since with the current setup, which is equipped with a simple syringe, solutions can not be perfectly flushed out in between experiments. The use of a peristaltic pump could result in a significant improvement in the results. Fig. 9.17 shows the variation of refractive index with concentration, which is fairly linear. The results from experiments with solutions in decreasing order of concentration were not included in the analysis.

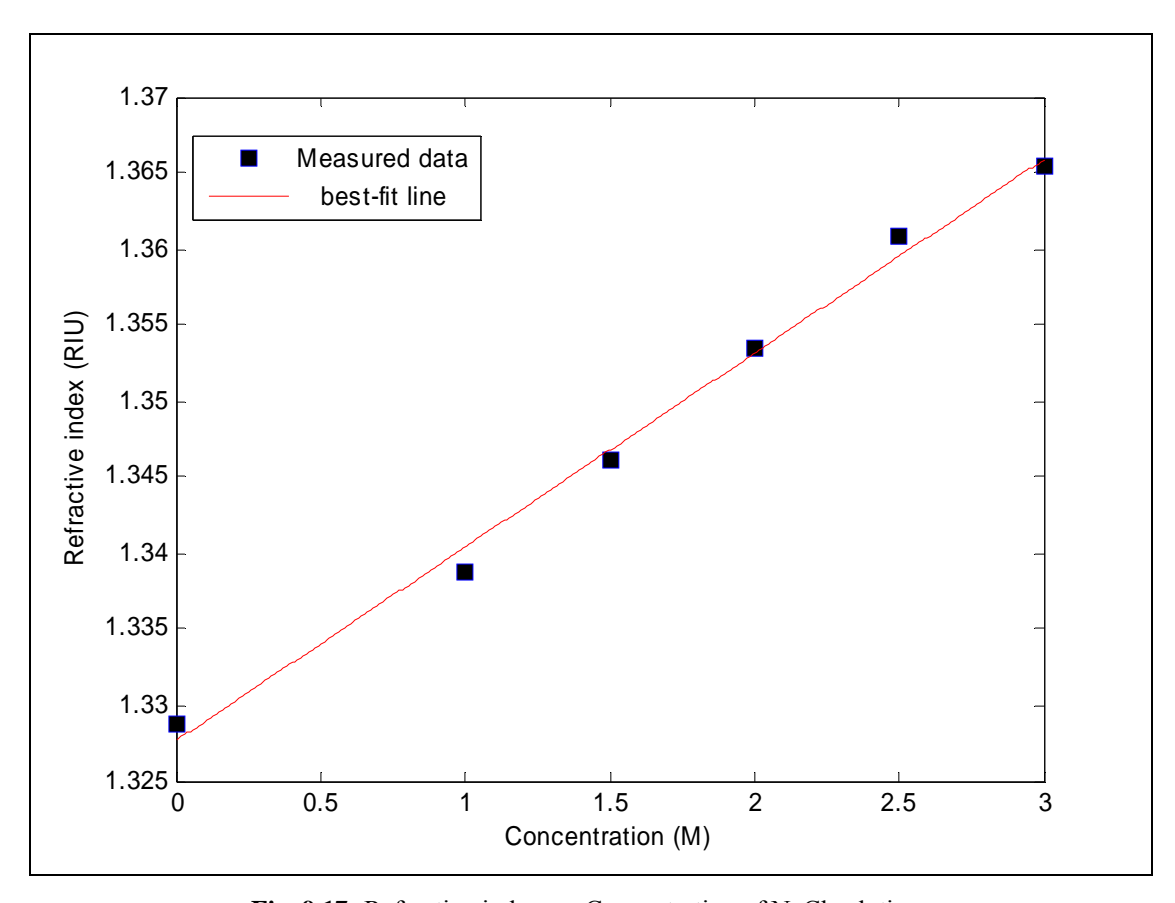


Fig. 9.17: Refractive index vs. Concentration of NaCl solutions

In order to determine the sensitivity of refractive index to concentration changes, $\partial n/\partial C$, more accurately, the experiments were repeated with NaCl solutions of smaller concentrations, varying from 0M to 1M, in order of increasing concentration. The results are shown in Fig. 9.18. The error bars are roughly the size of the data markers. The $\partial n/\partial C$ is given by the slope of the best-fit line.

$$\frac{\partial n}{\partial C} = 0.0096911 \text{ RIU/mol} = \frac{0.0096911*1000ml}{58.4425g} = 0.1658 \text{ ml/g}$$
 Eq. 9.4

where, 58.4425g is the molar mass of NaCl. Most of the data on $\partial n/\partial C$ of NaCl solutions has been reported for 587nm (0.17138 ml/g) and 633nm (0.17010 ml/g) wavelengths [9.6,9.7]. The reported $\partial n/\partial C$ decreases for increasing wavelengths. For 850nm, only extrapolated data was obtained from [9.8], which is within 1% agreement of our results.

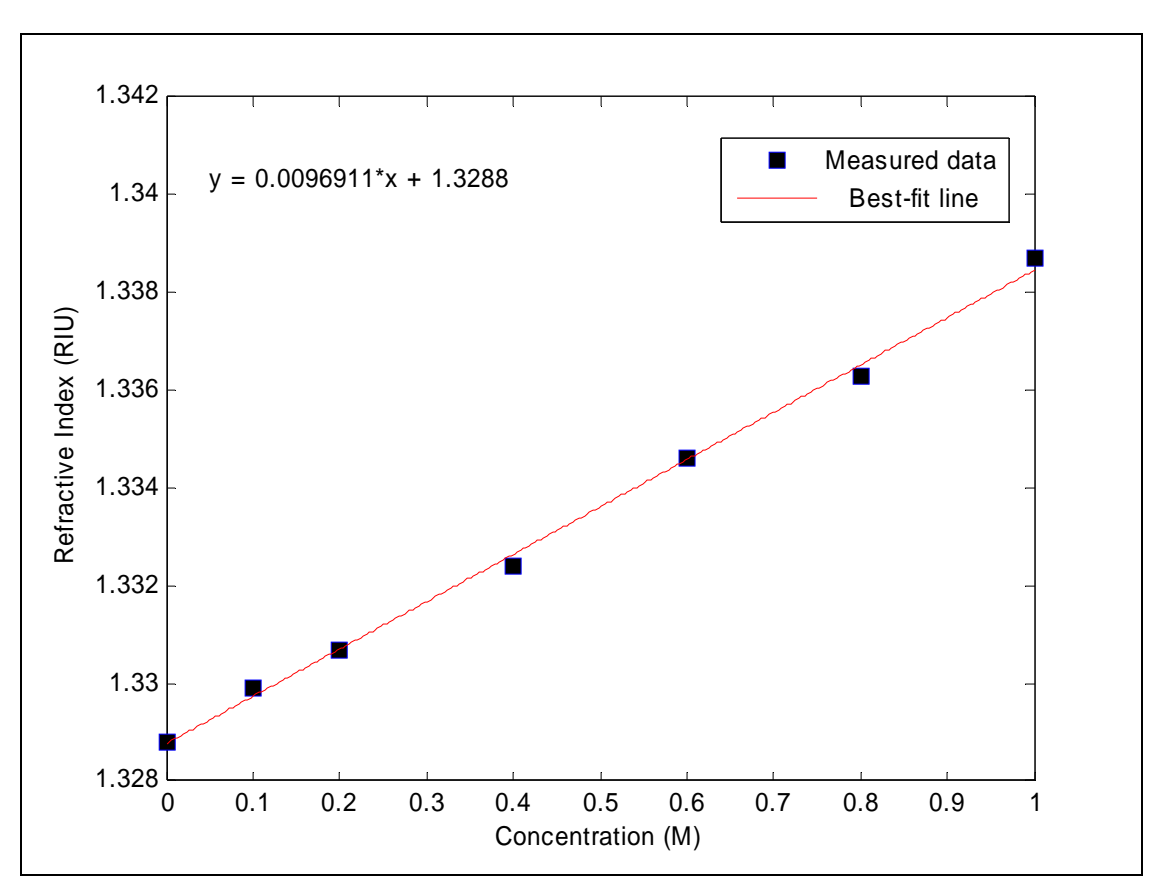


Fig. 9.18: Refractive index vs. Concentration for 0M – 1M NaCl solutions

Fig. 9.19 shows a plot of the SPR angle vs. refractive index. The angular sensitivity given by the slope is 125°/RIU. This result is consistent with the theoretical sensitivity of 124.54°/RIU calculated using Eq. 2.5 which is repeated here for convenience:

$$S = \frac{\partial \theta_{res}}{dn_{new}} = S = \frac{\varepsilon_M^2}{\mid \varepsilon_M + n_{new}^2 \mid \sqrt{\varepsilon_M n_{fs}^2 (\varepsilon_M + n_{new}^2) - \varepsilon_M^2 n_{new}^2}} \quad \text{(rad/RIU)},$$
 Eq. 9.5

The theoretical angular sensitivity reported in [9.9] for an 850nm wavelength prism-coupler based system is 97°/RUI, which is much lower than our results. However, this discrepancy should not be too alarming, since from Eq. 9.5, it is evident that the sensitivity depends significantly on the dielectric constant of gold, and there is a great deal of variation in the reported data on gold optical properties in the literature. Thus the

lower sensitivity reported in Ref. [9.9] can be easily due to a different source used to obtain gold data.

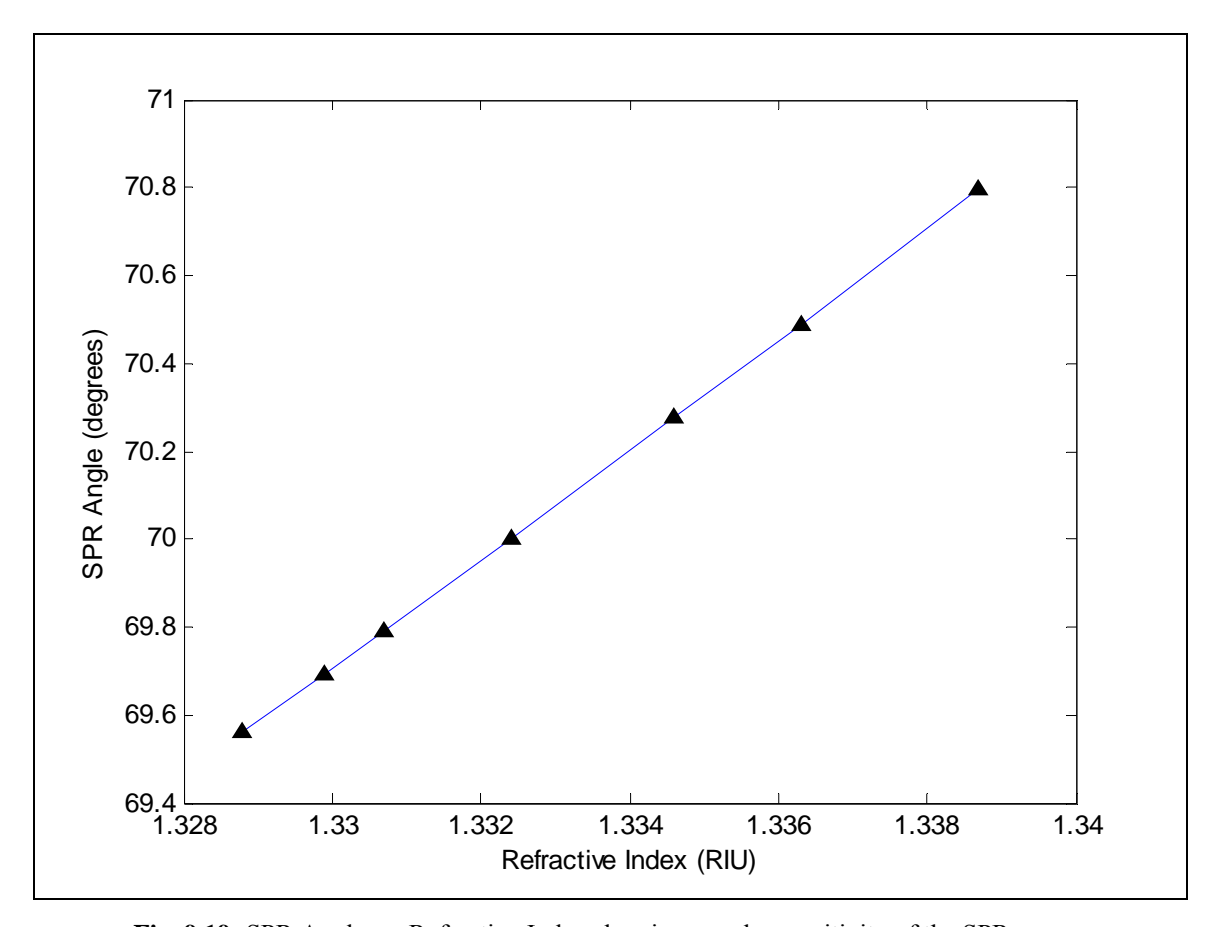


Fig. 9.19: SPR Angle vs. Refractive Index showing angular sensitivity of the SPR sensor

9.2.3 Noise measurements and detection limit

Accurate determination of the system noise is absolutely vital to the performance evaluation of the SPR sensor. Noise was measured using a sample whose gold surface has been cleaned with ethanol and then repeatedly flushed with DI water. The SPR dip with DI water was captured in the same manner as before with each image being averaged 50 times before being recorded. 20 such images were recorded at 1 minute intervals.

The SPR dip locations (in degrees) were calculated using the centroid method for 40 successive pixel rows (rows 220 – 260) in each of the 20 recorded 2-D images, and converted to refractive index units using Eq. 9.3. The standard deviation of the dip centroid was calculated for each pixel row. The average of the standard deviations determined the final RMS noise level which was calculated to be 2.6×10^{-5} RIU. This noise level is poor compared to the noise level of 1.0×10^{-6} RIU reported in [9.9] for prism-coupler based SPR sensors at 850nm wavelength. The order of magnitude difference in performance can be attributed to the poor emission spectrum of the SDL laser, the poor quality of the low-end CCD camera being used and the presence of the zero-order signal within the desired spectrum.

The minimum detection limit is another important parameter that determines the smallest change that can be detected by the sensor. It is given by the ratio of the measurement accuracy of the SPR angle and the angular sensitivity. The detection limit is roughly estimated to be three standard deviations from the noise floor, i.e. $\sim 7.8 \times 10^{-5}$ RIU. In order to verify this, an SPR experiment was carried out using 0.01M NaCl solution. Using the $\partial n/\partial C$ from Fig. 9.17, the 0.01M solution should cause a change in refractive index of 9.69×10^{-5} RIU which should be within the detection limit. The experimentally detected change was $1.07 \times 10^{-4} \pm 5\%$ RIU leading to a discrepancy of 10.4%. At such low concentrations, if the contaminations from the Teflon chamber, gold surface, syringe and those during solution preparation are taken into account, the results seem fairly reasonable.

9.3 Summary of sensor performance

The performance of the SPR sensor is quite promising. The sensor can track the concentration changes in analyte solutions fairly accurately and experimental data showed excellent correlation with theoretical and published data. The diffraction efficiency of the diffractive mirror is close to 60%, which is lower than expected, primarily due to minor fabrication errors. The angular sensitivity is calculated to be

125°/RIU which is also in strong agreement with theoretical results. The noise performance of the sensor was not as promising primarily due to certain hardware and design limitations. As a result, the detection limit of the sensor also suffered. But overall, the design concept of the device was thoroughly verified and the results can be improved upon in numerous ways, some of which are discussed in the next section. The performance parameters of the SPR sensor detailed earlier have been summarized in Table 9.2.

Table 9.2: Performance parameters of the integrated SPR sensor

Diffraction efficiency of DOE (%)	< 59.45	
Angular Sensitivity (°/RIU)	125	
Average Noise (RIU)	2.6×10^{-5}	
Minimum detection limit (RIU)	$\sim 7.8 \times 10^{-5}$	

9.4 Future considerations

Despite the promising results of the integrated SPR sensor, there are certainly numerous avenues that can be explored to improve the accuracy, repeatability, and detection limit, such that the performance is comparable to commercial SPR systems. Some suggestions are listed below:

- Perform experiments using a peristaltic pump to improve repeatability and accuracy of results.
- Perform experiments to determine bio-chemical binding events. Current system is severely limited by the CCD and simple flow system such that it is impossible to obtain kinetic data. More expensive CCD cameras can sample faster and perform averaging on the go, and have lower shot and thermal noises. A peristaltic pump together with a better and faster CCD could reduce noise, improve the detection limit and allow investigation of bio-chemical interactions.

- Characterize noise sources in the system more thoroughly and target each source independently to improve noise performance of the system.
- Develop an integrated microfluidic system on top of the planar sensor surface to make multi-analyte sensing possible.
- Perform spatial filtering to improve the profile of the input laser beam. This would remove some non-uniformities in the intensity spectrum captured by the CCD.
- Develop more robust post-processing techniques to locate the SPR dip position and filter out any noise if possible.
- A big improvement could be made if the design of the device was modified slightly to move the input incidence angle out of the operating range of the sensor, at the expense of a smaller minimum feature size for the DOE. The operating range would also have to be reduced say to 10°, in order to stay above the 1μm minimum feature size limit. For example, we would have to reduce the operating range say between 65° 75° with an angle of incidence of 63°. This would remove the problems caused by the zero-order, thereby improving the noise, accuracy and repeatability of the system.
- Scale down the device. The current dimensions of the system are very conservative and were chosen to facilitate fabrication and testing. However, since the operating concept has been tested and verified, the device can be scaled down by a factor of 5 10 times, leading to a substantially miniaturized device.
- The large single coupling slab should be split into two coupling slabs, one for input and output coupling each. This would make the index-matching process much more practical, while saving time and money spent on fabrication.
- A suitable process-flow should be developed to fabricate the device in a polymer substrate using injection molding and stamping techniques. This would result in highquality devices that are reproducible and cost-effective.

9.5 References

- [9.1] "Oz Optics website: www.ozoptics.com," 2007.
- [9.2] "National Instruments website: www.ni.com/labview/," 2007.

- [9.3] G. G. Nenninger, M. Piliarik, and J. Homola, "Data analysis for optical sensors based on spectroscopy of surface plasmons," *Measurement Science & Technology*, vol. 13, no. 12, pp. 2038-2046, Dec.2002.
- [9.4] C. Thirstrup and W. Zong, "Data analysis for surface plasmon resonance sensors using dynamic baseline algorithm," *Sensors and Actuators, B: Chemical*, vol. 106, no. 2, pp. 796-802, 2005.
- [9.5] T. M. Chinowsky, L. S. Jung, and S. S. Yee, "Optimal linear data analysis for surface plasmon resonance biosensors," *Sensors and Actuators B: Chemical*, vol. 54, no. 1-2, pp. 89-97, Jan.1999.
- [9.6] Y. Sarov, S. Sainov, I. Kostic, V. Sarova, and S. Mitkov, "Automatic VIS- near IR laser refractometer," *Review of Scientific Instruments*, vol. 75, no. 10, pp. 3342-3344, Oct.2004.
- [9.7] J. R. Castrejon-Pita, A. Morales, and R. Castrejon-Garcia, "Critical angle laser refractometer," *Review of Scientific Instruments*, vol. 77, no. 3 Mar.2006.
- [9.8] A. Kruis, "The equivalent dispersion of strong electrolytes in solution. I. The measurement of the concentration dependence of visual equivalent refraction," *Zeitschrift fur Physikalische Chemie-Abteilung B-Chemie der Elementarprozesse Aufbau der Materie*, vol. 34, no. 1/2, pp. 13-50, Oct.1936.
- [9.9] J. Homola, S. S. Yee, and G. Gauglitz, "Surface plasmon resonance sensors: review," *Sensors and Actuators B: Chemical*, vol. 54, no. 1-2, pp. 3-15, Jan.1999.

Conclusion

Design, fabrication and performance results of a highly integrated surface plasmon resonance sensor were presented. The sensor employs a diffractive optic element to provide simultaneous reflectivity data for a 15° angular range, thereby avoiding the need to manually scan through each angle. The device requires no moving parts which makes it more durable and robust, while making the measurements less prone to error. The planar design of the sensor makes it favorable for integration with an advanced microfluidic system which can allow for easy delivery and simultaneous sensing of multiple analytes.

The DOE is an off-axis 8-level focusing mirror fabricated in a fused silica substrate, designed for operation in the first diffraction order. It has a relatively large minimum feature size of 1.5µm, which presents a significant advantage, in terms of ease and accuracy of fabrication, over previous designs. Also the multi-level profile leads to higher achievable diffraction efficiency. The large angular range obtained using this DOE translates to a large dynamic range in terms of refractive index of solutions that can be tested using this sensor.

Fabrication was performed using multi-step photolithography and reactive ion etching. The smallest misalignment achieved after 3 alignment steps was 0.3µm. The theoretical diffraction efficiency of the mirror was determined to be 70.1%; however, due to misalignment and RIE errors, the experimental diffraction efficiency was measured to be less than 60%.

The sensor was thoroughly tested using NaCl solutions of concentrations varying from 0 – 3M. Higher concentration solutions were used to test the dynamic range of the sensor, where as lower concentration solutions were used to calibrate the system. The experimental results were fairly repeatable and showed excellent correlation with theoretical and published data. The angular sensitivity of the sensor was measured to be

125°/RIU. The RMS noise in the system was determined to be 2.6x10⁻⁵ RIU, where as the minimum detection limit was around 7.8x10⁻⁵ RIU. The noise and detection limit results are not as promising primarily due to poor laser and CCD characteristics, and due to the zero-order signal which lies within the operating range. Table C1 shows a comparison of the performance of our sensor with theoretical data and the commercially available Spreeta sensor. There is an order of magnitude difference in the noise and detection limit performance of the present design and the theoretical and commercial data. The results can be significantly improved by using a CCD that can sample data faster and by averaging a larger number of images.

Table C1: Comparison of results with theoretical and commercial data

	Angular Sensitivity (°/RIU)	Average Noise (RIU)	Minimum detection limit (RIU)
Present design	125	2.6×10^{-5}	$\sim 7.8 \times 10^{-5}$
Reported theoretical data for 850nm prism coupler based sensor [9.9]	97	1x10 ⁻⁶	1.03x10 ⁻⁶
Spreeta sensor (Source emission peak ~880nm) ^a	90.9	1.5x10 ⁻⁶	4.5x10 ⁻⁶

^a Application notes on Spreeta SPR sensor, www.sensata.com, 2007

No biochemical binding events could be studied unfortunately, due to hardware limitations. Use of a peristaltic pump together with a low noise CCD camera would enable us to obtain kinetic data for biochemical sensing, and would greatly improve the accuracy and repeatability of the device.

Overall the results obtained are very promising. The sensor has great potential for miniaturization and a suitable process should be developed to fabricate the sensor in a polymer substrate using injection molding and imprinting techniques.